# On the Conversion of Nanocomposite Architectures

Hans C. Hendrikse

# On the Conversion of Nanocomposite Architectures

Hans C. Hendrikse

Ph.D. Thesis, University of Amsterdam, February 2021

*On the Conversion of Nanocomposite Architectures*

Hans Christiaan Hendrikse

Cover image:
Scanning electron image of a field of $SnO_2/SiO_2$ nanocomposite architectures. Imaged with help of the Amsterdam Nanocenter, AMOLF, Amsterdam, The Netherlands.

ISBN: 978-94-92323-49-1

The work described in this thesis was performed at
AMOLF, Science Park 104, 1098 XG, Amsterdam, The Netherlands.

This work is part of the Dutch Research Council (NWO). It is also funded by the Vernieuwingsimpuls Vidi research program "Shaping up materials" with project number 016.Vidi.189.083.

This thesis was produced on FSC® certified materials.
A digital version of this thesis can be downloaded from
http://amolf.nl and https://dare.uva.nl/

# On the Conversion of Nanocomposite Architectures

## ACADEMISCH PROEFSCHRIFT

ter verkrijging van de graad van doctor

aan de Universiteit van Amsterdam

op gezag van de Rector Magnificus

prof. dr. ir. K.I.J. Maex

ten overstaan van een door het College voor Promoties ingestelde commissie,

in het openbaar te verdedigen in de Aula der Universiteit

op vrijdag 26 februari 2021, te 14:00 uur

door

Hans Christiaan Hendrikse

geboren te Scherpenzeel

Promotiecommissie:

| | | |
|---|---|---|
| Promotor: | prof. dr. H.J. Bakker | *Universiteit van Amsterdam* |
| Copromotor: | dr. W.L. Noorduin | *AMOLF, Amsterdam* |
| Overige leden: | prof. dr. H. Cölfen | *University of Konstanz* |
| | dr. M.F. Neira d'Angelo | *Eindhoven University of Technology* |
| | prof. dr. M.L. van Hecke | *Universiteit Leiden* |
| | prof. dr. D. Bonn | *Universiteit van Amsterdam* |
| | prof. dr. B. de Bruin | *Universiteit van Amsterdam* |
| | dr. J.C. Slootweg | *Universiteit van Amsterdam* |

Faculteit der Natuurwetenschappen, Wiskunde en Informatica.

*"Be confident enough to try, but humble enough to learn."*

# Contents

# Chapter 1

## Introduction

## 1.1 Progress in Man-Made Materials

*"...remember that a CPU is literally a rock that we tricked into thinking"*
Ben Driscoll

In this world there are many compounds with fascinating properties. Just as silicon can be 'tricked' to become a powerful computer, so too can we trick cobalt to become a versatile catalyst or lead to be a tunable semi-conductor.[1–3] In fact, one could consider that tricking elements into doing what we want has played a pivotal role in the development of our society.[4] From the very early days of using stone, bronze and iron to create tools, to the industrial revolution using coal to power our factories, utilizing the power a compound possesses is crucial to our technological progress.[5,6]

The utilisation of such a compound is linked to how well we can give it a proper shape: An axe is dysfunctional without a sharp edge, just like a battery will not power anything if it short circuits. It is the combination of composition and organisation that makes a compound a functional material. In our thousands of years of material-making, we have developed many ways to shape materials either in large numbers or in specific morphologies.[7,8] However, our ability to do so depends on the scale of the particular material. Shaping a material not only becomes more difficult when it becomes too large to handle, but also when it becomes too small to manipulate easily.[9] In fact, a big challenge in our current age is to gain control over a material on the nano- to micrometer scale.

Though the nano- to microscale is invisible to the human eye, the effects of the organization at this scale are very visible. For example, solar cells rely on their organisation at this scale to obtain high conversion efficiencies, while catalysts work best as tiny nanoparticles embedded on a supporting material (Figure 1.1).[10,11] Thus, organization on this invisible scale gives access to sources of renewable energy and ways to create various compounds. Yet, organizing at this scale is not trivial, and often requires elaborate setups to properly shape the correct compounds.[12,13]

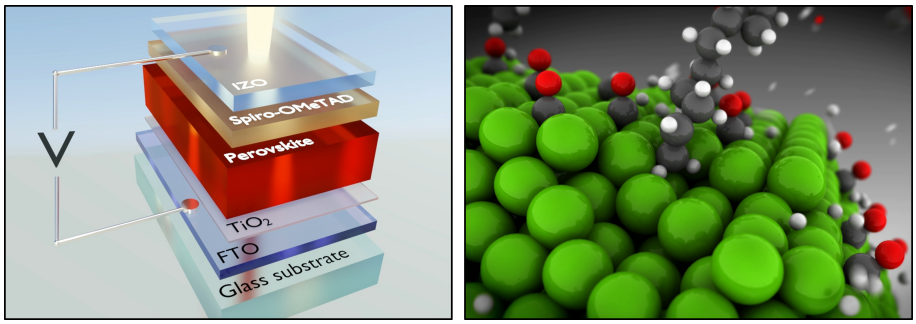


**Figure 1.1: Examples of man-made materials whose functionality is derived from order at the nano- to micrometer scale.** Solar cells (left) are commonly composed of nano/micrometer-thick layers to convert a high fraction of incident light directly into usable current. A catalyst (right) on the other hand often has the shape of a metallic nanoparticle (in green), which lowers the energy barrier of a chemical reaction. © *by Fabian Ruf / Scilight (left) and ICMS Animation Studio, TU/e (right).*[14–16]

There is an ongoing research effort to facilitate the organization of a material for a specific purpose by tuning either its shape or composition. Take for example solar cells, which in the commercial world are mostly silicon-based. Even though silicon is one of the cheapest elements on earth, the production costs of a silicon-based solar cell are still relatively high. This is because the silicon is organized as a single crystal when incorporated into a solar cell, which is done by carefully stacking it from the molecular level up.[10] Currently, a new solar cell material, perovskite, has therefore attracted much attention in the scientific community as it does not require this single crystal organisation. These perovskites thus require significantly less effort put into their organization to be functional and therefore are interesting additions or even proper competitors to silicon-based solar cells.[3,17] Hence, replacing silicon with perovskite as the composition of a solar cell may reduce the need of organization of a solar cell, while still maintaining its functionality.

This does not abolish the function of organization however, as it can also improve the performance of an already active compound. In catalysis oftentimes metal particles such as iron, nickel or cobalt are used to catalyze a myriad of processes.[18–20] Though these metals are active on their own, their performance is increased when embedded as nanoparticles on a supporting material like $SiO_2$, $Al_2O_3$ or $TiO_2$.[21–23] Moreover, by tuning organizational parameters like spacing, particle size and surface area, these supported catalysts can be tuned to increase their activity or produce specific products.[24–30] In other words, the performance of a catalyst can thus be enhanced by designing an effective organization of its active components.

Supported catalysts are also an example of functional materials formed using multiple compounds as building blocks. The functionality here can be derived from the individual building blocks, or from an interplay between them. One class of materials that demonstrate this very well are nanocomposites, materials where nanosized building blocks are incorporated into a carrier compound.[31] Functionality can be introduced along multiple length scales with this structural layout, for example by spacing the nanoparticles with a fixed distance.[32] This systematic structuring introduces new properties not found in an individual nanoparticle or their bulk counterpart, creating interesting opportunities for optical, electromagnetic or mechanical purposes.[33–36] The possibilities for these nanocomposites are increasing with each new building block found, for example with novel particle syntheses that create new compound-, size- and shape-selections.[37] Combine this with an ever-increasing list of assembly techniques, and the potential for properties programmed into nanocomposites is still yet to be fully realized.[38]

Despite tremendous progress in this field already, the current available methods are not yet all encompassing and oftentimes require ellaborous setups to shape their building blocks. These methods can generally be divided into two approaches: top-down and bottom-up.[31] With the top-down approach, materials are shaped from the macroscale down using for example 3D printing, which is limited to printable materials and is not easily scalable.[39] The bottom-up approach on the other hand is based on assembly from the molecular level up. Unfortunately, it requires pre-existing templates to guide the material in the proper shape. These templates need to be made in a cleanroom and have limited out-of-plane options.[40] There are some solutions that circumvent these problems, for instance using silk worms' fibroin to outsource the (mass-)production of a 3D template to nature.[41] This however limits the choice of shapes to those pre-fabricated by nature. Perhaps if we could understand the mechanisms used by nature to fabricate materials, we could utilise them to make our own, freely shapeable, materials.

## 1.2 Lessons from Nature

On the full timeline of our planet, mankind's conscious efforts to produce materials is a relatively new process. Organisms found in nature (i.e. animals, plants and even our own human bodies) have had a significantly longer time to develop materials required for their survival and procreation.[42,43] This has resulted in a myriad of materials with widely varied properties e.g. tough shells, colorful butterfly-wings, sharp teeth, durable spider silk and rigid bones among many other examples (Figure 1.2).[44–47] What makes the production of these varied materials even more remarkable, is that the organisms who made them only used a relatively small selection of compositions, mostly composed of polysaccharides, proteins, and minerals.[48]

Oftentimes various organisms even use the same building block to create very different materials. For example, α-keratin is used by both porcupines and sheep.[49]The former makes spiky quills out of it to protect itself from predators, while the latter makes warm wool to help regulate temperature.[50,51] So how can the same building block yield materials with such different properties? The answer to this lays in the ordering of this material. The keratin in the porcupine's quills is organized in a stiff outer sheath and a porous core, resulting in a strong, yet lightweight, defense mechanism.[52,53] Sheep's wool also consists predominately out of keratinous proteins, but these are organized into a matrix with helical shaped cells at its core.[54–56] Now, a material with mechanical and thermal properties is produced, benificial to both the sheep and the textile industry.[50,57,58] The effort nature puts in the organization of its materials thus results in specific properties derived from this organization.

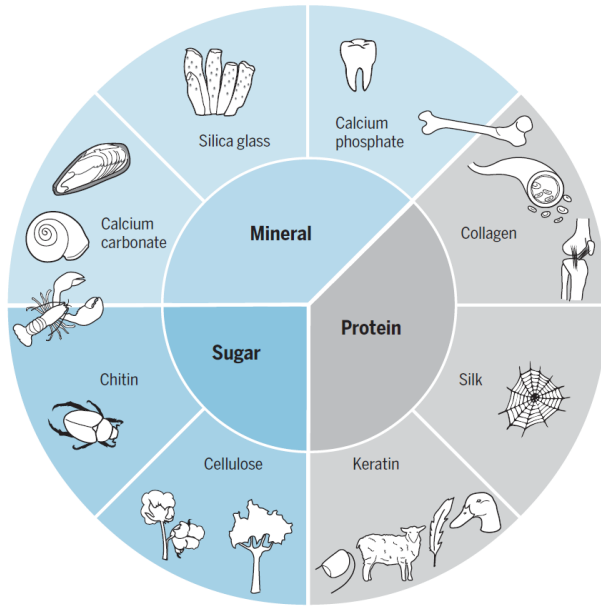


**Figure 1.2: Examples of materials produced by nature.** Even though these materials have widely varying mechanical properties and applications, they are predominantly composed of just polysaccharides, proteins and minerals. *Reprinted with permission from Eder et al., Science 2018.*[48]

Other fascinating examples of the care nature puts in organizing materials can be found in processes where living organisms produce minerals.[59] These biomineralization processes revolve for the most part around four classes of minerals: calcium carbonate, calcium phosphate, silica and magnetite.[60] Here, the shape of these minerals is vital for their performance inside the organism. For example, magnetotactic bacteria use the magnetic field lines of our planet to orient themselves.[61] They do so with special organelles called magnetosomes, in which magnetite is the magnetic component. In order to shape the magnetite to fit the organelle, the bacteria employs a special protein which single-handedly shapes the magnetite in 20-30 nm superparamagnetic crystals, making it suited for its directing purpose.[62,63]

The organization in biomineralization is also apparent in the most common of biominerals: calcium carbonate ($CaCO_3$).[60] Its crystal structure is quite shapeable, as it exists in three crystalline polymorphs: calcite, aragonite and vaterite.[64] In addition to these crystalline polymorphs, it also exists in a few amorphous states.[65] Especially amorphous $CaCO_3$ (ACC) is vital in nature, as it acts as a precursor which can be molded and crystallized to the crystalline polymorphs of $CaCO_3$.[66,67] Using an amorphous intermediate instead of direct crystallization allows sculpting of the overall crystal shape at the same time. For example, sea urchins shape their spines by crystallizing ACC into calcite. By doing so, they are able to create a single crystal of calcite in a smooth spine-shape, whereas calcite normally would grow with a faceted morphology.[67]

Nature also often combines properties of multiple compounds, creating composite materials that combine the best properties of their individual building blocks. Nacre is such a composite, consisting of aragonite crystals embedded in an organic matrix, and is found in the shells of e.g. abalones and other mollusks (Figure 1.3).[60,68–70] On its own, the hard aragonite is brittle and would provide insufficient protection as it easily fractures. On the other hand, the organic matrix is too soft to provide any protection at all. However, building a composite of aragonite platelets imbedded in the organic matrix creates a hard shell, where the envelopping organic matrix limits crack propagation to an individual platelet.[71,72] This results in a material with similar hardness to pure aragonite, but with a 3000 times higher toughness. Thus, also here nature's careful organization of compounds gives its materials their fascinating properties.

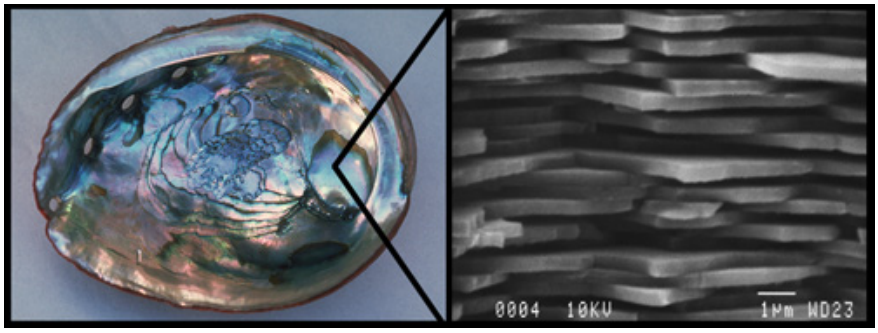


**Figure 1.3: A mollusk shell made of nacre.** Its iridescent color and crack resistant properties are derived from aragonite platelets embedded in an organic matrix. *Reprinted (adapted) with permission from Schäffer et al., Chem Matter 1997.* © *(2020) American Chemical Society.*[73]

## 1.3 Bio-inspired Materials

The remarkable properties of materials produced by nature have not gone unnoticed. In fact, whole research fields are dedicated to recreating these properties in manmade-materials.[74–76] This bio-inspired approach allows particular combinations of properties to be realized, which would otherwise be difficult to make. For example, it is well-known that hard materials are often brittle, while tough materials are often soft.[74,77] Yet, biominerals like bone and nacre are both hard and tough, because of their hierarchical ordering at the nano-to-microscale.[44,60,68,69]And even if the biomineral breaks, the organism often has ways to repair it.[67,78]Imagine the added benefit of these properties, if they could be incorporated into our own man-made materials.

Mimicking nature can be done in various ways.[74] It is possible to only mimic one aspect, e.g. the structural layout that nature produces, and with this obtain similar properties with the imitation material.[36,79] An example of this is directional freeze drying, which allows precise control over the morphology of the resulting nanocomposite.[36,80]Here, a ceramic suspension is directionally frozen with lamellar ice crystals, which expels the ceramic particles. After removing the ice a homogeneous layered ceramic scaffold is obtained, with holes where the ice originally was. By filling these holes with a soft and tough material, a nacre-like material is formed with up to twice the toughness and hardness of natural nacre. Hence, even though the assembly is very different from what nature does, the resulting nanocomposite still retains the desired combination of hardness and toughness.

A bio-inspired approach can also mimic multiple aspects of nature, for example both the structural layout and the way of assembly. Here, additive manufacturing is an interesting example.[81]In this technique materials are deposited in a layer-by-layer fashion, which shares many similarities to how nature builds materials.[82–84] These common features include the supply of building blocks in a continuous or stepwise manner, a programming code dictating the shape and local composition of the to-form material, ways to convert this code into the structural layout of the material and ways to solidify the shape after the shaping process is done.[82] By mimicking nature, materials can be produced with not only a programmable shape, but also with a tunable local structural layout.[85,86] This has resulted in materials that for example mimic the toughness of nacre, but also in self-healing materials.[87,88] Overall, this approach is believed to still have a lot of untapped potential that can bring us closer to understanding nature and its material design.

One system which mimics nature's assembly and hierarchical layout is the co-precipitation of silica ($SiO_2$) and earth alkali carbonates ($CaCO_3$, $SrCO_3$, or $BaCO_3$) (See examples in Figure 1.4).[89–96]. It was originally discovered by the group of Garcia-Ruiz, who noted that growing $BaCO_3$ in the presence of $SiO_2$ resulted in intricate microshapes with morphologies uncommon for crystals.[93,94] They dubbed these architectures 'biomorphs', as their nanocomposite layout and way of formation are very similar to those of biominerals. Yet, there is much more to these composites than only the way they form.[97] In recent years, scientists have started to functionalize these biomorphs, highlighting their nanocomposite structural layout.[98] Furthermore, their ability to be shaped also has drawn much attention, where the biomorphs act as chemically sculpted architectures.[96,99] Thus, the term 'nanocomposite' or 'architecture' is better suited when describing the biomorphs structure and shape, respectively.

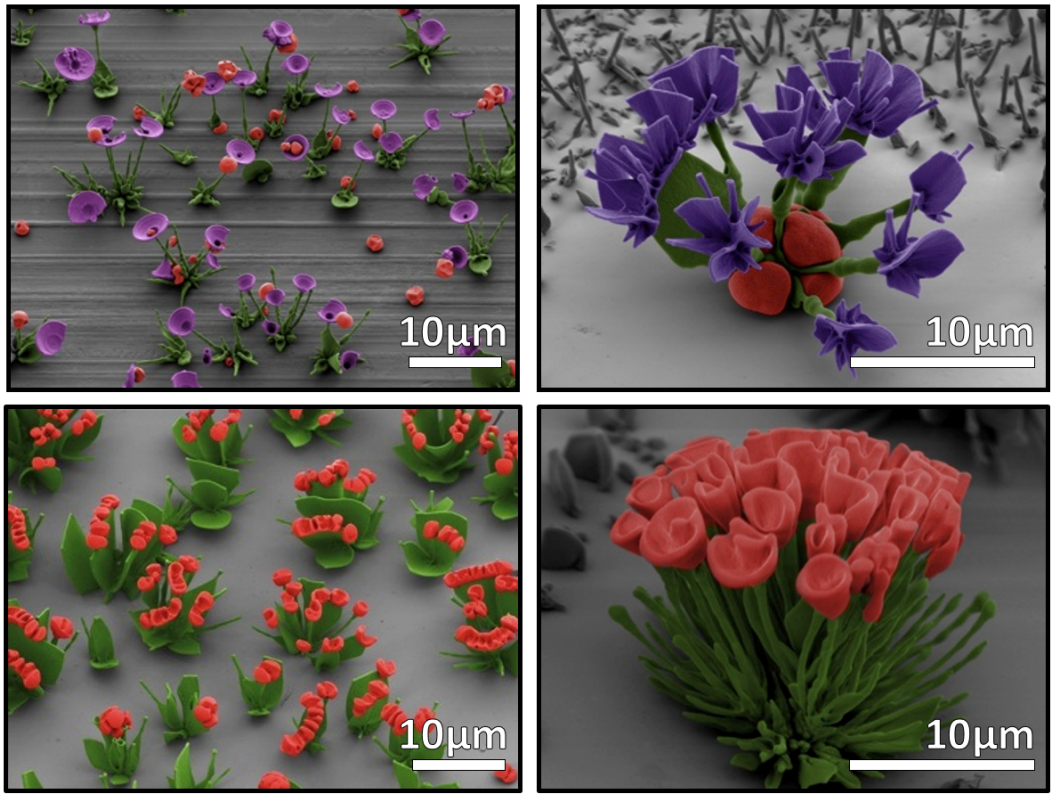


**Figure 1.4: Examples of Nanocomposite Architectures.** These architectures were produced by Noorduin *et al.* and demonstrate a selection of the possible shapes they can be programmed to have.[96]

The procedure to make these nanocomposite architectures is remarkably straightforward (Figure 1.5A). In its simplest form, all that is required is a beaker containing an aqueous solution of barium ions ($Ba^{2+}$) and metasilicate ($SiO_3{}^{2-}$). Furthermore, placing a substrate in this solution gives the architectures a place to precipitate. Then, by simply waiting, carbon dioxide ($CO_2$) will diffuse from the air into the solution and initiate the co-precipitation. From an experimental perspective, the architectures can simply be retrieved from the solution after 1.5 hours.

From a mechanistic perspective, an intriguing process is taking place in these 1,5 hours. As the $CO_2$ is taken up by the solution, bicarbonate ($HCO_3^-$) is formed which reacts with the $Ba^{2+}$ (Figure 1.5B$_1$):[96]

$$Ba^{2+}(aq) + HCO_3^{2-}(aq) \rightarrow BaCO_3(s) + H^+(aq) \tag{1.1}$$

Here, $BaCO_3$ precipitates as nanocrystals near the meniscus of the solution, while locally forming protons ($H^+$) (Figure 1.5B$_2$). The locally lowered pH around the nanocrystals instigate the second precipitation:

$$SiO_3^{2-}(aq) + 2H^+(aq) \rightarrow SiO_2(s) + H_2O(l) \tag{1.2}$$

Here, $SiO_3^{2-}$ precipitates as $SiO_2$ and forms an isolating layer around the $BaCO_3$ (Figure 1.5B$_3$). This inhibits the growth of the $BaCO_3$, which can only grow further where the $SiO_2$ is not present (Figure 1.5B$_4$). This interplay between growth and inhibition gives the architectures its intricate shape.[93,94]

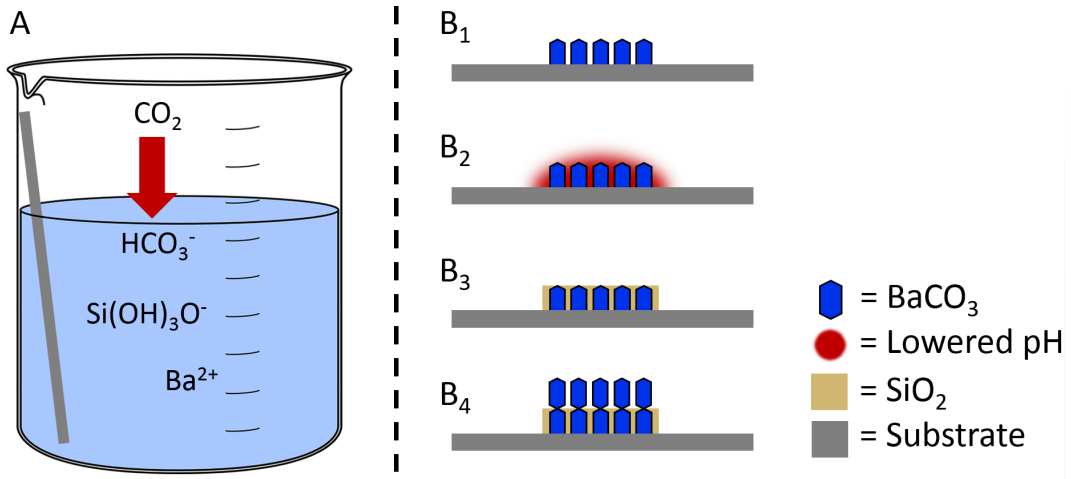


**Figure 1.5: Illustrative overview of the co-precipitation of $BaCO_3$ and $SiO_2$.** **A,** Experimental setup, which requires just an aqueous solution of $Ba^{2+}$ and $SiO_3^{2-}$. **B,** Schematic of the co-precipitation steps. **1,** $BaCO_3$ forms when $HCO_3^-$ reacts with $Ba^{2+}$(reaction 1.1). **2,** During the formation of $BaCO_3$, the acidity increases locally. **3,** $SiO_3^{2-}$ precipitates around the $BaCO_3$ because of the lowered pH (reaction 1.2). **4,** $BaCO_3$ continues to precipitate on places that have not been overgrown with $SiO_2$, restarting the cycle.

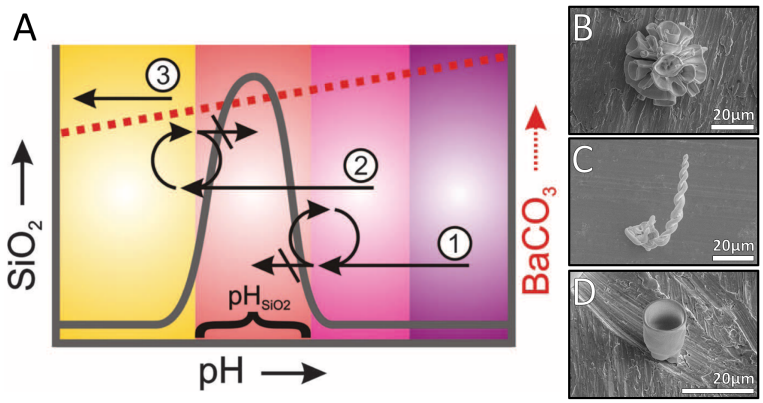


**Figure 1.6: Precipitation-rate Graph and Sculpted Architectures.** **A,** $SiO_2$ precipitation (solid gray line) occurs in a very specific pH range, while $BaCO_3$ precipitation (dashed red line) occurs over a wider pH range. The full pH range of the graph is $\sim$ 8 to 12. **B,** Coral grown at the higher pH (1) crossing point. **C,** Spiral grown at the lower pH (2) crossing point. **D,** Vase grown with a $CO_2$-pulse. *Graph (A) reprinted with permission from Noorduin et al., Science 2013.* [96]

The eventual shape of the architecture can be sculpted by manipulating growth parameters like pH, $CO_2$-concentration and temperature.[95,96] $BaCO_3$ precipitates steadily more with increased pH, whereas $SiO_2$ precipitates around a specific pH, and there exist 2 unique regimes where these precipitation rates cross each other (Figure 1.6A).[96] The co-precipitation proceeds around these two crossing points, and dictates the shape of the resulting nanoccomposite architectures. In the case of the crossing point at higher pH (starting pH=11.8), the silica precipitates away from the bulk solution, causing the $BaCO_3$ to grow towards the solution, creating coral- and stem-like shapes (Figure 1.6B). At the lower crossing point (starting pH=11.2), the silica precipitates towards the bulk solution, causing the $BaCO_3$ to grow away from the solution, creating spiral- and leaf-like shapes (Figure 1.6C). As another example, the precipitation can also temporarily be favored for $BaCO_3$ with a $CO_2$ pulse, causing a stem-like shape to expand, which after the pulse only continues to grow at the edges as the center can not get enough building blocks, causing a vase-like shape to form (Figure 1.6D). These adaptations to the synthesis provide a simple, yet powerful way to shape the resulting nanocomposites.

## 1.4 Ion Exchange

Though bio-inspired co-precipitation is an intriguing method to shape nanocomposites in 3D, it also inherits a limitation from nature: Its composition choice is limited to silica and earth alkali metals. Yet, the structural layout of a nanocomposite could potentially overcome this limitation, because during the co-precipitation the $BaCO_3$ forms as nanocrystals. Nanocrystals have a high surface area and small volume, which makes them prone to ion exchange reactions. These reactions allow the shape of the crystal to be retained, while changing its composition by either replacing its cations (cation exchange), or anions (anion exchange).[100,101]

Cation exchange is a well-established process for individual nanocrystals, and the principles behind these exchange reactions have been rationalized from a thermodynamic perspective.[102,103] In short, whether an ion exchange occurs can be estimated by comparing the association energy and solvation energy of the replacing and replaced compound.[104,105] These values can either be calculated directly, or can be estimated from the solubility constants of these compounds for a given solution.[102,106] For example, a cation exchange of a $BaCO_3$ nanocrystal to a new metal carbonate nanocrystal is likely to occur in water, as the solubility product of $BaCO_3$ in water ($5.1 \cdot 10^{-9}$) is much higher than for other metal carbonates like $CdCO_3$($5.2 \cdot 10^{-12}$), $PbCO_3$($7.4 \cdot 10^{-14}$) or $CoCO_3$ ($1.4 \cdot 10^{-13}$).[107]

Anion exchange on the other hand is more difficult. Besides thermodynamic considerations, the local reaction conditions and diffusion rates are also crucial for anion exchange reactions in particular.[102,103] Anions generally are larger than cations and diffuse slower, making them more difficult to remove from the crystal lattice.[105,108–110] Fortunately, sometimes anion exchange can be assisted by other mechanisms occuring within the anion. Such is the case with carbonate anions, who decompose at elevated temperatures.[111] During this decomposition, the crystal structure reorganizes, which can be used to change the morphology of individual nanocrystals and instigate anion reactions.[112,113].

In this thesis we explore ion-exchange reactions performed on nanocrystals in self-assembled structures. To this aim we will first co-precititate $BaCO_3/SiO_2$ into nanocomposites, and then develop ion exchange reactions that modify the chemical composition (Figure 1.7). Combined with the sculptable nature of the original $BaCO_3/SiO_2$ nanocomposites, this ion exchange potentially allows for a system where first a material is sculpted in a particular shape with co-precipitation, and then is converted to a new composition. This separates the shaping process from the eventual composition, combining bio-inspired assembly with the compound selection of manmade materials.

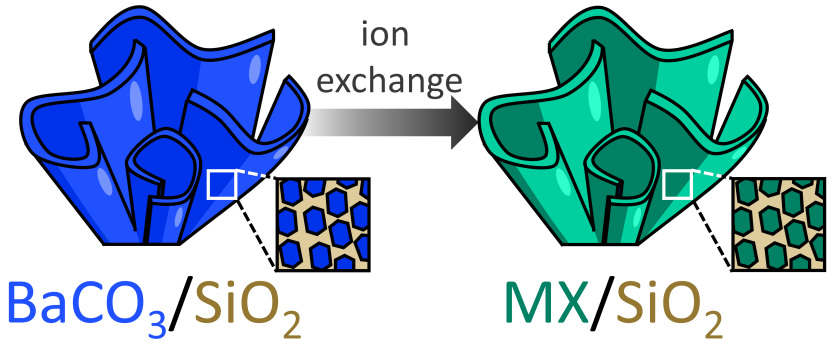


**Figure 1.7: Schematic for performing ion exchange on nanocomposites as explored in this thesis.** By performing ion exchange, we will attempt to exchange both the metal (from barium to target metal M) and the anion (from carbonate to target anion X) of the composite's nanocrystals.

## 1.5 Thesis Outline

In this thesis, we explore the possibilities of performing ion exchange reactions on $BaCO_3/SiO_2$ nanocomposites, as well as potential applications of the resulting nanocomposites.

In **Chapter 2**, we perform a case study on the conversion to CdS, with which we reveal the essential parameters of an ion exchange reaction. We then expand this case study to a general conversion plan, where we convert the nanocomposites to oxides and sulfides of cadmium, manganese, iron, nickel and cobalt. With this chapter, we establish the general parameters for an exchange reaction.

In **Chapter 3**, the nanocomposites' applicability in catalytic processes is analyzed. First, nickel nanocomposites are employed for the dry reforming of butane. Here, the catalytic activity of these nanocomposites at (desirable) low temperatures is analyzed and compared to traditional catalysts. Second, the performance of cobalt nanocomposites in the Fischer-Tropsch process is investigated. Specifically, we show that the selectivity of the resulting products can be tuned by varying the composite's nanocrystal grain size. Overall, this chapter shows that nanocomposites can act as catalysts with tunable parameters, and in some instances rival traditional catalysts.

In **Chapter 4**, we expand the conversion possibilities to non-transition metals and non-chalcogenides. For this, we first develop an exchange route to lead carbonate, a non-transition metal. The resulting nanocomposites are then converted to lead halide perovskites. This conversion demonstrates not only an anion exchange towards metal halides, but also the possibility of an ion insertion (specifically methylammonium). Furthermore, we investigate the luminescent properties of these perovskite nanocomposites, which combined with their sculptable 3D shape show potential for photovoltaic applications.

In **Chapter 5**, we investigate a conversion pathway without a carbonate intermediate. Specifically, we convert our nanocomposite architectures to tin, a metal without a stable carbonate, where the converted nanocomposite forms a tin oxy-hydroxide instead. This oxy-hydroxide intermediate possesses similar properties as a normal carbonate intermediate, and can readily be converted to both tin oxide and tin halide perovskite. This chapter shows that the cation exchange reactions performed on the nanocomposites are not limited to metal carbonates, and that many more pathways could still be discovered.

**Overall**, this thesis introduces an assembly/conversion system for nanocomposite architectures, where control over their shape and composition is seperated in two steps. We first identify the essential mechanisms with a proof-of-principle system, where $BaCO_3/SiO_2$ nanocomposites are converted into $CdS/SiO_2$ nanocomposites, while preserving their shape. We then generalize this principle to a large diversity of iron, manganese, cobalt, nickel, cadmium, lead and tin salts. Finally, we demonstrate the potential of these converted nanocomposites in catalytic and optoelectronic applications, showing how an independent control of shape and composition opens exciting new ways to create functional materials.

# Bibliography


[1] Ceruzzi, P. E. *Technology and Culture* **46**(3), 584–593 (2005).

[2] Iglesia, E. *Applied Catalysis A: General* **161**(1-2), 59–78 (1997).

[3] Kojima, A., Teshima, K., Shirai, Y., and Miyasaka, T. *Journal of the American Chemical Society* **131**(17), 6050–6051 (2009).

[4] Grady Weaver, H. *The Mainspring of Human Progress (Chapter 2).* Ludwig von Mises Institute, (1962).

[5] Edmonds, M. *Stone Tools and Society.* Routledge, (2012).

[6] Ashton, T. *The Industrial Revolution 1760-1830.* Oxford University Press, (1997).

[7] Gao, W., Zhang, Y., Ramanujan, D., Ramani, K., Chen, Y., Williams, C. B., Wang, C. C., Shin, Y. C., Zhang, S., and Zavattieri, P. D. *CAD Computer Aided Design* **69**, 65–89 (2015).

[8] Arce, P. E., Quintard, M., and Whitaker, S. In *Chemical Engineering*, volume 11, 1–39. John Wiley & Sons, Ltd, Chichester, UK oct (2005).

[9] Poole Jr., C. and Owens, F. *Introduction to Nanotechnology.* John Wiley and Sons, (2003).

[10] Shimura, F. *Single-Crystal Silicon: Growth and Properties (Chapter in Springer Handbook of Electronic and Photonic Materials).* Springer, Cham, (2017).

[11] Quinson, J., Neumann, S., Wannmacher, T., Kacenauskaite, L., Inaba, M., Bucher, J., Bizzotto, F., Simonsen, S. B., Theil Kuhn, L., Bujak, D., Zana, A., Arenz, M., and Kunz, S. *Angewandte Chemie - International Edition* **57**(38), 12338–12341 (2018).

[12] Piqué, A., Auyeung, R. C., Kim, H., Charipar, N. A., and Mathews, S. A. *Journal of Physics D: Applied Physics* **49**(22) (2016).

[13] Dumon, P., Bogaerts, W., Wiaux, V., Wouters, J., Beckx, S., Van Campenhout, J., Taillaert, D., Luyssaert, B., Bienstman, P., Van Thourhout, D., and Baets, R. *IEEE Photonics Technology Letters* **16**(5), 1328–1330 (2004).

[14] Ruf, F., Magin, A., Schultes, M., Ahlswede, E., Kalt, H., and Hetterich, M. *Applied Physics Letters* **112**(8) (2018).

[15] Van Santen, R. A., Ghouri, M. M., Shetty, S., and Hensen, E. M. *Catalysis Science and Technology* **1**(6), 891–911 (2011).

[16] Shetty, S. G., Ciobîcă, I. M., Hensen, E. J., and Van Santen, R. A. *Chemical Communications* **47**(35), 9822–9824 (2011).

[17] Green, M. A., Ho-Baillie, A., and Snaith, H. J. *Nature Photonics* **8**(7), 506–514 (2014).

[18] Khodakov, A. Y., Chu, W., and Fongarland, P. *Chemical Reviews* **107**(5), 1692–1744 (2007).

[19] Sivula, K., Le Formal, F., and Grätzel, M. *ChemSusChem* **4**(4), 432–449 (2011).

[20] Fan, M. S., Abdullah, A. Z., and Bhatia, S. *ChemCatChem* **1**(2), 192–208 (2009).

[21] Yu, J., Yu, J., Shi, Z., Guo, Q., Xiao, X., Mao, H., and Mao, D. *Catalysis Science and Technology* **9**(14), 3675–3685 (2019).

[22] Trueba, M. and Trasatti, S. P. *European Journal of Inorganic Chemistry* (17), 3393–3403 (2005).

[23] Lomate, S., Sultana, A., and Fujitani, T. *Catalysis Science and Technology* **7**(14), 3073–3083 (2017).

[24] Murdoch, M., Waterhouse, G. I., Nadeem, M. A., Metson, J. B., Keane, M. A., Howe, R. F., Llorca, J., and Idriss, H. *Nature Chemistry* **3**(6), 489–492 (2011).

[25] Bezemer, G. L., Bitter, J. H., Kuipers, H. P., Oosterbeek, H., Holewijn, J. E., Xu, X., Kapteijn, F., Van Diilen, A. J., and De Jong, K. P. *Journal of the American Chemical Society* **128**(12), 3956–3964 (2006).

[26] van Santen, R. A. *Accounts of Chemical Research* **42**(1), 57–66 (2009).

[27] Parlett, C. M., Wilson, K., and Lee, A. F. *Chemical Society Reviews* **42**(9), 3876–3893 (2013).

[28] Sudarsanam, P., Peeters, E., Makshina, E. V., Parvulescu, V. I., and Sels, B. F. *Chemical Society Reviews* **48**(8), 2366–2421 (2019).

[29] Munnik, P., De Jongh, P. E., and De Jong, K. P. *Chemical Reviews* **115**(14), 6687–6718 (2015).

[30] Prieto, G., Zečević, J., Friedrich, H., De Jong, K. P., and De Jongh, P. E. *Nature Materials* **12**(1), 34–39 (2013).

[31] Begley, M. R., Gianola, D. S., and Ray, T. R. *Science* **364**(6447), eaav4299 jun (2019).

[32] Kovalenko, M. V., Manna, L., Cabot, A., Hens, Z., Talapin, D. V., Kagan, C. R., Klimov, V. I., Rogach, A. L., Reiss, P., Milliron, D. J., Guyot-Sionnnest, P., Konstantatos, G., Parak, W. J., Hyeon, T., Korgel, B. A., Murray, C. B., and Heiss, W. *ACS Nano* **9**(2), 1012–1057 (2015).

[33] Llordés, A., Garcia, G., Gazquez, J., and Milliron, D. J. *Nature* **500**(7462), 323–326 (2013).

[34] Choi, J. H., Wang, H., Oh, S. J., Paik, T., Jo, P. S., Sung, J., Ye, X., Zhao, T., Diroll, B. T., Murray, C. B., and Kagan, C. R. *Science* **352**(6282), 205–208 (2016).

[35] Casini, M. *Renewable Energy* **119**, 923–934 (2018).

[36] Deville, S., Saiz, E., Nalla, R. K., and Tomsia, A. P. *Science* **311**(5760), 515–518 (2006).

[37] Boles, M. A., Engel, M., and Talapin, D. V. *Chemical Reviews* **116**(18), 11220–11289 (2016).

[38] Levchenko, I., Bazaka, K., Keidar, M., Xu, S., and Fang, J. *Advanced Materials* **30**(2), 1–32 (2018).

[39] Murray, C. B., Kagan.R. and M.G., B. *Annu. Rev. Mater. Sci.* **30**, 545–610 (2006).

[40] Tan, A. T., Beroz, J., Kolle, M., and Hart, A. J. *Advanced Materials* **30**(44), 1–7 (2018).

[41] Wang, Y., Aurelio, D., Li, W., Tseng, P., Zheng, Z., Li, M., Kaplan, D. L., Liscidini, M., and Omenetto, F. G. *Advanced Materials* **29**(38), 1–9 (2017).

[42] Meyers, M. A., Chen, P. Y., Lin, A. Y. M., and Seki, Y. *Progress in Materials Science* **53**(1), 1–206 (2008).

[43] Thompson, D. *On Growth and Form*. Cambridge University Press, (2014).

[44] Rho, J. Y., Kuhn-Spearing, L., and Zioupos, P. *Medical Engineering and Physics* **20**(2), 92–102 (1998).

[45] Studart, A. R. *Nature Materials* **13**(5), 433–435 (2014).

[46] Gosline, J. M., Guerette, P. A., Ortlepp, C. S., and Savage, K. N. *Journal of Experimental Biology* **202**(23), 3295–3303 (1999).

[47] Vukusic, P., Sambles, J. R., and Lawrence, C. R. *Nature* **404**(6777), 457 (2000).

[48] Eder, M., Amini, S., and Fratzl, P. *Science* **362**(6414), 543–547 (2018).

[49] Wang, B., Yang, W., McKittrick, J., and Meyers, M. A. *Progress in Materials Science* **76**, 229–318 (2016).

[50] Haly, A. R. and Snaith, J. W. *Biopolymers* **6**(9), 1355–1377 (1968).

[51] Vincent, J. F. and Owers, P. *Journal of Zoology* **210**(1), 55–75 (1986).

[52] McKittrick, J., Chen, P. Y., Bodde, S. G., Yang, W., Novitskaya, E. E., and Meyers, M. A. *Jom* **64**(4), 449–468 (2012).

[53] Yang, W., Chao, C., and McKittrick, J. *Acta Biomaterialia* **9**(2), 5297–5304 (2013).

[54] Lewis, D. and Rippon, J. *The Coloration of Wool and other Keratin Fibres*. John Wiley and Sons, (2013).

[55] Rivett, D., Ward, C., Belkin, L., J.A.M., R., and Wilshire, J. *The Lennox Legacy*. Csiro Publishing, (1996).

[56] Fan, J., Yang, X., and Liu, Y. *Journal of Engineered Fibers and Fabrics* **14**, 1–3 (2019).

[57] Feughelman, M. and Haly, A. R. *Kolloid-Zeitschrift* **168**(2), 107–115 (1960).

[58] Zach, J., Korjenic, A., Petránek, V., Hroudová, J., and Bednar, T. *Energy and Buildings* **49**, 246–253 (2012).

[59] Vert, M., Doi, Y., Hellwich, K. H., Hess, M., Hodge, P., Kubisa, P., Rinaudo, M., and Schué, F. *Pure and Applied Chemistry* **84**(2), 377–410 (2012).

[60] Nudelman, F. and Sommerdijk, N. A. *Angewandte Chemie - International Edition* **51**(27), 6582–6596 (2012).

[61] Lin, W., Zhang, W., Zhao, X., Roberts, A. P., Paterson, G. A., Bazylinski, D. A., and Pan, Y. *ISME Journal* **12**(6), 1508–1519 (2018).

[62] Arakaki, A., Webb, J., and Matsunaga, T. *Journal of Biological Chemistry* **278**(10), 8745–8750 (2003).

[63] Prozorov, T., Mallapragada, S. K., Narasimhan, B., Wang, L., Palo, P., Nilsen-Hamilton, M., Williams, T. J., Bazylinski, D. A., Prozorov, R., and Canfield, P. C. *Advanced Functional Materials* **17**(6), 951–957 (2007).

[64] Morse, J. W., Arvidson, R. S., and Lüttge, A. *Chemical Reviews* **107**(2), 342–381 (2007).

[65] Addadi, L., Raz, S., and Weiner, S. *Advanced Materials* **15**(12), 959–970 (2003).

[66] Weiss, I. M., Tuross, N., Addadi, L., and Weiner, S. *Journal of Experimental Zoology* **293**(5), 478–491 (2002).

[67] Politi, Y., Arad, T., Klein, E., Weiner, S., and Addadi, L. *Science* **306**(5699), 1161–1164 (2004).

[68] Addadi, L., Joester, D., Nudelman, F., and Weiner, S. *Chemistry - A European Journal* **12**(4), 980–987 (2006).

[69] Smith, B. L., Schäffer, T. E., Vlani, M., Thompson, J. B., Frederick, N. A., Klndt, J., Belcher, A., Stucky, G. D., Morse, D. E., and Hansma, P. K. *Nature* **399**(6738), 761–763 (1999).

[70] Barthelat, F., Yin, Z., and Buehler, M. J. *Nature Reviews Materials* **1** (2016).

[71] Currey, J. D. *Proceedings of the Royal Society of London - Biological Sciences* **196**(1125), 443–463 (1977).

[72] Jackson, A., Vincent, J., and Turner, R. *Proceedings of the Royal Society of London. Series B. Biological Sciences* **234**(1277), 415–440 (1988).

[73] Schäffer, T. E., Ionescu-Zanetti, C., Proksch, R., Fritz, M., Walters, D. A., Almqvist, N., Zaremba, C. M., Belcher, A. M., Smith, B. L., Stucky, G. D., Morse, D. E., and Hansma, P. K. *Chemistry of Materials* **9**(8), 1731–1740 (1997).

[74] Wegst, U. G., Bai, H., Saiz, E., Tomsia, A. P., and Ritchie, R. O. *Nature Materials* **14**(1), 23–36 (2015).

[75] Studart, A. R. *Advanced Materials* **24**(37), 5024–5044 (2012).

[76] Aizenberg, J. and Fratzl, P. *Advanced Functional Materials* **23**(36), 4398–4399 (2013).

[77] Ritchie, R. O. *Nature Materials* **10**(11), 817–822 (2011).

[78] Kanczler, J. M. and Oreffo, R. O. *European Cells and Materials* **15**, 100–114 (2008).

[79] Hager, B. M. D., Greil, P., Leyens, C., Zwaag, S. V. D., and Schubert, U. S. *Advanced Materials* **22**, 5424–5430 (2010).

[80] Munch, E., Launey, M. E., Alsem, D. H., Saiz, E., Tomsia, A. P., and Ritchie, R. O. *Science* **322**(5907), 1516–1520 (2008).

[81] Studart, A. R. *Chemical Society Reviews* **45**(2), 359–376 (2016).

[82] Calvert, P. and Crockett, R. *Chemistry of Materials* **9**(3), 650–663 (1997).

[83] Villar, G., Graham, A. D., and Bayley, H. *Science* **340**(6128), 48–52 (2013).

[84] Fu, Q., Saiz, E., and Tomsia, A. P. *Advanced Functional Materials* **21**(6), 1058–1063 (2011).

[85] Dimas, L. S., Bratzel, G. H., Eylon, I., and Buehler, M. J. *Advanced Functional Materials* **23**(36), 4629–4638 (2013).

[86] Lewis, J. A. *Advanced Functional Materials* **16**(17), 2193–2204 (2006).

[87] Dimas, L. S. and Buehler, M. J. *Soft Matter* **10**(25), 4436–4442 (2014).

[88] Toohey, K. S., Sottos, N. R., Lewis, J. A., Moore, J. S., and White, S. R. *Nature Materials* **6**(8), 581–585 (2007).

[89] Nakouzi, E., Knoll, P., and Steinbock, O. *Chemical Communications* **52**(10), 2107–2110 (2016).

[90] Zhang, G., Morales, J., and García-Ruiz, J. M. *Journal of Materials Chemistry B* **5**(8), 1658–1663 (2017).

[91] Kellermeier, M., Cölfen, H., and García-Ruiz, J. M. *European Journal of Inorganic Chemistry* (32), 5123–5144 (2012).

[92] Knoll, P. and Steinbock, O. *Israel Journal of Chemistry* **58**(6), 682–692 (2018).

[93] Garcia-Ruiz, J. M., Melero-Garcia, E., and Hyde, S. T. *Science* **323**(5912), 362–365 (2009).

[94] Garcia-Ruiz, J. M. *Science* **302**(5648), 1194–1197 (2003).

[95] Kaplan, C. N., Noorduin, W. L., Li, L., Sadza, R., Folkertsma, L., Aizenberg, J., and Mahadevan, L. *Science* **355**(6332), 1395–1399 (2017).

[96] Noorduin, W. L., Grinthal, A., Mahadevan, L., and Aizenberg, J. *Science* **340**(6134), 832–837 (2013).

[97] Cölfen, H. *Physics of Life Reviews* **1**, 6–8 (2020).

[98] Opel, J., Wimmer, F. P., Kellermeier, M., and Cölfen, H. *Nanoscale Horizons* **1**(2), 144–149 (2016).

[99] Opel, J., Kellermeier, M., Sickinger, A., Morales, J., Cölfen, H., and García-Ruiz, J. M. *Minerals* **8**(2), 1–12 (2018).

[100] Boneschanscher, M. P., Evers, W. H., Geuchies, J. J., Altantzis, T., Goris, B., Rabouw, F. T., van Rossum, S. A. P., van der Zant, H. S. J., Siebbeles, L. D. A., Van Tendeloo, G., Swart, I., Hilhorst, J., Petukhov, A. V., Bals, S., and Vanmaekelbergh, D. *Science* **344**(6190), 1377–1380 (2014).

[101] Holtus, T., Helmbrecht, L., Hendrikse, H. C., Baglai, I., Meuret, S., Adhyaksa, G. W., Garnett, E. C., and Noorduin, W. L. *Nature Chemistry* **10**(7), 740–745 (2018).

[102] De Trizio, L. and Manna, L. *Chemical Reviews* **116**(18), 10852–10887 (2016).

[103] Beberwyck, B. J., Surendranath, Y., and Alivisatos, A. P. *Journal of Physical Chemistry C* **117**(39), 19759–19770 (2013).

[104] Dong, H. S., Hughes, S. M., Yin, Y., and Alivisatos, A. P. *Science* **306**(5698), 1009–1012 (2004).

[105] Rivest, J. B. and Jain, P. K. *Chemical Society Reviews* **42**(1), 89–96 (2013).

[106] Moon, G. D., Ko, S., Xia, Y., and Jeong, U. *ACS Nano* **4**(4), 2307–2319 (2010).

[107] *Solubility Product Constants*, (University of Rhode Island, accessed on 29-08-2020), https://www.chm.uri.edu/weuler/chm112/refmater/KspTable.html.

[108] Dloczik, L. and Könenkamp, R. *Nano Letters* **3**(5), 651–653 (2003).

[109] Huang, C. M., Cheng, S. H., Jeng, U. S., Yang, C. S., and Lo, L. W. *Nano Research* **5**(9), 654–666 (2012).

[110] Dloczik, L. and Koenenkamp, R. *Journal of Solid State Electrochemistry* **8**(3), 142–146 (2004).

[111] Mu, J. and Perlmutter, D. *Thermochimica Acta* **49**(2-3), 207–218 nov (1981).

[112] Yu, H., Wang, D., and Han, M. Y. *Journal of the American Chemical Society* **129**(8), 2333–2337 (2007).

[113] Wu, J., Yao, Y. C., Dai, Y. N., and Yang, B. *Advanced Materials Research* **443-444**, 594–600 (2012).

# Chapter 2

## Ion Exchange to Metal Chalcogenides

Forging customizable compounds into arbitrary shapes and structures has the potential to revolutionize functional materials and technology—where independent control over shape and composition is essential. Current self-assembly strategies allow impressive levels of control over either shape or chemical composition, but not both, as self-assembly inherently entangles shape and composition. In this chapter we demonstrate independent control over shape and composition by performing chemical conversion reactions on nanocrystals which were first self-assembled in nanocomposites with programmable microscopic shapes. The multiscale character of nanocomposites is crucial: we show that nanocrystals offer enhanced chemical reactivity, while the composite layout accommodates volume changes of the nanocrystals, which together leads to complete chemical conversion with full shape preservation at the microscale. We show that these conversion reactions are surprisingly materials agnostic, allowing a large diversity of chemical pathways, and develop conversion pathways yielding a wide selection of shape-controlled transition metal chalcogenides.

This work has been published as:

Hendrikse, H.C., van der Weijden, A., Ronda-Lloret, M., Yang, T., Bliem, R., Raveendran Shiju, N., van Hecke, M., Li, L., and Noorduin, W.L., *Shape-Preserving Chemical Conversion of Architected Nanocomposites*, Advanced Materials, 32(52), 2003999 (2020).

Hans C. Hendrikse and Arno van der Weijden contributed equally.

## 2.1 Introduction

All around us, living organisms assemble three-dimensional (3D) geometries with staggering complexity and sub-micron precision.[1–4] This has inspired synthetic assembly strategies to produce highly complex 3D shapes using simple methods.[4–16] Unfortunately, in both cases the choice of chemical compositions is limited. Alternatively, a wide selection of compositions can be reached by nanoparticle synthesis,[16–25] but assembling these in arbitrary microscopic 3D shapes has remained challenging. Synthesis inherently entangles shape and composition; hence, current assembly routes offer control over either 3D shape or composition, but not both.

In principle, chemically converting existing 3D shapes to a specified composition allows control over both the chemical composition and 3D geometry. The viability of this strategy is indicated by naturally occurring geochemical fossilization processes,[1] and laboratory demonstrations of shape preserving ion-exchange and oxidation/reduction reactions on individual and ensembles of nanocrystals, as well as biominerals.[5,21–26] Nevertheless, conversion of arbitrary microscopic architectures is still challenging as conversion is diffusion-limited and slow, and significant changes in the atomistic unit cells could yield uncontrollable dissolution/recrystallization, large deformations, and even fracture failure.

We recognize that successful conversion reactions require a paradoxical combination of reactivity and stability to enable: (i) diffusion of reactants and products in the solid phase, (ii) crystal lattice rearrangements and unit-cell volume changes, while (iii) preserving the overall 3D shape. We thus hypothesize that nanocomposites consisting of nanocrystals in an amorphous matrix have excellent characteristics to overcome these issues. Traditionally, nanocomposites have mainly been studied for their excellent mechanical properties.[1,2,5,6,13,14] Importantly, already a wide diversity of shape-controlled microscopic nanocomposites can be assembled by controlling the coprecipitation of calcium-, strontium-, and barium carbonate salts with amorphous silica.[7–10] The resulting nanocomposites have limited functionalities by themselves, but we note that many interesting metal compounds form carbonate salts with closely related crystal structures. This facilitates ion-exchange with minimal rearrangements of the crystal lattice towards a wide range of metal chalcogenides with interesting chemical and electronic properties.

In this chapter we show that the unique structuring across length scales of nanocomposites enables a versatile and surprisingly amenable shape-preserving conversion strategy, thus enabling a complete uncoupling of the 3D shape from the chemical composition. We do so by first programming the nanocomposite in a pre-programmed shape (e.g. a coral-, spiral-, vase-, or post-like shapes, see Figure 2.1A). Then, we employ a two step conversion pathway, where consecutively a cation and anion exchange takes place (Figure 2.1B). This pathway first converts the nanocrystals inside the composite to a target metal carbonate. Second, these metal carbonates are thermally excited to convert them into metal chalcogenides and perovskites, compounds with various application potential (The latter conversion is discussed in Chapter 4 and 5).[27,28]

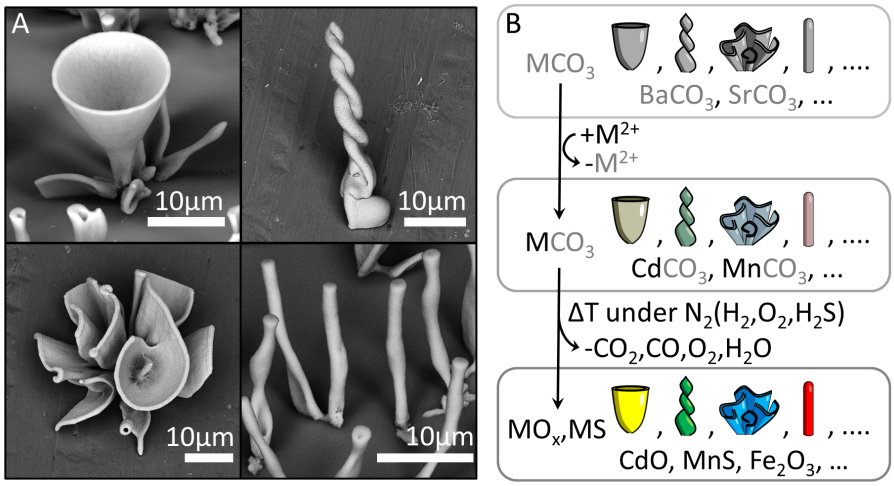


**Figure 2.1: Synthesis approach for nanocomposites with independent control over shape and composition. A,** Scanning electron microscopy (SEM) images of example $BaCO_3/SiO_2$ nanocomposites sculpted to have a vase-, spiral-, coral- and post-like shape. **B,** Plan for converting the $BaCO_3$ nanocrystals of the composite to new materials. First, a cation exchange changes the nanocrystals to a new metal carbonate. Second, thermal excitation allows a change in anion to form for example metal oxides or sulfides.

## 2.2 Proof-of-Principle: Conversion to CdS

We investigate the general processes for these shape-preserving conversion reactions by studying a representative case: the conversion of barium carbonate ($BaCO_3$) to cadmium sulfide (CdS) in coral-shaped $BaCO_3/SiO_2$ nanocomposites. The initial $BaCO_3/SiO_2$ coral-like shapes are synthesized following previously developed procedures (see Appendix A.1.1).[8–10] Our proposed conversion scheme is then employed (Figure 2.1), which is motivated by the solubilities, chemical reactivities, and crystallographic similarities of orthorhombic $BaCO_3$, the intermediate trigonal $CdCO_3$, and trigonal CdS.[26,29]

First, $BaCO_3$ is converted to $CdCO_3$ by immersing the shapes into an aqueous solution of $CdCl_2$ (50 mM) at room temperature for 10 minutes (Figure 2.2, see Appendix A.1.2 for details). This cation exchange is driven towards the formation of $CdCO_3$ by the thousand-fold lower solubility of $CdCO_3$ ($K_{sp,CdCO_3} = 1.0 \cdot 10^{-12}$) compared to $BaCO_3$ ($K_{sp,BaCO_3} = 2.58 \cdot 10^{-9}$), and the excess amount of $Cd^{2+}$ in the solution. Second, $CdCO_3$ is converted to CdS in $H_2S/N_2$ 10/90 vol% at 1 bar and 290 °C for 4 hours. This anion exchange is facilitated by the release of $H_2O$ and $CO_2$. Scanning electron microscopy (SEM) shows excellent preservation of the 3D microscopic shape (Figure 2.2B), while X-ray powder diffraction (XRD) and energy dispersion spectroscopy (EDS) analysis confirm the complete chemical conversion to yield trigonal $CdCO_3$ in step 1, and trigonal CdS in step 2 (Figure 2.2E,F).

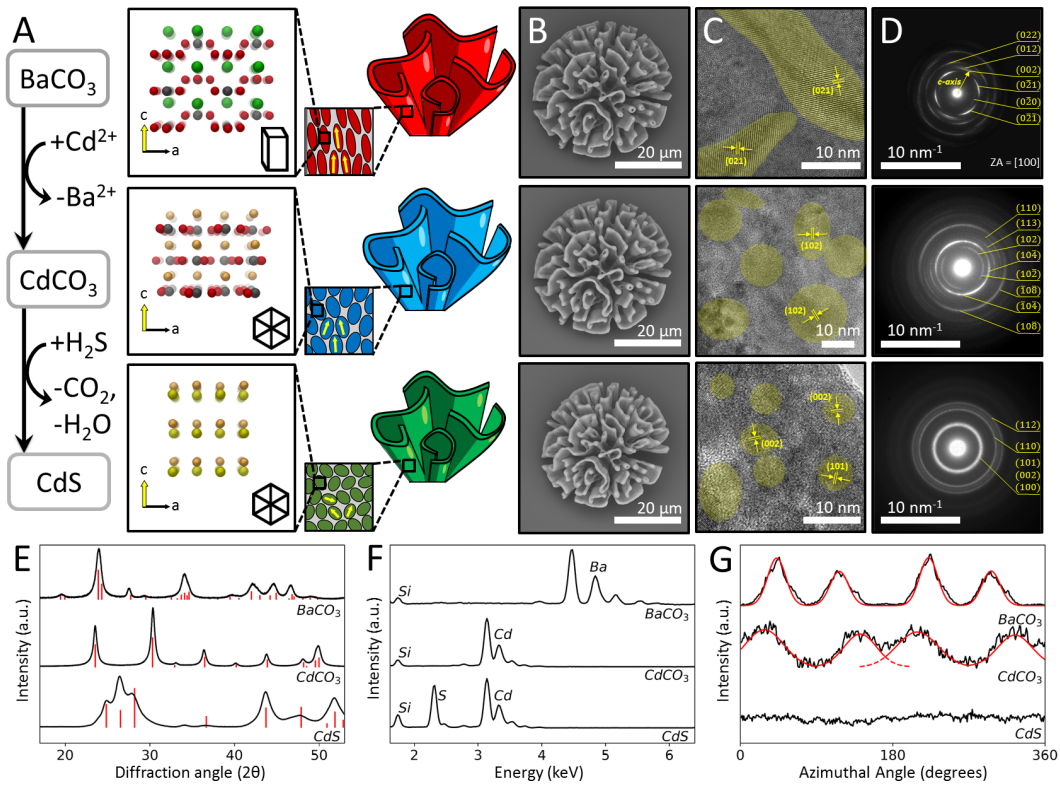


**Figure 2.2: Shape-preserving conversion in nanocomposites.** **A,** Reaction steps, crystal structures, and schematic hierarchical organization of the nanocomposites. **B,** SEM backscatter images of the same architecture showing shape preservation and volume adjustment after each reaction step. **C,** TEM imaging of FIB-sectioned architectures show preservation of crystallinity and nanocomposite layout after each reaction step, nanocrystallites highlighted in color (See Appendix A.2.3 for details). **D,** SAED on cross-sections show preservation of crystallinity, crystallographic orientation of the c-axis indicted by yellow arrow. **E,** XRD, and **F,** EDS confirm complete chemical conversion (red lines indicate XRD spectra of the expected products). XRD peak broadening is consistent with the observed nanocrystal sizes in C. **G,** Demonstration of crystallographic misorientations by integrating selected diffraction peaks with respect to the azimuthal angle from the SAED data in D. The diffraction peaks used for analysis are $(0\bar{2}1)/(0\bar{2}\bar{1})/(02\bar{1})/(021)$, $(10\bar{2})/(102)/(\bar{1}02)/(\bar{1}0\bar{2})$, and $(101)/(002)/(100)$ peaks for $BaCO_3$, $CdCO_3$, and CdS, respectively. The black and red lines represent the experimental and fitting results respectively.

To disentangle the mechanism underlying microscopic shape preservation during (volume) changes of the crystallographic unit cells, we compare architectures before and after each exchange step at various length scales. During the intermediate conversion of $BaCO_3$ to $CdCO_3$ the volume of the crystal lattice shrinks by ca. 25% (comparing crystallographic data of COD1000033 and AMCSD0004324). However, comparison of the microscopic shape before and after the conversion to $CdCO_3$ shows no volume change, suggesting the formation of nanopores in the composite (Figure 2.2, Appendix A.2.8). During the final conversion from $CdCO_3$ to CdS, the volume of

the crystal lattice shrinks an additional 11% (comparing AMCSD0004324 with COD1011054), and the volume of the microscopic shape shrinks almost 30%, implying the disappearance of the nanoporosity. Indeed, the volume change of the overall conversion of $BaCO_3$ to CdS (33%) is almost identical for the crystal structure volume and microscopic shape (30%, Appendix A.2.8): volume changes of the crystal lattice are thus translated to mesoscale volume changes of the architecture.

Remarkably, albeit shrunken, the final CdS microshape is geometrically indistinguishable from the original one; even sub-micrometer details remain preserved. We follow the conversion processes at the nanoscale using transmission electron microscopy (TEM) imaging and selected-area electron diffraction (SAED). In the original $BaCO_3/SiO_2$ nanocomposites, the $BaCO_3$ nanocrystals exhibit rod-like morphologies (length, ca. 20-50 nm; width, ca. 5-10 nm) (Figure 2.2C)[8,10] which are preferentially oriented with the c-axis along the growth direction of the nanocomposite (Figure 2.2D, Appendix A.2.3). The azimuthally integrated intensity profile of selected diffraction peaks allows us to estimate the crystallographic misorientation distribution of ca. 25° within the silica matrix (Figure 2.2D,G, Appendix A.2.3). Facilitated by the similarities between the crystal structures, this preferred co-alignment along the c-axis is maintained after the conversion to trigonal $CdCO_3$, although the misorientation distribution increases to ca. 50° (Figure 2.2D). In addition, the $CdCO_3$ crystals slightly shrink to ca. 20 nm and appear to lose their rod-like morphologies. During the more profound rearrangement of the crystal structure into trigonal CdS the nanocrystals shrink further to 5-10 nm and become randomly oriented (Figure 2.2D). Throughout these transformations, the silica matrix is preserved and the nanocrystals remain embedded in the matrix (Figure 2.2C). We conclude that, at the nanoscale, the matrix adapts to the shape transformations and reorientations at the nanoscale while preserving the overall shape at the microscale.

## 2.3 General Pathway Design

Complete chemical conversion requires rapid transport of ions towards and away from the nanocrystals through the entire architecture. We envisage that the interconnected silica matrix, which constitutes ca. 20-25 at.% of the overall composite, can facilitate this transport. Consistent with this hypothesis, deliberately crosslinking the silica matrix by heating hinders the diffusion of ions and thereby leads to incomplete conversion. In addition, removing the silica matrix results in poor conversion or even destruction of the architectures, thus emphasizing the role of the percolating matrix for both transport and stabilization of the overall shape.

Overall, the multiscale character of nanocomposites is perfectly suited for the essential processes of/during shape-preserving conversion reactions. The large surface to volume ratio of the nanocrystals enhances chemical reactivity, the percolating silica matrix enables transport of ions, and the composite layout provides mechanical stability for preserving the overall morphology during expansion and shrinkage of the crystal unit cell.

These insights suggest that the conversion pathway is rather material agnostic, as long as the target nanocrystal forms a carbonate intermediate. Thus, shape-preserving conversion can be achieved for a wide palette of chemical compositions and shapes by taking advantage of the nanocomposite layout. To demonstrate this, we design a general conversion pathway towards metal chalcogenides which are of wide interest for their chemical and electronic properties,[27] and where control over their form offers improved or even novel applications. Our strategy is motivated by the following considerations: (i) many relevant transition metals form carbonates,[29] which facilitates cation exchange, (ii) many metal carbonates crystallize in the same or related crystal structures, which facilitates cation exchange with a minimal distortion of the anionic framework, (iii) the carbonate anion can act as a good leaving group for introducing the desired oxide or sulfide, and (iv) the oxidation state of the metal can be controlled by applying either oxidative or reductive conditions.

To demonstrate that our process is essentially independent of the shape of the nanocomposite and the details of the chemical pathway, we converted $BaCO_3/SiO_2$ nanocomposites (e.g. coral-, spiral-, vase-, and post-like shapes) into a range of cadmium-, iron-, manganese-, cobalt- and nickel- oxides and sulfides. SEM analysis, EDS mapping, and XRD confirm the chemical conversion with preservation of the microscopic geometry and nanocomposite layout (Figure 2.3, see Appendix A.1 for synthesis procedures).

We find that the nanocomposite layout supports the formation of both crystalline and amorphous carbonate intermediates. In particular, iron, nickel and cobalt carbonates are known to form amorphous instead of crystalline solid phases.[30–32] Indeed, an amorphous phase is found after the conversion of $BaCO_3$ into the carbonate salts of these materials (see Appendix A.1.4 and A.1.5). Nevertheless, conversion of this amorphous phase still yields the desired metal oxide while preserving the overall shape and fine details of the initial architecture.

Moreover, a large range of metal chalcogenides with various crystal structures (e.g. orthorhombic, cubic, tetragonal, trigonal) can be obtained by controlling the reaction conditions during conversion. For example, $Mn(II)CO_3$ shapes are converted into manganese oxides with various crystal structures and oxidation states by controling the reaction conditions in the second step. Specifically, heating $Mn(II)CO_3$ microshapes under inert $N_2$ flow to 540 °C results in the exclusive formation of tetragonal $Mn(II,III)_3O_4$ within 13 hours. Applying reductive conditions using a flow of $H_2$ converts $Mn(II)CO_3$ shapes into cubic Mn(II)O, whereas oxidative conditions obtained by heating under $O_2$ results into the complete conversion of $Mn(II)CO_3$ into orthorhombic $\alpha$-$Mn(III)_2O_3$.

This control over oxidation state and flexibility in crystal structure holds true for all formed metal salts. In the case of iron, the oxidation state of the metal oxide product can be controlled to yield preprogrammed shapes such as stems, vases or corals of magnetite (cubic $Fe(II,III)_3O_4$) under inert conditions at 570 °C, hematite (trigonal $\alpha$-$Fe(III)_2O_3$) under oxidative conditions with $O_2$ at 570 °C, and even metallic iron (cubic $\delta$-Fe) under reductive conditions with $H_2$ at 400 °C. Finally, cobalt can be tuned to $Co_3O_4$ or CoO by either performing the reaction under oxidative conditions with 20 vol.% $O_2$ or under a pure $N_2$ environment respectively. Overall, these two-step reaction pathways thus offer systematic routes towards a wide range of relevant metal chalcogenides with independent control over shape and composition.

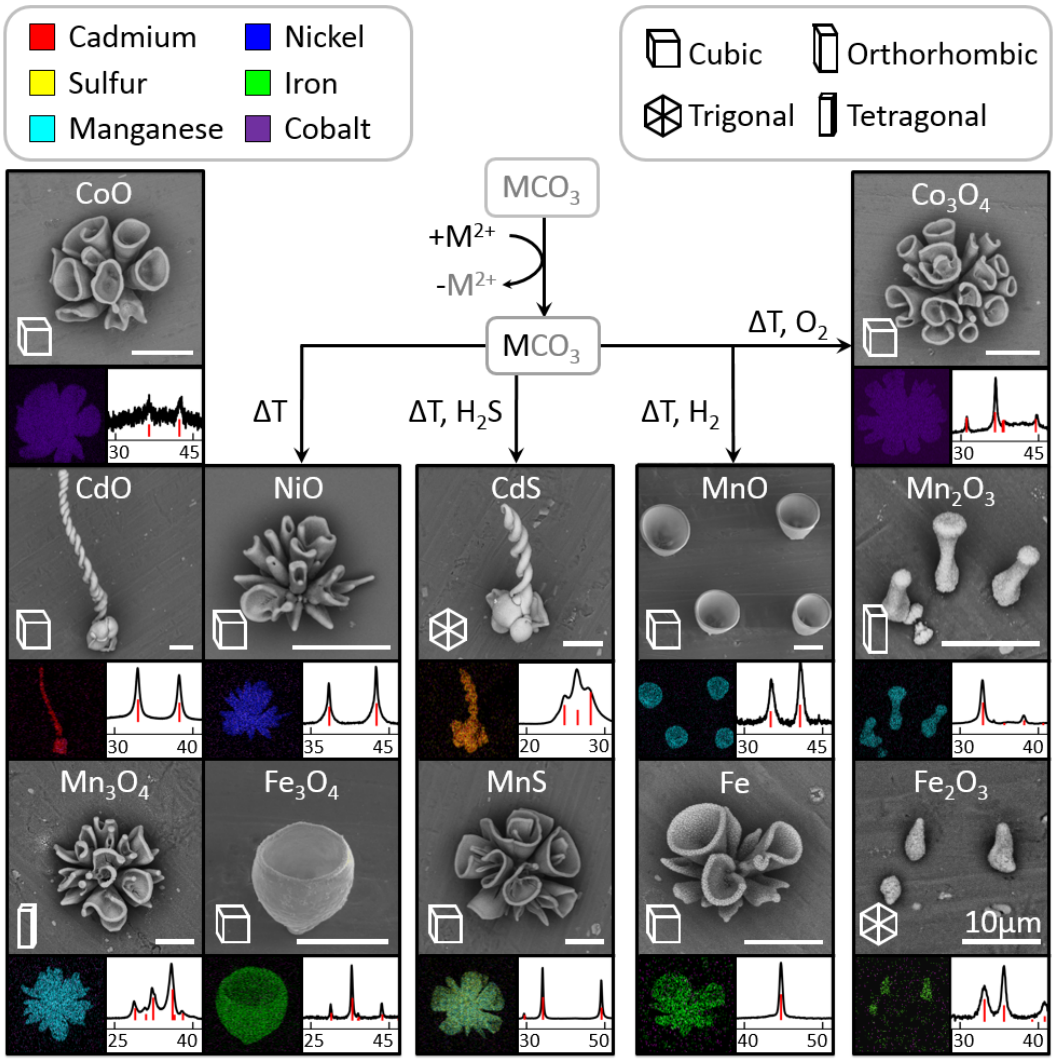


**Figure 2.3: Conversion pathways to metal oxides and metal sulfides.** SEM images show the shape preservation (scalebars 10 µm), while EDS mapping and XRD confirm the conversion (EDS colormap according to top left panel; XRD reference peaks indicated in red, final crystal system indicated by icon). First the desired metal ion is introduced, subsequently the desired metal chalcogenide is obtained by heating the architecture in a chemical vapor deposition oven (See Appendix A.1 for details).

## 2.4 Conclusion

In summary, in this chapter we introduce a versatile strategy for shape-controlled architectures with tunable compositions. The design principles are highly customizable owing to the broad choice of chemistries, and leverage the practical simplicity of directed assembly strategies. We foresee that the multiple complementary functionalities can be integrated by exploiting orthogonal chemistry approaches for tuning the chemical composition of the nanocrystals, and functionalization of the silica matrix with well-developed chemistries. In the following chapters we will explore some of these potential functionalities, looking at the catalytic properties of the converted architectures (chapter 3) and applications in photovoltaics (chapter 4 and 5). Moreover, we will expand the principles described here to biominerals (chapter 4) and new types of conversion routes (chapter 5).

# Bibliography


[1] Eder, M., Amini, S., and Fratzl, P. *Science* **362**(6414), 543–547 (2018).

[2] Weinkamer, R. and Fratzl, P. *MRS Bulletin* **41**(9), 667–671 (2016).

[3] Meldrum, F. C. and Cölfen, H. *Chemical Reviews* **108**(11), 4332–4432 (2008).

[4] Lowenstam, H. A. and Weiner, S. *On Biomineralization*. Oxford Univ. Press, (1989).

[5] Begley, M. R., Gianola, D. S., and Ray, T. R. *Science* **364**(6447) (2019).

[6] Bargardi, F. L., Le Ferrand, H., Libanori, R., and Studart, A. R. *Nature Communications* **7**, 1–8 (2016).

[7] Knoll, P. and Steinbock, O. *Israel Journal of Chemistry* **58**(6), 682–692 (2018).

[8] Garcia-Ruiz, J. M., Melero-Garcia, E., and Hyde, S. T. *Science* **323**(5912), 362–365 (2009).

[9] Noorduin, W. L., Grinthal, A., Mahadevan, L., and Aizenberg, J. *Science* **340**(6134), 832–837 (2013).

[10] Kaplan, C. N., Noorduin, W. L., Li, L., Sadza, R., Folkertsma, L., Aizenberg, J., and Mahadevan, L. *Science* **355**(6332), 1395–1399 (2017).

[11] Whitesides, G. M. and Grzybowski, B. *Science* **295**(5564), 2418–2421 (2002).

[12] Bao, Z., Weatherspoon, M. R., Shian, S., Cai, Y., Graham, P. D., Allan, S. M., Ahmad, G., Dickerson, M. B., Church, B. C., Kang, Z., Abernathy, H. W., Summers, C. J., Liu, M., and Sandhage, K. H. *Nature* **446**(7132), 172–175 (2007).

[13] Studart, A. R. *Advanced Materials* **24**(37), 5024–5044 (2012).

[14] Wegst, U. G., Bai, H., Saiz, E., Tomsia, A. P., and Ritchie, R. O. *Nature Materials* **14**(1), 23–36 (2015).

[15] Mirabello, G., Lenders, J. J., and Sommerdijk, N. A. *Chemical Society Reviews* **45**(18), 5085–5106 (2016).

[16] Vogel, N., Retsch, M., Fustin, C. A., Del Campo, A., and Jonas, U. *Chemical Reviews* **115**(13), 6265–6311 (2015).

[17] Shevchenko, E. V., Talapin, D. V., Kotov, N. A., O'Brien, S., and Murray, C. B. *Nature* **439**(7072), 55–59 (2006).

[18] Kundu, P. K., Samanta, D., Leizrowice, R., Margulis, B., Zhao, H., Börner, M., Udayabhaskararao, T., Manna, D., and Klajn, R. *Nature Chemistry* **7**(8), 646–652 (2015).

[19] Choi, J. H., Wang, H., Oh, S. J., Paik, T., Jo, P. S., Sung, J., Ye, X., Zhao, T., Diroll, B. T., Murray, C. B., and Kagan, C. R. *Science* **352**(6282), 205–208 (2016).

[20] Singh, G., Chan, H., Baskin, A., Gelman, E., Repnin, N., Král, P., and Klajn, R. *Science* **345**(6201), 1149–1153 (2014).

[21] Beberwyck, B. J., Surendranath, Y., and Alivisatos, A. P. *Journal of Physical Chemistry C* **117**(39), 19759–19770 (2013).

[22] Boneschanscher, M. P., Evers, W. H., Geuchies, J. J., Altantzis, T., Goris, B., Rabouw, F. T., Van Rossum, S. A., Van Der Zant, H. S., Siebbeles, L. D., Van Tendeloo, G., Swart, I., Hilhorst, J., Petukhov, A. V., Bals, S., and Vanmaekelbergh, D. *Science* **344**(6190), 1377–1380 (2014).

[23] Putnis, A. *Science* **343**(6178), 1441–1442 (2014).

[24] Powell, A. E., Hodges, J. M., and Schaak, R. E. *Journal of the American Chemical Society* **138**(2), 471–474 (2016).

[25] Stebe, K. J., Lewandowski, E., and Ghosh, M. *Science* **325**(5937), 159–160 (2009).

[26] Holtus, T., Helmbrecht, L., Hendrikse, H. C., Baglai, I., Meuret, S., Adhyaksa, G. W., Garnett, E. C., and Noorduin, W. L. *Nature Chemistry* **10**(7), 740–745 (2018).

[27] Gao, M. R., Xu, Y. F., Jiang, J., and Yu, S. H. *Chemical Society Reviews* **42**(7), 2986–3017 (2013).

[28] Zhang, W., Eperon, G. E., and Snaith, H. J. *Nature Energy* **1**(6) (2016).

[29] Stern, K. H. *High Temperature Properties and Thermal Composition of Inorganic Salts.* CRC Press, (2001).

[30] Legrand, L., Mazerolles, L., and Chaussé, A. *Geochimica et Cosmochimica Acta* **68**(17), 3497–3507 (2004).

[31] Packter, A. and Uppaladinni, S. C. *Kristall und Technik* **10**(9), 985–994 (1975).

[32] Haq, I. U. and Akhtar, K. *Journal of Materials Science* **35**(10), 2565–2571 (2000).

# Chapter 3

## Nanocomposite Architectures as Catalysts

In this chapter we explore the application potential of self-assembled nanocomposites for catalysis. From a pure structural perspective, nanocomposite architectures are metal nanoparticles embedded in an amorphous matrix, and this structural layout is commonly employed in catalytic processes. The performance of catalysts in these processes is dependent on both the size and spacing of their metal nanoparticles. Developing strategies to control these parameters can therefore increase the efficiency of the overall catalytic process. In this chapter, we investigate how the hierarchical growth of the architectures can be employed to build a catalyst with intrinsic spacing and control over the size of the embedded nanoparticles. In particular, we compare this assembly method to traditionally made catalysts by employing them for the dry reforming process. Furthermore, we examine how the grain size of the composites' metal nanoparticles affects their selectivity in the Fischer-Tropsch synthesis. Combined, these results demonstrate that converted nanocomposites can be used as catalysts which have a competitive activity compared to traditional catalyst, as well as tunable selectivity.

Part of this work has been published as:

Hendrikse, H.C., van der Weijden, A., Ronda-Lloret, M., Yang, T., Bliem, R., Raveendran Shiju, N., van Hecke, M., Li, L., and Noorduin, W.L., *Shape-Preserving Chemical Conversion of Architected Nanocomposites*, Advanced Materials, 32(52), 2003999 (2020).

Hans C. Hendrikse and Arno van der Weijden contributed equally.

Part of this work (Fischer-Tropsch synthesis) is submitted for publication.

## 3.1 Introduction

The impact of catalysis on society is almost unmatched by any other process, as it lays at the core of both the chemical and energy industry.[1,2] In particular solid particles catalyzing reactions in liquid or gas have been utilized for a plethora of processes.[3,4] Improving the performance of such heterogeneous catalysts can dramatically increase the efficiency of a catalytic process, as a catalyst often influences reactions many times its own weight.[5]

The performance of a catalyst is characterized by three parameters: activity, selectivity and stability.[6] Activity is defined as the throughput rate of a reaction per amount of catalyst. It is commonly expressed as the turnover frequency (TOF), which describes the amount of starting material converted per catalyst particle per unit of time. Selectivity is defined as the amount of desired product formed compared to the total amount of products formed, including undesired side products. Stability is the ability of a catalyst to maintain its initial activity and selectivity over time. Such stability is not trivial for many catalysts, as their active sites get covered with carbon deposits ('coking') or their catalytic particles agglomerate.[7,8]

The performance of a catalyst is dependent on its physical properties, which in turn are determined by the preparation method. For example, the active sites, where the actual catalysis takes place, are usually metallic nanocrystals. The size of these metal particles is generally kept small, usually below 30 nm, with an optimal size depending on the specific process.[9,10]By decreasing the particle size, the surface-to-volume ratio of the particle increases, resulting in a more active catalyst.[11] Furthermore, these particles are usually supported by, or embedded on, an inert support to prevent them from agglomerating.[12,13] This support is typically porous to increase the surface area, thus allowing for more catalytic particles to be embedded on the support, which in turn results in a more active catalyst per unit volume. Another way to improve the activity per unit volume is by increasing the amount of metal particles on the support material. However, a higher metal loading may lead to agglomeration and larger particles, thereby lowering selectivity and reducing the TOF.[3,14] The performance of a catalyst is thus dependent on the interplay between the support used, the metal loading, and the particle size of the metal particles.

Traditionally, heterogeneous catalysts are prepared by loading metal particles (Fe, Ni and Co among others)[15–17]on a support material (for example $SiO_2$, $Al_2O_3$ or $TiO_2$).[18–20] This is typically done by either precipitation or impregnation. With precipitation, a precursor is precipitated on a substrate by causing an oversaturation by for example a change in pH, via coprecipitation, or by a change in temperature.[21] With impregnation, the metal ions are brought onto the support by infiltrating its pores and using adsorption to fixate the metal particles on the support material.[21,22] Both options enable the formation of a large variety of catalysts, though there are limitations to the explorable parameter space. For example, in both instances the metal loading is performed on an already existing support, which makes the resulting catalyst dependent on the diffusion of the metal particles onto the support. This in turn makes parameters like particle size and spacing always dependant on this diffusion, adding an additional dependency to these already difficult to tune parameters.

Alternatively, the catalyst could also be coprecipitated with the support, thus forming both at the same time. However, simultaneous precipitation of the metallic particles and support materials is not trivial as undesired phase separation, full catalyst encapsulation, or unintended reactions between the support and catalyst can occur.[23–26]

From this perspective, nanocomposite architectures of $BaCO_3$ and $SiO_2$ may provide an attractive alternative route towards designable heterogenous catalysts. First, the hierarchical coprecipitation can shape the support ($SiO_2$) and instantaneously embed the metal particles ($BaCO_3$) inside. Then, ion exchange can convert the barium ions to catalytically active metals. This route provides unique possibilities to design the catalyst: The hierarchical growth of the architectures allows for automatic spacing of the metal particles inside their support (see Figure 3.1). Furthermore, the encapsulation of the metal particles in the $SiO_2$ matrix limits their size to 20 nm or less (see Table A.1 and A.2), even though the metal loading is exceptionally high (75-80 at.%, see Chapter 2). Finally, the hierarchical growth of the support and metal particles allows for customization of the microshape, thus giving it a tunable surface area. This allows for an intrinsic high surface area (e.g. with coral-like shapes), without the necessity of creating porosity in the support. In summary, the properties that self-assemble the architectures may thus also translate to ways of designing and tuning a catalyst.

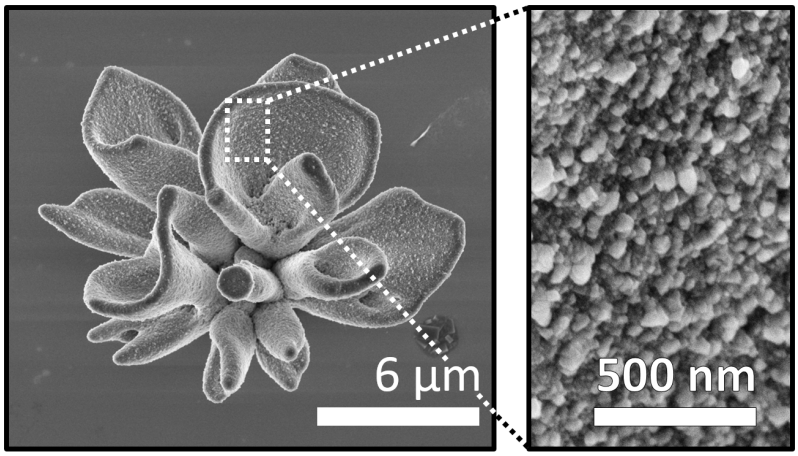


**Figure 3.1: Coral-shaped, NiO-containing nanocomposite with zoom in on the nanostructure.** The coral-like microshape offers a high surface area for the nanocrystals, while the hierarchical structuring originally formed by the coprecipitation between $BaCO_3$ and $SiO_2$ creates an intrinsic spacing between the NiO nanocrystals.

In this chapter we explore the catalytic performance of the nanocomposite architectures. In particular, we use the architectures to catalyze two complimentary processes: the dry reforming process and the Fischer-Tropsch synthesis. [17]

The dry reforming process converts carbon dioxide ($CO_2$) along with small hydrocarbons like methane ($CH_4$) or butane ($C_4H_{10}$) to a mixture of hydrogen ($H_2$) and carbon monoxide (CO), commonly known as syngas (reaction 3.1). [27] The stability of $CO_2$ causes this process to require temperatures of 600-800 °C, which are unfavourable due to the high deactivation rates and high costs to operate at these temperatures. [28] Hence, there is a current search for catalysts which are active at 400 °C. In this chapter we explore the possibility of using nanocomposite architectures to develop such a catalyst.

The Fischer-Tropsch synthesis converts syngas to longer hydrocarbons ($C_xH_{2+2x}$, reaction 3.2). [29] The ideal carbon chain length of these hydrocarbons varies based on their intended application. [30–32] Therefore the focus here will be on obtaining selectivity in the carbon chain length of the obtained product, which can be tuned by the grain size of the metal particles catalyzing the Fischer-Tropsch synthesis. [33] We will tune the architectures' metal particles by adapting the synthesis procedure and explore how this affects their selectivity in the Fischer-Tropsch synthesis. In summary, this chapter aims to explore the activity of the nanocomposite architectures with the dry reforming process, and their selectivity with the Fischer-Tropsch synthesis.

$$CH_4 + CO_2 \rightarrow 2H_2 + 2CO \qquad \Delta H^\circ_{298K} = 247 kJ/mol \tag{3.1}$$

$$(2x+1)H_2 + xCO \rightarrow C_xH_{2x+2} + xH_2O \tag{3.2}$$

## 3.2 Dry Reforming of Butane

Converting $CO_2$ to value adding products could potentially be the most important conversion of our generation. Not only is this conversion a vital part of a circular economy, it also reduces the concentration of green house gases in our atmosphere.[34] The dry reforming process is a promising technique to realize this, converting carbondioxide ($CO_2$) and small hydrocarbons (from methane ($CH_4$) up to butane ($C_4H_{10}$)) into the increasingly valuable syngas (hydrogen ($H_2$) and carbonmonoxide (CO)).[17] Unfortunately, the high stability of $CO_2$ forces this conversion to take place at high temperatures between 600 and 800 °C, making it difficult to apply in a commercial setting. Hence, there is a need for catalysts which can operate at temperatures of 400 °C or lower.[28]

Unfortunately, currently available catalysts demonstrate low activity at these temperatures, and thus new catalysts with high activity at low temperature need to be developed for dry reforming.[28] Nanocomposite architectures are potential candidates for this, as their high metal loading could offer higher activity at these lower temperatures.[35] Normally an increase in the metal loading would also increase the particle size of the metal particles, which in turn results in unwanted side reactions.[36] However, the hierarchical growth of the architecture prevents this, as the inhibiting effect of the $SiO_2$ precipitation limits the particle size of the nanocrystal (Table A.1). This makes the architectures potential catalysts with high metal loading, which also have a small grain size per individual metal particle.

### 3.2.1 Results and Discussion

We here demonstrate the potential of coral-like architectures, in particular those converted to NiO, for the dry reforming of butane (DRB, reaction 3.3). To produce enough architectures for DRB, a new procedure was developed to produce these architectures at the gram scale (Figure 3.2). In this procedure, the autonomous nature of bottom-up assembly is leveraged by growing the architectures on the meniscus rather than on a substrate. As the growth of the architectures is only dependent on the local chemistry (see Section 1.3), the assembly of an individual architecture is similar in both instances. However, because of the much higher surface area of the used tray compared to a substrate, it is possible to scale the production of the architectures by over 500-fold to $\sim 500$ mg per tray.

$$C_4H_{10} + 4CO_2 \rightarrow 5H_2 + 8CO \qquad \Delta H^\circ{}_{298K} = 428 kJ/mol \tag{3.3}$$

**Figure 3.2: Scalability of DRB.** Photo depicting yield difference between growth on the meniscus (tray) and on a substrate (aluminum slide, bottom left). Depicted ruler (bottom right) is 20 cm for reference.

To benchmark the catalytic activity of the NiO architectures ($Ni_{coral}$), their performance for DRB was compared to conventional catalysts prepared via wet impregnation (see Appendix A.4.2). These reference catalysts were prepared with two different metal loadings, one with a conventionally used metal loading (5wt%, $Ni_{convent}$), and one with a equivalent metal loading to the architectures (80 wt% $Ni_{equiv}$). The catalytic tests were carried out under atmospheric pressure in an automated six-flow parallel reactor system, flowing 10 mL/min of a gas mixture of 80% Ar, 16% $CO_2$ and 4% $C_4H_{10}$. As expected, $Ni_{convent}$ does not show any detectable conversion at 400 °C (Figure 3.3). However, both the $Ni_{coral}$ and $Ni_{equiv}$ do show activity, indicating that a higher metal loading indeed stimulates activity at this lower temperature.

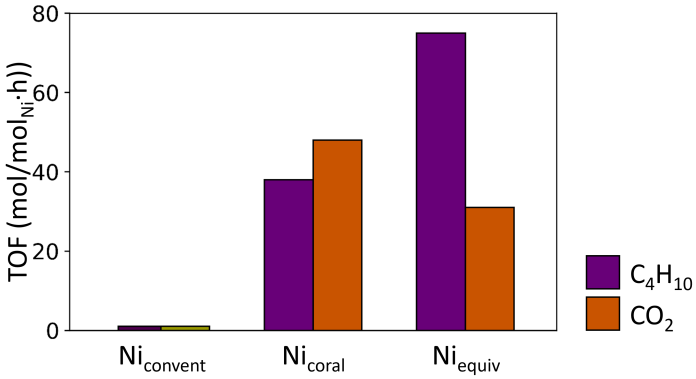


**Figure 3.3: Activity of DRB for nanocomposite architectures and references.** Reaction is performed at 400 °C, where $Ni_{convent}$ shows no detectable activity. $Ni_{coral}$ and $Ni_{equiv}$ on the other hand show comparable activity, with the former converting more $CO_2$ and the latter more $C_4H_{10}$.

The difference between $Ni_{coral}$ and $Ni_{equiv}$ lies within the products they produce. Here, CO makes up 48.9% of the formed products when using $Ni_{coral}$, compared to only 17.4% when using $Ni_{equiv}$ as a catalyst instead (Figure 3.4). Moreover, even though the $Ni_{equiv}$ produces almost similar amounts of $H_2$ compared to $Ni_{coral}$ (38.1% against 43.8%), the major product of the $Ni_{equiv}$ are side products like $CH_4$ and $C_2$-species, as well as the formation of coke (44.5% of total, see Appendix A.4.2 for details). These side products presumably form from unwanted side reactions, like the Boudoard reaction, the cracking of butane or dehydrogenation reactions.[37–39] In the case of $Ni_{coral}$, side products also form, but this is only 7.3% of the total formed products, significantly less than $Ni_{equiv}$. Comparing the peak broadening in the XRD patterns of $Ni_{coral}$ and $Ni_{equiv}$ reveals a grain size of 19 nm and 105 nm respectively, which suggests that the higher selectivity of $Ni_{coral}$ is caused by its smaller grain size.

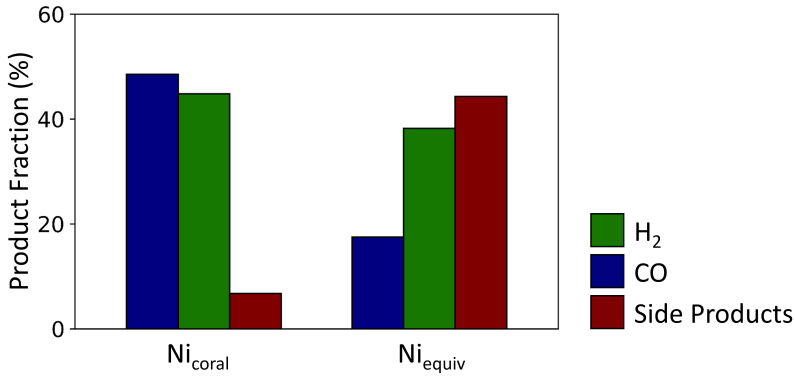


**Figure 3.4: Selectivity of DRB.** $Ni_{coral}$ forms predominately the desired product, forming 48.9% CO, 43.8% $H_2$ and 7.3% side products (composed of $CH_4$, $C_2$-species and formed coke). $Ni_{equiv}$ on the other hand forms predominantly side products, with 17.4% CO, 38.1% $H_2$ and 44.5% side products.

The stability of $Ni_{coral}$ also exceeds that of $Ni_{equiv}$ as it stays operational longer, but only by half an hour (Figure 3.5). An explanation for this can be found in the carbon balance of $Ni_{coral}$. Though the amount of side product formed with $Ni_{coral}$ is relatively low, it is almost exclusively coke (see Appendix A.4.2 for details). This significantly affects the stability of the conversion, as the coke clogs the pores of the catalyst. This in turn stops the gasflow, making it impossible to measure the products of the reaction and forcing the reactor to be shut down. Although $Ni_{coral}$ has a good initial catalytic activity, it is crucial to improve its coking resistance to increase its long term stability. It is therefore vital to improve the coke resistance of the catalyst to make the $Ni_{coral}$ more appealing as a catalyst. According to literature, coke formation is however common for a system with NiO particles embedded on a silica support.[40] Possible ways to overcome this challenge have been found by applying alkali metals like potassium to increase the basicity of the catalyst and prevent coke formation catalyzed by acidic sides.[27] Alternatively, introducing a promoter like cerium or zirconium can also prevent coke formation, as shown by Debek *et al.*[41,42]

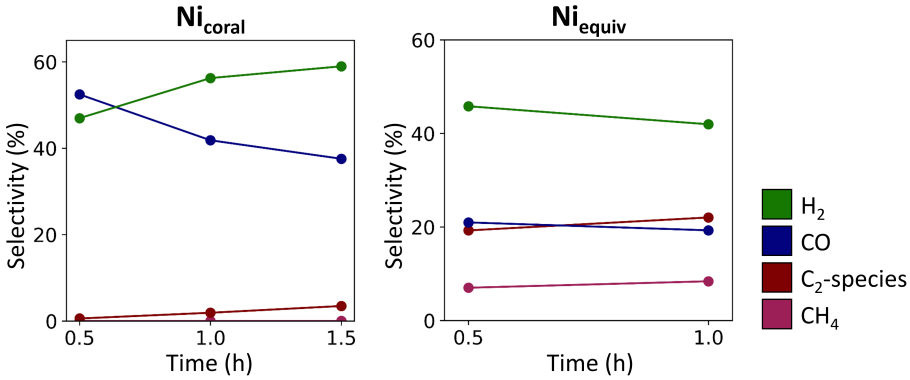


**Figure 3.5: Stability of DRB.** Though the reactor remains operational longer in the case of $Ni_{coral}$(left) compared to $Ni_{equiv}$(right), further optimization is needed to keep the reactor operational at longer time scales.

Collectively, these results demonstrate a unique strength of our approach: the hierarchical growth of nanocrystals and $SiO_2$ support enables high metal loadings which yield high catalytic activity and nanosized metal particles for improved selectivity. Though quite promising as initial results, further optimization is needed to increase the appeal of nanocomposite architectures as catalysts. In particular, the stability of these architectures is still low, as they only last 1,5 hour under operating conditions. This can be improved in future research by introducing a promotor or by further developing the control over the metal particle grain size.

## 3.3 Fischer-Tropsch Synthesis

The Fischer-Tropsch synthesis (FTS) plays an important role in the realisation of a circular economy, as it produces hydrocarbons from syngas, which are used as starting materials for fuel, plastics and specialty chemicals.[30–32] The hydrocarbons produced in FTS have a variable carbon chain length ($C_xH_{x+2}$), which optimum length depends on their application. Therefore, catalysts which can tune the carbon chain length in this synthesis are of great interest. One way to introduce this tunability is to control the particle size of the catalyst's metallic crystals.[33]

Here nanocomposite architectures are potential candidates as catalysts with tunable selectivity. Their hierarchical growth, as well as the conditions chosen during the ion exchange, gives the architectures a variable crystal size (Table A.1). Thus, we hypothesize that the formation of the architectures not only gives us control over the crystal size and spacing, but also allows for variation of the crystal size. This in turn potentially allows for tuning of the resulting hydrocarbon's chain length when these architectures are applied for FTS.

We test this hypothesis by applying $Co_3O_4/SiO_2$ nanocomposites containing crystals with various grain sizes for FTS. We tune the crystal size within the $Co_3O_4/SiO_2$ nanocomposites by inducing sintering of the crystals during the decomposition step of our conversion reaction. To this aim, we perform decompositions at different temperatures and determine the crystal size from X-ray powder diffractograms using the Scherrer equation (see Appendix A.2.6). Consistent with previously observed sintering,[43,44] we observe an almost linear increase in crystal sizes from ca. 10 nm ($Co_3O_4$(10nm)/$SiO_2$) to ca. 17 nm ($Co_3O_4$(17nm)/$SiO_2$) for temperatures ranging from 530 °C to 650 °C (Figure 3.6). Moreover, even though the nanoscopic crystal size can be tailored precisely over a wide range of sizes, the nanocomposite layout remains preserved (see Appendix A.1.6).

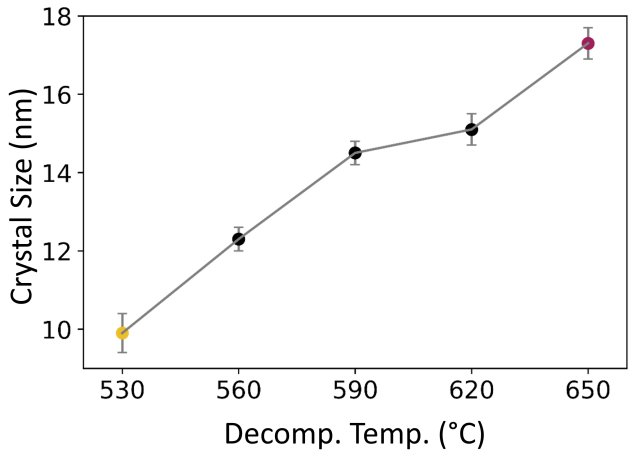


**Figure 3.6: Relation of decomposition temperature and the resulting $Co_3O_4/SiO_2$ nanocomposite's crystal grain size.** The crystal size was estimated from the peak $\sim 37°$ of the XRD pattern of $CO_3O_4/SiO_2$ nanocomposites (Appendix A.1.6). Increasing the decomposition temperature causes sintering, which in turn yields larger crystal sizes (see Appendix A.2.6 for details).

We perform the FTS with $Co_3O_4$(17nm)/$SiO_2$ nanocomposites. The nano-composites are placed in a gas flow reactor and are reduced to the active metal cobalt catalyst with $H_2$ (10 vol.% in $N_2$ flow rate of 50 mL/min). FTS is initiated by flowing $H_2$, CO and $N_2$ (with a ratio of 6:3:1) into the reactor at 20 bar, 220 ˚C, and a gas hourly space velocity (GHSV) of 320 mL/gcat/min. The reaction progress is followed using real-time online gas chromatography. We observe an initial conversion of 13% and a steady-state conversion rate of 5% with a turnover frequency (TOF) of $6.2{\cdot}10^{-3}$ $s^{-1}$(see Appendix A.4.3 for details), a performance which is comparable with traditionally-prepared state-of-the-art catalysts.[10,45,46] Remarkably, the reaction predominantly produces long carbon chains with 40% of the products having a chain length of $C_{20}$+, which is a desired attribute in FTS catalysts, commonly associated with large and uniformly distributed nanocrystals.[32,46] Hence, these findings demonstrate the functionality potential of these self-assembled nanocomposites for selectively catalyzing FTS.

According to the current understanding on FTS cobalt catalysts, smaller nanocrystals catalyze the formation of shorter hydrocarbon chains with respect to larger crystals, while the effects of crystal size on reaction rate (TOF) depend on the size range.[30,31,46] Most studies agree that TOF increases with the crystal size up to ca. 6 – 10 nm and remains nearly invariant with larger crystals, while others report a negative effect of TOF for even larger crystals of ca. 10-15 nm.[46] Thus, to further assess the potential of the self-assembled nanocomposites, we aim to tune the catalytic selectivity and activity of the FTS reaction by tailoring the nanocrystal size within the nanocomposite. To this aim, we decrease the crystal size of the $Co_3O_4/SiO_2$ nanocomposites from 17 to 10 nm by performing the decomposition at 530 ˚C (Appendix A.1.6), and perform the FTS under identical conditions. Consistent with previous reports,[46] the decrease in crystal size results in an increase of the initial conversion from 13% to 25%, a steady-state conversion rate from 5% to 15%, and a TOF increase from $6.2{\cdot}10^{-3}$ $s^{-1}$ to $11{\cdot}10^{-3}$ $s^{-1}$. Furthermore, as expected, the decrease of the nanocrystal size shifts the selectivity of these catalysts to form predominately medium-long carbon chains, with 27% of the products as $C_{5\text{-}10}$ , while only 17% of the products has a chain length of $C_{20}$+ (Figure 3C). Thus, our self-assembly scheme enables customization of the crystal size within the nanocomposites for straightforwardly tuning of the selectivity and activity of the FTS.

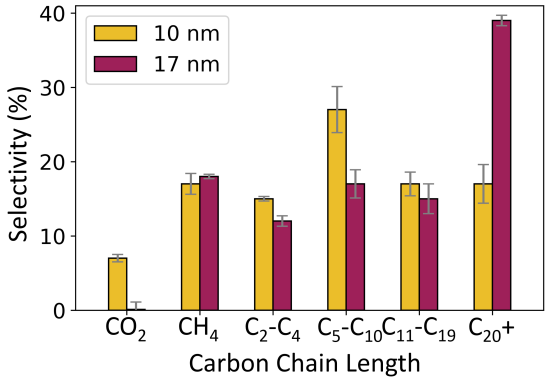


**Figure 3.7: Results of the Fischer Tropsch synthesis with 17 nm and 10 nm particles.** The 17 nm particles predominately grow carbon chains of 20+ (purple). Their initial activity is 15%, which lowers to a steady state of 5.3% over 20 hours. The 10 nm particles show a preference to grow carbon chains between $C_5$-$C_{10}$ (yellow). Their initial activity is 25%, which lowers to a steady state of 13.3% over 25 hours.

These results show the potential these architectures have: Not only do they autonomously form a suitable structure for catalysis, but they also allow for tuning of selectivity in FTS by subtly changing the decomposition temperatures. We believe that the architectures could be valuable as catalysts, especially as many optimizations like use of promotors and use of metal mixtures remains unexplored.[47–49]

## 3.4 Conclusion

In this chapter we explored the application potential of nanocomposite architectures in catalysis. For this, we employed Ni- and Co-containing nanocomposites for the dry reforming of butane and the Fischer Tropsch synthesis, respectively.

With the dry reforming reaction, we compared the Ni-containing nanocomposite catalysts with traditionally prepared catalysts. We find that the nanocomposite catalysts show activity at 400 °C. This is several hundreds of degrees lower than temperatures where catalysts with traditional metal loadings are active. These traditionally prepared catalysts can also be active at 400 °C with an increased metal loading, but they lose selectivity due to the large crystal sizes of the metal particles. The hierarchical growth of the nanocomposite catalysts keeps its metal particles small, giving them good selectivity without compromising their activity at these lower temperatures.

With the Fischer Tropsch synthesis, we investigated the control over the carbon chain length selectivity with the Co-containing nanocomposite catalysts. For this, we varied the temperature during the decomposition of $CoCO_3/SiO_2$ nanocomposites, resulting in $Co_3O_4/SiO_2$ nanocomposites with a tunable crystal size. This in turn allows for a tunable carbon chain length in the formed products, where a larger crystal size results in longer hydrocarbons. Thus, simple modification in the conversion scheme of the nanocomposite allows for tunability in the selectivity of the Fischer Tropsch synthesis.

Collectively, nanocomposite architectures offer exciting opportunitites for catalytic processes, either by lowering their reaction temperature or by controlling their selectivity. Moreover, this procedure can easily be scaled, as the formation of the architectures is autonomous and occurs as long as the right reaction conditions are set.

# Bibliography


[1] Hutchings, G. J., Catlow, C. R. A., Hardacre, C., and Davidson, M. G. *Philosophical Transactions of the Royal Society A: Mathematical, Physical and Engineering Sciences* **374**(2061) (2016).

[2] Armor, J. N. *Catalysis Today* **163**(1), 3–9 (2011).

[3] Munnik, P., De Jongh, P. E., and De Jong, K. P. *Chemical Reviews* **115**(14), 6687–6718 (2015).

[4] Campanati, M., Fornasari, G., and Vaccari, A. *Catalysis Today* **77**(4), 299–314 (2003).

[5] Behrens, M., Studt, F., Kasatkin, I., Kuhl, S., Havecker, M., Abild-Pedersen, F., Zander, S., Girgsdies, F., Kurr, P., Kniep, B.-L., Tovar, M., Fischer, R. W., Norskov, J. K., and Schlogl, R. *Science* **336**(6083), 893–897 may (2012).

[6] Schwarz, J. A., Contescu, C., and Contescu, A. *Chemical Reviews* **95**(3), 477–510 (1995).

[7] Calvin H. *Applied Catalysis A: General* **212**(1-2), 17–60 (2001).

[8] Munnik, P., De Jongh, P. E., and De Jong, K. P. *Journal of the American Chemical Society* **136**(20), 7333–7340 (2014).

[9] Murdoch, M., Waterhouse, G. I., Nadeem, M. A., Metson, J. B., Keane, M. A., Howe, R. F., Llorca, J., and Idriss, H. *Nature Chemistry* **3**(6), 489–492 (2011).

[10] Bezemer, G. L., Bitter, J. H., Kuipers, H. P., Oosterbeek, H., Holewijn, J. E., Xu, X., Kapteijn, F., Van Diilen, A. J., and De Jong, K. P. *Journal of the American Chemical Society* **128**(12), 3956–3964 (2006).

[11] van Santen, R. A. *Accounts of Chemical Research* **42**(1), 57–66 (2009).

[12] Parlett, C. M., Wilson, K., and Lee, A. F. *Chemical Society Reviews* **42**(9), 3876–3893 (2013).

[13] Sudarsanam, P., Peeters, E., Makshina, E. V., Parvulescu, V. I., and Sels, B. F. *Chemical Society Reviews* **48**(8), 2366–2421 (2019).

[14] Prieto, G., Zečević, J., Friedrich, H., De Jong, K. P., and De Jongh, P. E. *Nature Materials* **12**(1), 34–39 (2013).

[15] Khodakov, A. Y., Chu, W., and Fongarland, P. *Chemical Reviews* **107**(5), 1692–1744 (2007).

[16] Sivula, K., Le Formal, F., and Grätzel, M. *ChemSusChem* **4**(4), 432–449 (2011).

[17] Fan, M. S., Abdullah, A. Z., and Bhatia, S. *ChemCatChem* **1**(2), 192–208 (2009).

[18] Yu, J., Yu, J., Shi, Z., Guo, Q., Xiao, X., Mao, H., and Mao, D. *Catalysis Science and Technology* **9**(14), 3675–3685 (2019).

[19] Trueba, M. and Trasatti, S. P. *European Journal of Inorganic Chemistry* (17), 3393–3403 (2005).

[20] Lomate, S., Sultana, A., and Fujitani, T. *Catalysis Science and Technology* **7**(14), 3073–3083 (2017).

[21] Deraz, N. M. *Journal of Industrial and Environmental Chemistry* **2**(1), 19–21 (2018).

[22] Van Dillen, A. J., Terörde, R. J., Lensveld, D. J., Geus, J. W., and De Jong, K. P. *Journal of Catalysis* **216**(1-2), 257–264 (2003).

[23] Vesselli, E. and Peressi, M. *Nanoscale Control of Metal Clusters on Templating Supports*, volume 177. Elsevier B.V., 1 edition, (2017).

[24] Heiz, U. and Bullock, E. L. *Journal of Materials Chemistry* , 564–577 (2004).

[25] Fang, W., Hu, H., Ma, Z., Wang, L., and Zhang, Y. *Catalysts* **8**(9) (2018).

[26] Guerrero-Martínez, A., Pérez-Juste, J., and Liz-Marzán, L. M. *Advanced Materials* **22**(11), 1182–1195 (2010).

[27] Zhang, G., Liu, J., Xu, Y., and Sun, Y. *International Journal of Hydrogen Energy* **43**(32), 15030–15054 (2018).

[28] Wang, Y., Yao, L., Wang, S., Mao, D., and Hu, C. *Fuel Processing Technology* **169**(October 2017), 199–206 (2018).

[29] Dry, M. E. *Catalysis Today* **71**(3-4), 227–241 (2002).

[30] Torres Galvis, H. M. and De Jong, K. P. *ACS Catalysis* **3**(9), 2130–2149 (2013).

[31] Dry, M. E. *Journal of Chemical Technology and Biotechnology* **77**(1), 43–50 (2002).

[32] Bouchy, C., Hastoy, G., Guillon, E., and Martens, J. A. *Oil and Gas Science and Technology* **64**(1), 91–112 (2009).

[33] Khodakov, A. Y. *Catalysis Today* **144**(3-4), 251–257 (2009).

[34] Artz, J., Müller, T. E., Thenert, K., Kleinekorte, J., Meys, R., Sternberg, A., Bardow, A., and Leitner, W. *Chemical Reviews* **118**(2), 434–504 (2018).

[35] Dong, W. S., Roh, H. S., Jun, K. W., Park, S. E., and Oh, Y. S. *Applied Catalysis A: General* **226**(1-2), 63–72 (2002).

[36] Zhang, J., Wang, H., and Dalai, A. K. *Applied Catalysis A: General* **339**(2), 121–129 (2008).

[37] Basu, P. *Gasification Theory and Modeling of Gasifiers*. Elsevier Inc., first edition edition, (2010).

[38] Froment, G. F., Van De Steene, B. O., Vanden Berghe, P. J., and Goossens, A. G. *AIChE Journal* **23**(1), 93–106 (1977).

[39] Wu, J., Peng, Z., Sun, P., and Bell, A. T. *Applied Catalysis A: General* **470**, 208–214 (2014).

[40] Martin, C. C., Coleman, D. N., Garcia, L. G., Furnus, C. C., and Relling, A. E. *Journal of Animal Science* **96**(12), 5300–5310 (2018).

[41] Dębek, R., Motak, M., Galvez, M. E., Grzybek, T., and Da Costa, P. *International Journal of Hydrogen Energy* **42**(37), 23556–23567 (2017).

[42] Dębek, R., Motak, M., Galvez, M. E., Da Costa, P., and Grzybek, T. *Reaction Kinetics, Mechanisms and Catalysis* **121**(1), 185–208 (2017).

[43] Gadow, R. and Kern, F. *Journal of the Ceramic Society of Japan* **114**(1335), 958–962 (2006).

[44] Shirsath, S. E., Kadam, R. H., Gaikwad, A. S., Ghasemi, A., and Morisako, A. *Journal of Magnetism and Magnetic Materials* **323**(23), 3104–3108 (2011).

[45] Iglesia, E. *Applied Catalysis A: General* **161**(1-2), 59–78 (1997).

[46] Borg, Ø., Dietzel, P. D., Spjelkavik, A. I., Tveten, E. Z., Walmsley, J. C., Diplas, S., Eri, S., Holmen, A., and Rytter, E. *Journal of Catalysis* **259**(2), 161–164 (2008).

[47] Tihay, F., Roger, A. C., Kiennemann, A., and Pourroy, G. *Catalysis Today* **58**(4), 263–269 (2000).

[48] Jacobs, G., Das, T. K., Zhang, Y., Li, J., Racoillet, G., and Davis, B. H. *Applied Catalysis A: General* **233**(1-2), 263–281 (2002).

[49] Yang, Y., Xiang, H. W., Xu, Y. Y., Bai, L., and Li, Y. W. *Applied Catalysis A: General* **266**(2), 181–194 (2004).

# Chapter 4

## Nanocomposite Architectures as Luminescent Perovskites

In this chapter we present a strategy to convert a wide range of metal carbonate nanocomposite architectures into lead halide perovskite semiconductors with tunable bandgaps, while preserving the 3D shape. First, we introduce lead ions by cation exchange. Second, we use carbonate as a leaving group, facilitating anion exchange with halide, which is followed rapidly by methylammonium insertion to form the perovskite. As proof of principle, pre-programmed carbonate salt shapes such as vases, coral-like forms and helices are transformed into perovskites while preserving the morphology and crystallinity of the initial nanocomposite architectures. This approach also readily converts calcium carbonate biominerals into semiconductors, furnishing biological and programmable synthetic shapes with the performance of artificial compositions such as perovskite-based semiconductors.

This work has been published as:

Holtus, T., Helmbrecht, L., Hendrikse, H.C., Baglai, I., Meuret, S., Adhyaksa, G.W., Garnett, E.C. and Noorduin, W.L., *Shape-preserving transformation of carbonate minerals into lead halide perovskite semiconductors based on ion exchange/insertion reactions*, Nature chemistry, 10(7), 740-745 (2018).

Tim Holtus, Lukas Helmbrecht, and Hans C. Hendrikse contributed equally.

## 4.1 Introduction

Lead halide perovskites have drawn attention from the scientific community because of their excellent optoelectronic performance.[1–3] Furthermore, strategies that offer independent control over 3D shape and composition of nano- and micro-scale architectures are of fundamental interest and hold relevance for optoelectronics and many other fields.[4–12] In this chapter we present a strategy to convert a wide range of carbonate architectures into lead-halide perovskite semiconductors with tunable bandgaps, giving the carbonate's programmable 3D shape to perovskites.

Carbonate salts, including the most abundant biomineral calcium carbonate, give access to an impressive catalogue of exquisitely sculpted crystalline shapes that can be created via biological and bio-inspired mineralization processes with a rational control over form.[4,5,12–17] However, these carbonate salts have limited application potential, due to the properties of their chemical composition.

One way to overcome this inherent limitation is by converting previously formed shapes into a desired composition while preserving the original shape. So far, these shapes have already been converted into functional compositions using oxidation/reduction reactions, which give access to a range of metals and metal oxides (Chapter 2).[11,18–20] However, many compositions that can act as conductors, semi-conductors and catalysts contain non-transition metals and halides (e.g. lead halide perovskites), which are inaccessable with the reaction pathways discussed so far.

The approach to tune the material composition by ion-exchange reactions can however be expanded to include these new materials. Ion-exchange reactions enable the conversion of the ionic composition of nanocrystals—and superlattices thereof—into a wide range of compositions, whilst preserving the original morphology.[21–31] Cation exchange has already been demonstrated for many different ions.[23] Anion exchange, on the contrary, remains challenging as the larger size and lower diffusivity of anions hinder proper conversions. As a result, only a few examples of successful anion exchange reactions have been reported and general routes to exchange anions still need to be developed.[26,27]

Here we demonstrate a new pathway towards lead halide perovskites with complete cationic and anionic exchange and full shape preservation, starting from a variety of biological and bio-inspired artificial materials. Two key insights underlie this approach. First, the anionic carbonate group in biological and bio-inspired minerals can act as a remarkably good leaving group, offering a promising way to introduce new anions in a relatively facile and generic manner. Second, many biomineralized architectures are composed of nanocomposites, i.e., materials composed of an ensemble of nanocrystals embedded in an amorphous matrix, and this nanocrystalline nature may readily enable the tuning of their composition using ion-exchange reactions. This applies not only to biologically formed materials, but also to the rich variety of synthetic bioinspired materials, for which numerous strategies exist to yield rationally designed shape-controlled hybrid materials.[5–8,12–17] Exploiting these two unique advantages will thus enable the possibility to first program the shape in a carbonate salt nanocomposite and subsequently apply a cascade of cation and anion conversion reactions to obtain a functional-material composition, e.g. a semiconductor or catalyst, of the exact same shape.

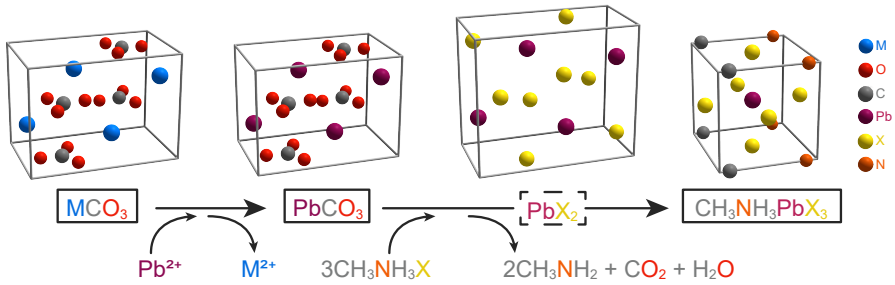


**Figure 4.1: Reaction scheme for the synthesis of $CH_3NH_3PbX_3$ perovskites from carbonate salts ($MCO_3$).** The reaction of $PbCO_3$ with $CH_3NH_3X$ results in the direct formation of $CH_3NH_3PbX_3$ via intermediate $PbX_2$ (dashed box). Cation organization in the crystal unit cell of the carbonate salts and $PbX_2$ is similar, thereby facilitating the cation exchange reaction. The sizes of the unit cells are scaled for the conversion of $BaCO_3$ to $CH_3NH_3PbBr_3$. M(blue)=Ca, Ba or Sr; X(yellow)=Cl, Br or I; Pb (purple), O (red), N (orange), C and H (both grey).

To demonstrate the proof-of-principle, we chose methylammonium lead-halide perovskites ($CH_3NH_3PbX_3$) as target materials. The exceptional performance of these semiconductors for solar cells, water-splitting, lasers, LEDs and radiation detectors along with their facile synthesis is revolutionizing the prospects of next-generation optoelectronics.[32] So far most studies have been performed on thin films, but control over the 3D microscale morphology of perovskites may be essential for developing the next generation of transistors and directed light-absorption and emission.[33] Despite the recent progress in casting methods,[34,35] growth of arbitrary perovskite shapes has remained challenging, and highlights the need for new strategies to gain independent control over shape and composition.

In this chapter we show a simple two-step reaction scheme for converting carbonate architectures into lead-halide perovskites (Figure 4.1). Starting from biological and programmable synthetic carbonate-salt architectures we convert these into perovskites with a tunable bandgap and a charge carrier lifetime on par with state-of-the-art perovskite thin films, while at the same time inheriting the 3D shape, fine features, and crystallinity of the starting architecture.

## 4.2 Conversion to Lead Halide Perovskite

Conversion of carbonate salts into perovskites requires a complete chemical and structural transformation involving the exchange of the cations and the notoriously difficult exchange of anions, insertion of methylammonium halide ($CH_3NH_3X$), and rearrangement of the crystal unit cell, while in all steps minimizing the distortion of the crystal lattices (Figure 4.1). A key insight for the development of our route is that $PbX_2$, a commonly used precursor for synthesizing lead halide perovskites,[36,37] crystallizes in the same orthorhombic crystal structure as $PbCO_3$ (cerrusite) and many other carbonate salts $MCO_3$ (with M = i.e. Ba, Sr, or Ca in the witherite, strontianite, and aragonite crystal structures, respectively). More explicitly, the metal ions in the crystal structures of $PbX_2$, $PbCO_3$ and $MCO_3$ are in the same position, and the dimensions

of the unit cells are closely matched, with the length of the unit cell axes changing typically less than 10%. Additionally, the carbonate group can act as a good leaving group for facilitating the insertion of the halides into the $PbCO_3$ structure. Our two-step reaction scheme thus allows us to synthesize lead-halide perovskites from arbitrarily chosen metal carbonate architectures by first exchanging the metal ions for lead, followed by the reaction of the carbonate ions with methylammonium halides to directly yield the corresponding perovskite.

Prior to performing the conversion reaction, we program the carbonate nanocomposite into the desired target architecture. For the proof-of-principle, we use the bio-inspired coprecipitation of barium and strontium carbonate nanocrystals with silica. This nanocomposite system offers a pragmatic platform for developing a wide selection of micro-sized 3D geometries including vase, spiral, and coral shapes, which can be formed by rationally modulating the reaction conditions such as temperature, pH and $CO_2$ concentration.[12,16,17] We illustrate the concept of the conversion reactions on coral-like shapes of barium carbonate and silica ($BaCO_3/SiO_2$) (Figure 4.2a, see Appendix A.1.1 for details).

In the first step we exchange the $Ba^{2+}$ for $Pb^{2+}$ while preserving the shape of the original nanocomposite (Figure 4.2, Appendix A.1.7). During this exchange reaction it is essential to prevent the dissolution of $BaCO_3$ and subsequent nucleation of $PbCO_3$, as such dissolution/recrystallization processes hinder a preservation of the shape[38]. Since the dissolution/recrystallization is relatively slow for high concentrations of $Pb^{2+}$, we perform the reaction in a nearly saturated aqueous solution of 0.9 M $Pb(NO_3)_2$ for 30-60 seconds in the absence of $CO_2$. This reaction is rapidly driven to completion due to the high concentration of $Pb^{2+}$ and because the thermodynamic stability of the resulting $PbCO_3$ is higher, as indicated by the solubility product of $PbCO_3$ ($K_{sp} = 7.4 \cdot 10^{-14}$), which is orders of magnitude lower than that of $BaCO_3$ ($K_{sp} = 2.58 \cdot 10^{-9}$).[25,39] Additionally, the similarities between the orthorhombic crystals structures of both $BaCO_3$ and $PbCO_3$ minimize distortion of the unit cell during the conversion. Energy Dispersive X-ray Spectroscopy (EDS) confirms the complete exchange from $Ba^{2+}$ to $Pb^{2+}$ throughout the interior of the nanocomposite architecture (Figure 4.2). As expected, the orthorhombic crystal structure is maintained during the conversion of $BaCO_3$ into $PbCO_3$, which can be concluded from the nearly identical X-Ray powder diffraction (XRPD) data. Scanning Electron Microscopy (SEM) reveals the preservation of the entire architecture with nanoscale fidelity, while even the initial crystallographic alignment along the c-axis of the nanocrystals is retained according to the Maltese cross birefringent pattern of both the $BaCO_3$ and $PbCO_3$ using polarization microscopy (Appendix A.3.1).[16] This preservation of nanoscale features and crystallographic orientation suggests a transformation in which a single crystal of one phase transforms into a single crystal of a different phase while inheriting its orientation from the original crystal, thus constituting an additional level of complexity over dissolution/recrystallization mechanisms.

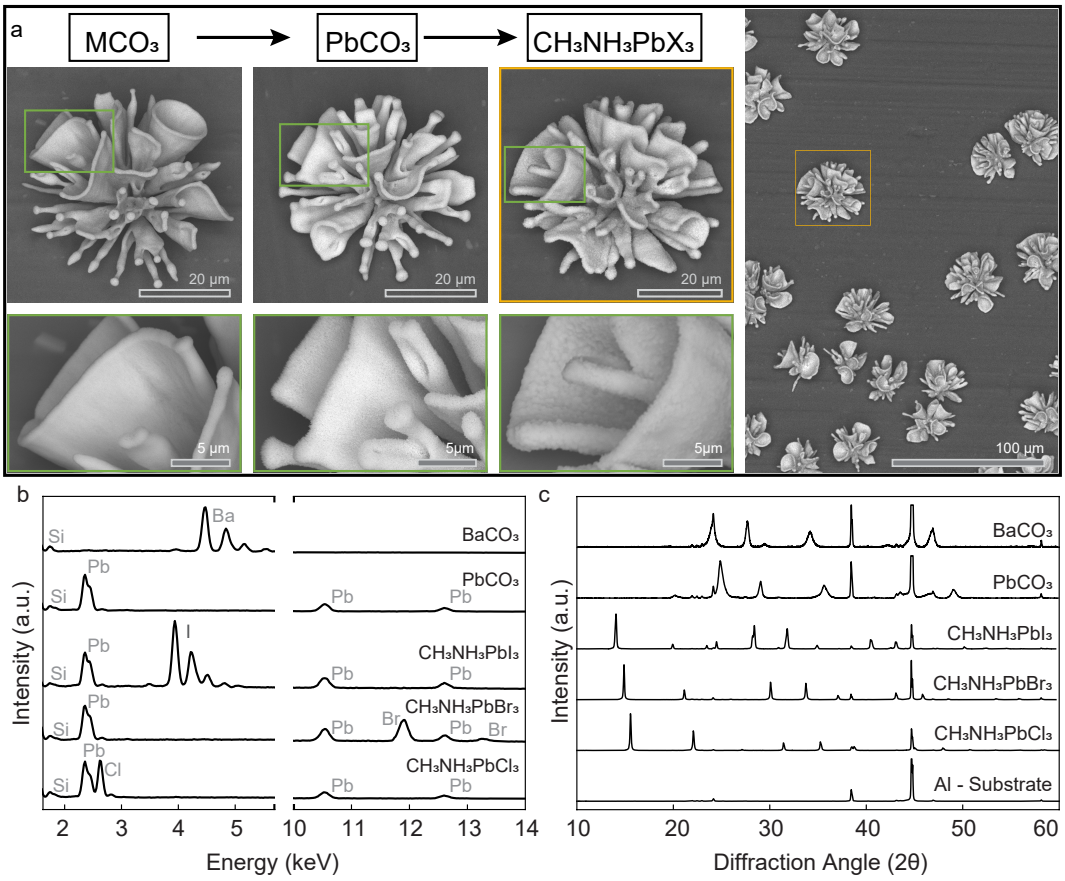


**Figure 4.2: Conversion of metal carbonate nanocomposites into $CH_3NH_3PbX_3$ perovskites. a,** Scanning electron microscope (SEM) images of the sequential reaction products, and overview images of the final perovskite product, shown for the conversion of $BaCO_3$ into $CH_3NH_3PbBr_3$ (see Appendix A.1.7 for details and SEM images of the $CH_3NH_3PbI_3$ and $CH_3NH_3PbCl_3$ nanocomposite architectures, respectively). **b,** Energy dispersion spectroscopy of nanocomposites showing the conversion of $BaCO_3$ into $PbCO_3$ and the final product $CH_3NH_3PbX_3$. **c,** X-ray powder diffraction data for nanocomposites showing the conversion of $BaCO_3$ (witherite) into $PbCO_3$ (cerrusite) and the final product $CH_3NH_3PbX_3$.

In the second step we convert the resulting $PbCO_3/SiO_2$ architectures directly into the desired $CH_3NH_3PbX_3/SiO_2$. The required exchange of anions has remained challenging in other systems thus far, since the larger size and lower diffusivity of anions often leads to sluggish conversions and poor retention of the morphology.[23] Besides replacing the carbonate with a desired halide-anion X ($X = Cl^-$, $Br^-$ or $I^-$), the reaction to perovskite requires the well-established insertion of $CH_3NH_3X$ and rearranging the crystal structure to yield the perovskite.[36] We here address these challenges in a one-pot conversion by exposing the $PbCO_3/SiO_2$ architectures to an excess of gaseous $CH_3NH_3X$ at 120 °C for ca. 6 hours, which results in the direct formation of the desired perovskite ($CH_3NH_3PbX_3$).

Characterization of the resulting nanocomposite architectures shows excellent conversion of $PbCO_3$ into the desired perovskite while retaining both the shape and fine features of the starting nanocomposites (Figure 4.2). The proposed reaction cascade is as follows:

$$PbCO_3(s) + 2\,CH_3NH_3X(g) \rightleftharpoons PbX_2(s) + H_2O(g) + CO_2(g) + 2\,CH_3NH_2(g) \quad (1)$$

$$PbX_2(s) + CH_3NH_3X(g) \rightleftharpoons CH_3NH_3PbX_3(s) \quad (2)$$

In the first step, the removal of $H_2O$, $CO_2$ and $CH_3NH_2$ from the reaction mixture drives the reaction to completion, which is consistent with Le Chatelier's principle. Additionally, the removal of water prevents the undesired decomposition of the perovskite, although small concentrations of water may improve the quality of the perovskite by lowering the defect density.[40–42] In the second step, the excess amount of $CH_3NH_3X$ pushes the reaction of the intermediate $PbX_2$ to the perovskite.

To confirm the proposed reaction mechanism, we first develop a method for methylamine $CH_3NH_2$ detection. For this we use a UV-light absorbing aromatic aldehyde that reacts with methylamine to form an imine that can be detected by HPLC-UV (High performance liquid chromatograph coupled to an UV-detector, see Appendix A.1.7 for details). This analysis shows that methylamine is released during the conversion of $PbCO_3$ to the perovskite, in agreement with the first step of the proposed mechanism. Consistent with this mechanism, we can also gain direct access to the $PbX_2$ intermediate by reacting $PbCO_3$ nanocomposites with KI under acidic conditions to obtain the corresponding $PbI_2$ nanocomposites (see Appendix A.1.7). In the second step $CH_3NH_3X$ is inserted into $PbX_2$ to form $CH_3NH_3PbX_3$. This reaction is already well documented for pure $PbX_2$ crystals.[36] Using the nanocomposites of $PbI_2$ we also confirm that the nanocomposites can undergo this insertion reaction with $CH_3NH_3I$ to form the corresponding $CH_3NH_3PbI_3/SiO_2$ nanocomposite. Finally, we qualitatively investigate the relative reaction rates of the two consecutive reaction steps by partially reacting $PbCO_3/SiO_2$ nanocomposite to $CH_3NH_3PbX_3/SiO_2$ according to the one-pot conversion scheme. Analysis of these nanocomposites using XRD show no detectable amounts of the reaction intermediate $PbX_2$, suggesting that the anion exchange of $PbCO_3$ to $PbX_2$ (step 1) is relatively slow compared to the conversion of $PbX_2$ to $CH_3NH_3PbX_3$ (step 2).

The generality of our reaction scheme allows us to synthesize a range of perovskites starting from a wide choice of carbonate compounds. To demonstrate this we successfully convert nanocomposites containing $BaCO_3$, $SrCO_3$ and $CaCO_3$ into the corresponding chloride, bromide and iodide perovskites (Figure 4.2b,c, and Appendix A.1.7). It should be noted that the silica (20-25 at.% of the entire composition) is inert during the entire sequence of conversions, and merely required for controlling the shape of the original $MCO_3/SiO_2$ nanocomposite architecture before we start with the conversions.[12,16,17] However, during the conversions the silica matrix can assist in stabilizing and maintaining the overall microshape by acting as a scaffold and by hindering ripening of the nanocrystals.

## 4.3 Luminescent Properties

In order to verify the quality of our 3D-shaped perovskites and the potential for our approach in optoelectronic applications, we benchmark the photoluminescence (PL) spectra and PL lifetime of our 3D halide-perovskite nanocomposites against already reported standard thin-film perovskites. Our 3D perovskites show narrow PL emission, with the peak wavelength tunable from the blue into the near-infrared by selecting the methylammonium halide precursor (Figure 4.3 a), comparable to what has been reported in literature for thin-film perovskites.[37] The photoluminescence lifetime of 28 ns for $CH_3NH_3PbBr_3/SiO_2$ nanocomposites is also on par with standard material preparation methods of thin films (Figure 4.3 b).[37] We also see excellent PL uniformity both within and across large fields of halide-perovskite nanocomposites, confirming the complete conversion of the samples (Figure 4.3 c). Our perovskites thus perform comparable to state-of-the-art thin film perovskites, while offering the ability to straightforwardly program the 3D-shape.

Since our conversion process is to a large extent independent of the microscopic form of the mineralized architecture, a wide variety of perovskite shapes can be synthesized by first programming the shape of the starting carbonate nanocomposite and subsequently converting them into lead-halide perovskite materials.[12,17] To illustrate the versatility of our concept, we preprogram different morphologies by modulating the reaction conditions such as pH, temperature and $CO_2$ concentration during the co-precipitation process of carbonate and silica (see Appendix A.1.1 for details). Subsequently, these nanocompsite architectures can be converted to perovskites with a tunable bandgap based on the choice of methylammonium halide precursor. The photoluminescence can be seen with great spatial resolution in the cathodoluminescence (CL, Appendix A.3.3) images of a selection of perovskite spirals, trumpets, spiked corals, and vases (Figure 4.4).

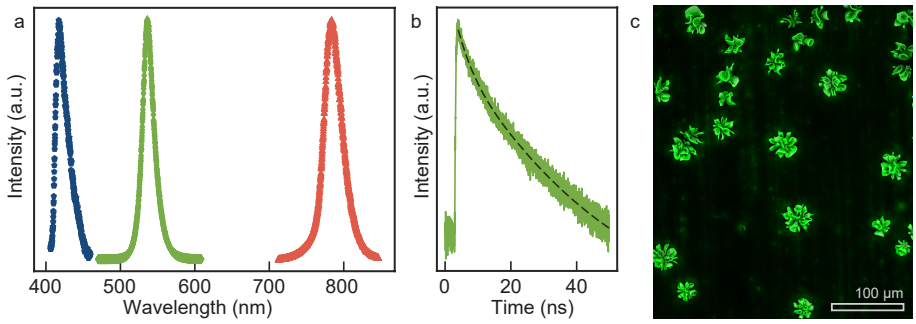


**Figure 4.3: Photoluminescence of perovskite microarchitectures.** **a,** Photoluminescence of coral-shaped synthetic microarchitectures containing lead halide perovskite $CH_3NH_3PbX_3$, X=Cl (blue trace), Br (green trace) and I (red trace), measured with excitation wavelengths of 365 nm, 405 nm and 532 nm, respectively. **b,** Photoluminescence lifetime of a $CH_3NH_3PbBr_3/SiO_2$ miroarchitecture. **c,** Overlay image of SEM and corresponding fluorescence microscopy image of a field of $CH_3NH_3PbBr_3/SiO_2$ coral shapes.

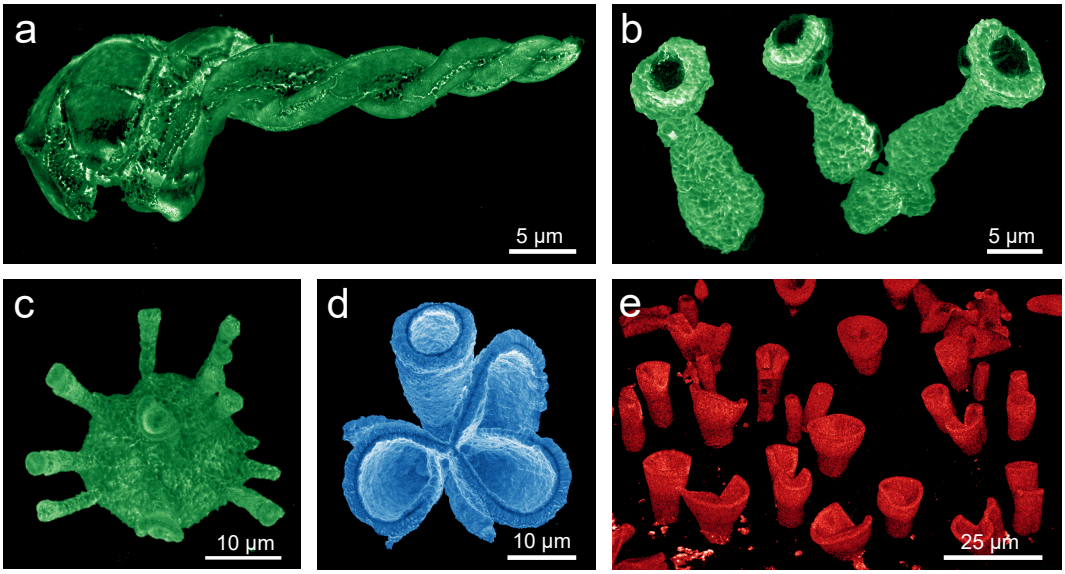


**Figure 4.4: Complex arbitrarily shaped perovskites from synthetic architectures. a-c,** Spiral (a), trumpet (b) and spiked-coral (c) shapes of $CH_3NH_3PbBr_3/SiO_2$. **d,** $CH_3NH_3PbCl_3/SiO_2$ coral shape. **e,** Field of $CH_3NH_3PbI_3/SiO_2$ vase shapes. The colours chosen for the colour scale represent the emission range of the measured cathodoluminescence, with lighter colours corresponding to higher emission.

The colors of the CL images in Figure 4.4a-e correspond to the real color of light emitted from the perovskite nanocomposites (peak wavelength), showing the tunability of the bandgap by selecting the methylammonium halide precursor. Our reaction scheme thus enables the synthesis of a wide repertoire of programmable 3D perovskites with independent control over the micro-shape and material composition.

## 4.4 Conversion of Biominerals

Our simple and flexible conversion approach also applies to naturally occurring biomineral materials made of $CaCO_3$, many of which have a comparable nanocrystalline layout and material composition to the artificially synthesized carbonate shapes.[13–15] We illustrate this concept by converting a 6x15x3 mm section of the highly intricate aragonite architecture of a cuttlefish bone (from Sepia officinalis) into perovskite, while retaining even the fine structure of the sub-micrometer-thin lamella (Figure 4.5a, Appendix A.1.7). The epitaxial relationship between aragonite and the most common $CaCO_3$ polymorph, calcite, suggests that these biominerals can be converted as well. We confirm this by converting a 3.5 cm sized calcite shell of a sand dollar (Mellita isometra) into $CH_3NH_3PbBr_3$. To speed up the reaction rate due to the slow mass transport in the gas phase reaction, we perform the conversion of $PbCO_3$ into perovskite in a solution containing the methylammonium halide precursor instead of the gas-phase reaction.

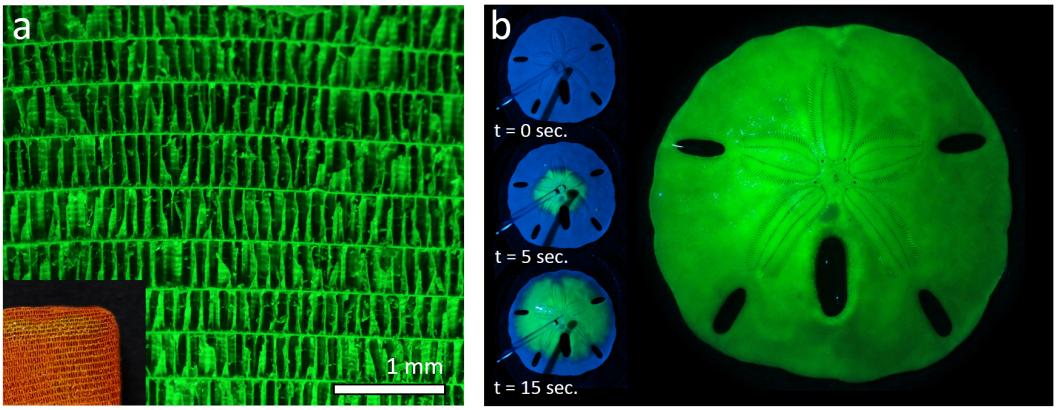


**Figure 4.5: Complex arbitrarily shaped perovskites from biological mineral architectures.** **a,** Fluorescence microscopy image of a cuttlefish bone converted into $CH_3NH_3Br_3$. Inset, Photograph under daylight illumination (image width 0.5 cm). **b,** Time-lapse fluorescence photographs under UV illumination at 365 nm of a sand dollar in 45 s from $PbCO_3$ into $CH_3NH_3PbBr_3$.

Even though a low pH can deteriorate perovskites, we here use acidic conditions to turn the carbonate of $PbCO_3$ into a good leaving group and speed up the conversion reaction. To directly visualize the transformation, we use UV illumination to observe the light emission from the forming perovskite. The reaction is remarkably fast, with a 3.5 cm sand dollar converting in less than one minute, as is clearly visible from the bright fluorescent true-color camera images (Figure 4.5b). This experiment also gives insight in the conversion depth that can be achieved: for a sand dollar with a thickness of ca. 1 mm, we find that the outer 100 µm is converted into perovskite, giving rise to a core-shell layout with a semiconductor on the outside and an insulating $CaCO_3$ interior (Appendix A.1.7). Thus, our transformation scheme is also effective on macroscopic scales, yet preserves even the finest features with sub-micrometer fidelity.

## 4.5 Conclusion

In summary, we present a platform to gain independent control over both shape and composition of 3D functional materials, using a two-step reaction scheme that converts biological and programmable synthetic carbonate-salt architectures into perovskites. With calcium carbonate being the most abundant biomineral in nature, our reaction thus gives access to the vast catalogue of biological architectures, leveraging nature's exquisite morphogenesis strategies with chemical conversion into broadly applicable functional materials.[4–8,10–19,43] Furthermore, the control offered by bio-inspired synthetic crystallization strategies over parameters such as nucleation position, shape, and crystal size can now be combined with the unprecedented material performance of artificially made halide perovskites with tunable optical and electronic properties.

# Bibliography


[1] Lee, M. M., Teuscher, J., Miyasaka, T., Murakami, T. N., and Snaith, H. J. *Science* **338**(6107), 643–647 (2012).

[2] Kojima, A., Teshima, K., Shirai, Y., and Miyasaka, T. *Journal of the American Chemical Society* **131**(17), 6050–6051 (2009).

[3] Kim, H. S., Lee, C. R., Im, J. H., Lee, K. B., Moehl, T., Marchioro, A., Moon, S. J., Humphry-Baker, R., Yum, J. H., Moser, J. E., Grätzel, M., and Park, N. G. *Scientific Reports* **2**, 1–7 (2012).

[4] Fratzl, P. *Journal of the Royal Society Interface* **4**(15), 637–642 (2007).

[5] Nudelman, F. and Sommerdijk, N. A. *Angewandte Chemie - International Edition* **51**(27), 6582–6596 (2012).

[6] Studart, A. R. *Advanced Materials* **24**(37), 5024–5044 (2012).

[7] Wegst, U. G., Bai, H., Saiz, E., Tomsia, A. P., and Ritchie, R. O. *Nature Materials* **14**(1), 23–36 (2015).

[8] Giosia, M. D., Polishchuk, I., Weber, E., Fermani, S., Pasquini, L., Pugno, N. M., Zerbetto, F., Montalti, M., Calvaresi, M., Falini, G., and Pokroy, B. *Advanced Functional Materials* **26**(30), 5569–5575 (2016).

[9] Xu, S., Yan, Z., Jang, K.-I., Huang, W., Fu, H., Kim, J., Wei, Z., Flavin, M., McCracken, J., Wang, R., Badea, A., Liu, Y., Xiao, D., Zhou, G., Lee, J., Chung, H. U., Cheng, H., Ren, W., Banks, A., Li, X., Paik, U., Nuzzo, R. G., Huang, Y., Zhang, Y., and Rogers, J. A. *Science* **347**(6218), 154–159 (2015).

[10] Nie, Z., Petukhova, A., and Kumacheva, E. *Nature Nanotechnology* **5**(1), 15–25 (2010).

[11] Bao, Z., Weatherspoon, M. R., Shian, S., Cai, Y., Graham, P. D., Allan, S. M., Ahmad, G., Dickerson, M. B., Church, B. C., Kang, Z., Abernathy, H. W., Summers, C. J., Liu, M., and Sandhage, K. H. *Nature* **446**(7132), 172–175 (2007).

[12] Kaplan, C. N., Noorduin, W. L., Li, L., Sadza, R., Folkertsma, L., Aizenberg, J., and Mahadevan, L. *Science* **355**(6332), 1395–1399 (2017).

[13] Lowenstam, H. A. and Weiner, S. *On Biomineralization*. Oxford Univ. Press, (1989).

[14] Mann, S. *Biomineralization*. Oxford Univ. Press, (2002).

[15] Mann, S. and Ozin, G. A. *Nature* **382**(6589), 313–318 (1996).

[16] Garcia-Ruiz, J. M., Melero-Garcia, E., and Hyde, S. T. *Science* **323**(5912), 362–365 (2009).

[17] Noorduin, W. L., Grinthal, A., Mahadevan, L., and Aizenberg, J. *Science* **340**(6134), 832–837 (2013).

[18] Sandhage, K. H., Dickerson, M. B., Huseman, P. M., Caranna, M. A., Clifton, J. D., Bull, T. A., Heibel, T. J., Overton, W. R., and Schoenwaelder, M. E. *Advanced Materials* **14**(6), 429–433 (2002).

[19] Weatherspoon, M. R., Allan, S. M., Hunt, E., Cai, Y., and Sandhage, K. H. *Chemical Communications* (5), 651–653 (2005).

[20] Wu, H., Hu, L., Rowell, M. W., Kong, D., Cha, J. J., McDonough, J. R., Zhu, J., Yang, Y., McGehee, M. D., and Cui, Y. *Nano Letters* **10**(10), 4242–4248 (2010).

[21] Son, D. H., Hughes, S. M., Yin, Y., and Alivisatos, A. P. *Science* **306**(5698), 1009–1012 (2004).

[22] Robinson, R. D., Sadtler, B., Demchenko, D. O., Erdonmez, C. K., Wang, L.-W., and Alivisatos, A. P. *Science* **317**(5836), 355–358 (2007).

[23] Beberwyck, B. J., Surendranath, Y., and Alivisatos, A. P. *Journal of Physical Chemistry C* **117**(39), 19759–19770 (2013).

[24] Putnis, A. *Mineralogical Magazine* **66**(05), 689–708 (2002).

[25] De Trizio, L. and Manna, L. *Chemical Reviews* **116**(18), 10852–10887 (2016).

[26] Hodges, J. M., Kletetschka, K., Fenton, J. L., Read, C. G., and Schaak, R. E. *Angewandte Chemie - International Edition* **54**(30), 8669–8672 (2015).

[27] Wu, H., Sato, R., Yamaguchi, A., Kimura, M., Haruta, M., Kurata, H., and Teranishi, T. *Science* **351**(6279), 1306–1310 (2016).

[28] Stebe, K., Lewandowski, E., and Ghosh, M. *Science* **325**, 159–161 (2009).

[29] Boneschanscher, M. P., Evers, W. H., Geuchies, J. J., Altantzis, T., Goris, B., Rabouw, F. T., van Rossum, S. A. P., van der Zant, H. S. J., Siebbeles, L. D. A., Van Tendeloo, G., Swart, I., Hilhorst, J., Petukhov, A. V., Bals, S., and Vanmaekelbergh, D. *Science* **344**(6190), 1377–1380 (2014).

[30] Geuchies, J. J., Van Overbeek, C., Evers, W. H., Goris, B., De Backer, A., Gantapara, A. P., Rabouw, F. T., Hilhorst, J., Peters, J. L., Konovalov, O., Petukhov, A. V., Dijkstra, M., Siebbeles, L. D., Van Aert, S., Bals, S., and Vanmaekelbergh, D. *Nature Materials* **15**(12), 1248–1254 (2016).

[31] Miszta, K., De Graaf, J., Bertoni, G., Dorfs, D., Brescia, R., Marras, S., Ceseracciu, L., Cingolani, R., Van Roij, R., Dijkstra, M., and Manna, L. *Nature Materials* **10**(11), 872–876 (2011).

[32] Zhang, W., Eperon, G. E., and Snaith, H. J. *Nature Energy* **1**(6) (2016).

[33] Polman, A. and Atwater, H. A. *Nature Publishing Group* **11**(3), 174–177 (2012).

[34] Chen, K. and Tüysüz, H. *Angewandte Chemie - International Edition* **54**(46), 13806–13810 (2015).

[35] Ashley, M. J., O'Brien, M. N., Hedderick, K. R., Mason, J. A., Ross, M. B., and Mirkin, C. A. *Journal of the American Chemical Society* **138**(32), 10096–10099 (2016).

[36] Burschka, J., Pellet, N., Moon, S. J., Humphry-Baker, R., Gao, P., Nazeeruddin, M. K., and Grätzel, M. *Nature* **499**(7458), 316–319 (2013).

[37] Sheng, R., Ho-Baillie, A., Huang, S., Chen, S., Wen, X., Hao, X., and Green, M. A. *Journal of Physical Chemistry C* **119**(7), 3545–3549 (2015).

[38] Yuan, K., Lee, S. S., De Andrade, V., Sturchio, N. C., and Fenter, P. *Environmental Science and Technology* **50**(23), 12984–12991 (2016).

[39] *Solubility Product Constants*, (North Carolina State University, accessed on 01-05-2017), www4.ncsu.edu/˜franzen/public_html/CH201/data/Solubility_Product_Constants.pdf.

[40] Niu, G., Li, W., Meng, F., Wang, L., Dong, H., and Qiu, Y. *J. Mater. Chem. A* **2**(3), 705–710 (2014).

[41] Tenuta, E., Zheng, C., and Rubel, O. *Scientific Reports* **6**(July), 1–8 (2016).

[42] Eperon, G. E., Habisreutinger, S. N., Leijtens, T., Bruijnaers, B. J., Van Franeker, J. J., Dequilettes, D. W., Pathak, S., Sutton, R. J., Grancini, G., Ginger, D. S., Janssen, R. A., Petrozza, A., and Snaith, H. J. *ACS Nano* **9**(9), 9380–9393 (2015).

[43] Li, L., Fijneman, A. J., Kaandorp, J. A., Aizenberg, J., and Noorduin, W. L. *Proceedings of the National Academy of Sciences* **115**(14), 201712911 (2018).

# Chapter 5

## Ion Exchange without Carbonate Intermediate

Shape-preserving conversion offers a promising strategy to transform self-assembled structures into advanced functional components with customizable composition and shape. Specifically, the assembly of barium carbonate nanocrystals and amorphous silica nanocomposites ($BaCO_3/SiO_2$) offers a plethora of programmable three-dimensional (3D) microscopic geometries, and the nanocrystals can subsequently be converted into functional chemical compositions while preserving the original 3D geometry. Despite this progress, the scope of these conversion reactions has been limited by the requirement to form carbonate salt intermediates. Here we overcome this limitation using a single step cation/anion exchange that is driven by the temporal pH change at the converting nanocomposite. We demonstrate the proof-of-principle by converting $BaCO_3/SiO_2$ nanocomposites into tin-containing nanocomposites, a metal without a stable carbonate. We find that $BaCO_3/SiO_2$ nanocomposites convert in a single step into hydroromarchite nanocomposites ($Sn_3(OH)_2O_2/SiO_2$) with excellent preservation of the 3D geometry and fine features. We explore the versatility and tunability of these $Sn_3(OH)_2O_2/SiO_2$ nanocomposites as precursor for functional compositions by developing shape-preserving conversion routes to two desirable compositions: transparent, conducting cassiterite ($SnO_2$), and semiconducting tin perovskite ($CH_3NH_3SnX_3$, with X = I, or Br). Ultimately, these findings may enable integrating of functional chemical compositions into advanced morphologies for next-generation opto-electronic devices.

This work has been submitted for scientific publication.

## 5.1 Introduction

Bioinspired strategies offer tremendous opportunities for ordering building blocks across multiple length scales into advanced functional materials.[1–14] The coprecipitation of metal carbonate nanocrystals ($MCO_3$, with M = $Ba^{2+}$, $Sr^{2+}$ or $Ca^{2+}$) and amorphous silica ($SiO_2$) offers an ideal system to explore this potential, as their co-assembly yields highly intricate yet easily controllable three-dimensional (3D) nanocomposite shapes.[15–17] Rational modulation of the reaction conditions (pH, $CO_2$ concentration, temperature etc.) enables steering of the assembly towards a wide diversity of shapes (e.g. coral, vase, helix forms) that can be further patterned and hierarchically organized.

Although the initial self-assembly process constrains the chemical composition of the nanocrystals to metal carbonate salts, post-assembly procedures have been developed to overcome this limitation. For example, microhelices have been decorated with magnetite mesocrystals, and silane chemistry enables chemical functionalization of the silica matrix of the nanocomposites.[18,19] Alternatively, the shape-preserving conversion reactions described in this thesis allow for complete conversion of the $BaCO_3$ nanocrystals into a wide selection of lead perovskites and metal chalcogenides with desirable optical, electronical, and chemical properties while inheriting the three-dimensional shape and fine features of the original nanocomposite.[20] These conversions are achieved by sequential series of cation and anion exchange reactions. Although many different chemical compositions have been achieved in this way, all of these conversions require the formation of a carbonate intermediate. Since many interesting compounds do not form a metal carbonate, this limits the choice of accessible chemical compositions for furnishing nanocomposites with advanced functionalities.

The mechanistic details of conversion reactions may offer inspiration for overcoming this challenge. From a thermodynamic perspective, the viability of exchange reactions can be rationalized by the difference in formation energy of the forming and disappearing salt and the reduction potential of the involved ions.[21,22] This rationalization is usually complemented by considerations of the in situ reaction conditions during transformation, as it is well-known that the local chemistry plays a major role in this process.[22–24] Especially the reaction conditions near the solid-liquid interface, the so-called reaction zone, are important and can be entirely different from the bulk solution. We hypothesize that the temporary local concentration gradients in the reaction zone may offer new reaction mechanisms for previously impossible conversion reactions.

In this chapter, we demonstrate that chemical gradients in the local reaction zone enable conversion of barium carbonate nanocomposites ($BaCO_3/SiO_2$) into a selection of tin containing nanocomposites. A straightforward cation exchange is not possible in this conversion, as tin does not form a stable carbonate salt.[25] However, we find that the temporary local concentrations during the conversion, in combination with the poor solubility of tin in water, results in the conversion towards hydroromarchite ($Sn_3(OH)_2O_2$). Furthermore, we explore the versatility and tunability of these $Sn_3(OH)_2O_2/SiO_2$ nanocomposites as precursor for functional compositions by developing shape-preserving conversion routes to two desirable compositions: transparent, conducting cassiterite ($SnO_2$), and semiconducting tin perovskite ($CH_3NH_3SnX_3$, with X = $I^-$, or $Br^-$).[26–33] Hence, by demonstrating this conversion mechanism, we open up pathways to new functional materials with controllable shapes.

## 5.2 Conversion without a Carbonate Intermediate

We study the ion exchange to tin from $BaCO_3/SiO_2$ coral-shaped nanocomposites. We assemble $BaCO_3/SiO_2$ coral-shapes following previously reported procedures.[16] Subsequently, these coral-shapes are immersed in an aqueous solution of 100 mM $SnCl_2$ under a nitrogen atmosphere (see Appendix A.1.8 for details). Within 30 seconds of immersion, the barium ions in the nanocomposites are completely replaced by tin according to energy dispersive X-ray spectroscopy (EDS, Figure 5.1B). Furthermore, scanning electron microscopy (SEM) shows excellent shape-preservation with sub-micrometer fidelity (Figure 5.1A).

Remarkably, X-ray diffraction (XRD, Figure 5.1C) reveals that the nanocrystals inside the nanocomposites are composed of hydroromarchite ($Sn_3(OH)_2O_2$).[34] Thus, besides the barium cations being replaced for tin, the carbonate anions are also substituted with oxyhydroxide. Infrared spectroscopy (IR) confirms that the characteristic carbonate fingerprint peak ($\sim$ 1450 $cm^{-1}$) of $BaCO_3$ disappears after the conversion (Figure 1D). Hence, both cations and anions are replaced in a single step during this shape-preserving chemical conversion.

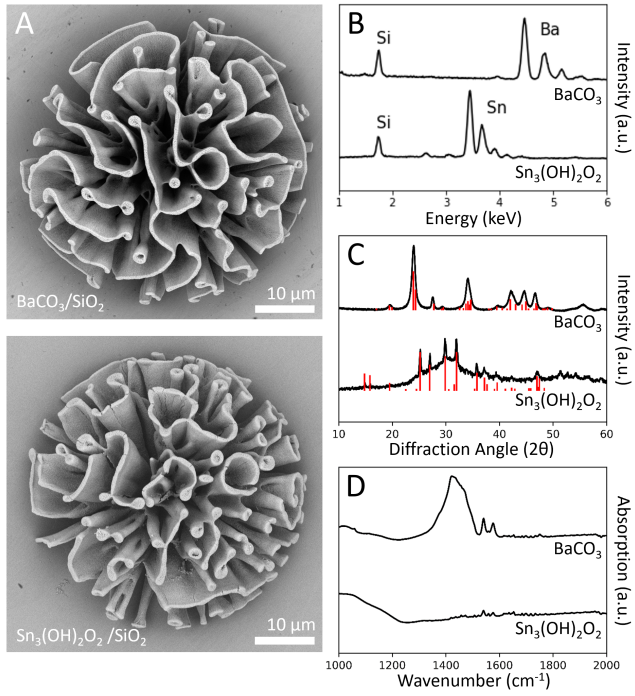


**Figure 5.1: Conversion from $BaCO_3/SiO_2$ to $Sn_3(OH)_2O_2/SiO_2$. A,** SEM images of (different) nanocomposites before (top) and after (bottom) conversion, showing that the coral-like shape is retained. **B,** EDS measurements of nanocomposites before (top) and after (bottom) conversion, indicating full replacement of barium with tin. **C,** XRD characterization showing the conversion of $BaCO_3$ to $Sn_3(OH)_2O_2$ (red lines indicate reference peaks). **D,** IR spectrum showing the disappearance of the fingerprint peak of an carbonate anion at 1450 $cm^{-1}$ after conversion to $Sn_3(OH)_2O_2$.

We hypothesize during the concurrent shape-preserving cation/anion exchange the following cascade of reactions occurs (Figure 2):

$$Sn^{2+}(aq) + H_2O(l) \rightarrow SnOH^+(aq) + H^+(aq) \tag{5.1}$$

$$3BaCO_3(s) + 3SnOH^+(aq) + H_2O(l) \rightarrow Sn_3(OH)_2O_2(s) + 3Ba^{2+}(aq) + 3HCO_3^-(l) \tag{5.2}$$

$$Sn_3(OH)_2O_2(s) + 3H^+(aq) \rightarrow 3Sn(OH)^+(aq) + H_2O(l) \tag{5.3}$$

Here, tin ions hydrolyze in water, forming $SnOH^+$ and acid (reaction 5.1), which is consistent with an observed decrease in the pH from 7.0 to 2.0. This acidic solution leads to the dissolution of $BaCO_3$ nanocrystals in the nanocomposite and thereby locally increases the pH in the close vicinity of the nanocomposite. This increased local pH, combined with the high tin concentration in the solution, results in the formation of $Sn_3(OH)_2O_2$ (reaction 5.2).[35,36] Once all $BaCO_3$ is dissolved, the local pH decreases again to the acidic pH of the bulk solution. Consequently, the $Sn_3(OH)_2O_2$ in the nanocomposites dissolves as it is only stable at a pH above 3.5 (bulk pH=2.0),[37] leaving the empty silica scaffold of behind (Reaction 5.3, see Appendix A.2.7). Consistent with this mechanism, deliberately increasing the pH of the bulk solution to 13-14 by adding a base (1.0M NaOH) results in precipitation of $Sn_3(OH)_2O_2$ in the entire solution (see Appendix A.2.7).[38] Thus, the dissolution of $BaCO_3$ creates a spatiotemporal reaction zone that enables the precipitation of the $Sn_3(OH)_2O_2$ in the nanocomposite with preservation of the original 3D shape.

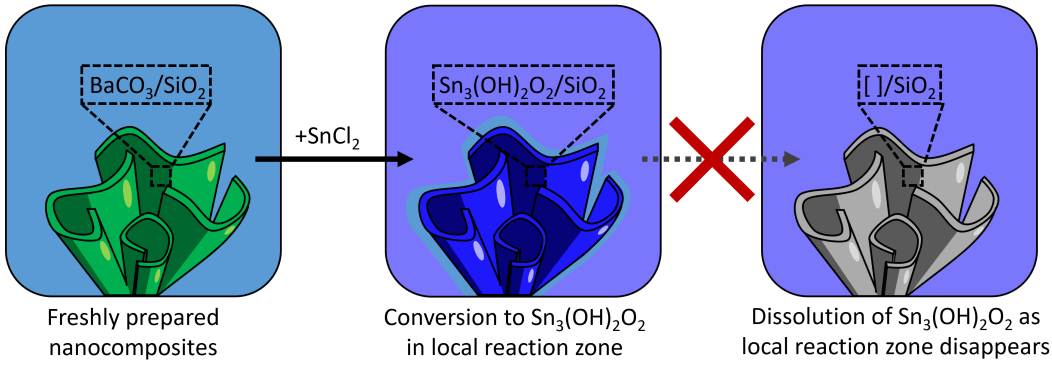


**Figure 5.2: Proposed conversion mechanism of $BaCO_3$ to $Sn_3(OH)_2O_2$ in nanocomposites.** $Sn^{2+}$ hydrolysis decreases the pH of water (reaction 5.1). High pH is indicated with light blue (left), low pH is indicated with purple (middle, right). Locally, the pH increases again by dissolving $BaCO_3$ (middle, indicated with light blue around the nanocomposite), which causes $Sn_3(OH)_2O_2$ to precipitate (reaction 5.2). Once all $BaCO_3$ is dissolved, the local pH decreases to the bulk pH, thereby initiating dissolution of $Sn_3(OH)_2O_2$ (right, reaction 5.3).

## 5.3 Conversions from a Carbonate-less Intermediate

The shape-preservation reaction to $Sn_3(OH)_2O_2/SiO_2$ nanocomposites opens up opportunities for developing further conversion pathways towards shape-controlled 3D morphologies with desirable tin compositions. We explore this potential for the conversion of $Sn_3(OH)_2O_2$ to tin dioxide (cassiterite, $SnO_2$). $SnO_2$ is a transparent conductor that is widely used for optoelectronic and battery applications, where shape-controlled 3D morphologies could offer new and improved functionalities.[26–29] Previous studies have already shown that $Sn_3(OH)_2O_2$ crystals can be converted into $SnO_2$ *via* dehydration and subsequent oxidation following:[39–41]

$$Sn_3(OH)_2O_2(s) \rightarrow 3SnO(s) + H_2O(g) \tag{5.4}$$

$$2SnO(s) + O_2(g) \rightarrow 2SnO_2(s) \tag{5.5}$$

So far, these reactions have not demonstrated shape preservation, as the mechanical stress during the dehydration and oxidation processes destroy the morphology of the original crystal. However, the nanocomposite layout in our system has already shown retention of the coral-shape is possible during the conversion reaction from $BaCO_3$ to $Sn_3(OH)_2O_2$, as the supporting silica matrix provides mechanical support during the conversion reaction, while the nanocrystals improve the chemical reactivity.[20] We rationalize that these shape-preserving properties of the nanocomposites can also be utilized for the conversion towards $SnO_2$.

To perform the conversion, we position the $Sn_3(OH)_2O_2/SiO_2$ nanocomposites in a tube oven that is open to air. The oven is heated to 200 °C for 3 hours to induce thermal dehydration (Reaction 5.4), and subsequently heated for 3 hours at 600 °C to form $SnO_2$ (Figure 5.3A, Reaction 5.5). XRD and EDS analysis confirm complete conversion of the nanocrystals in the nanocomposite to tetragonal $SnO_2$ (Figure 5.3C and D), while electron microscopy shows excellent preservation of the microscopic features of the nanocomposite (Figure 5.3B). Thus, the nanocomposites retain their coral-like shape while the nanocrystalline interior is completely converted to $SnO_2$.

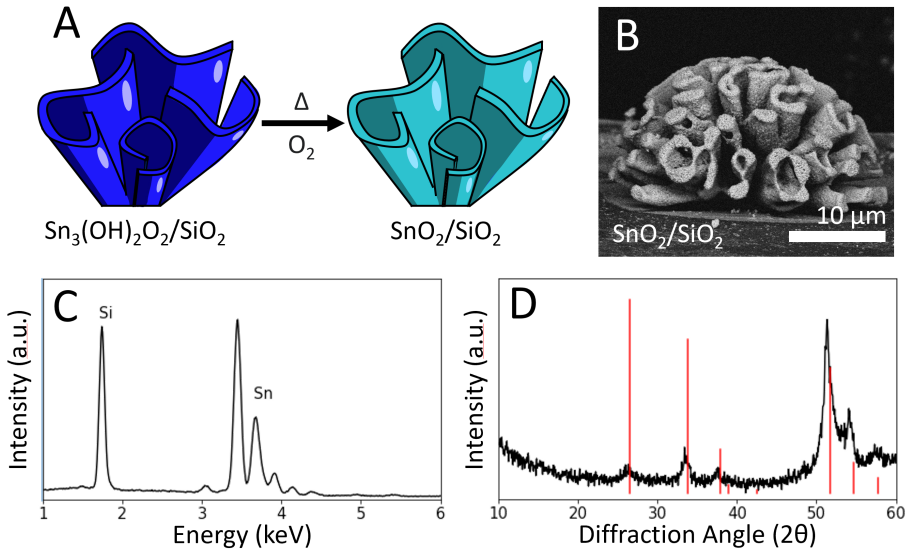


**Figure 5.3: Conversion of $Sn_3(OH)_2O_2$ to $SnO_2$ nanocomposite. A,** Cartoon representation of the conversion from $Sn_3(OH)_2O_2$ to $SnO_2$, which occurs at elevated temperatures in an oxygen-rich environment. **B,** SEM of the resulting $SnO_2/SiO_2$ nanocomposites, showing preservation of the coral-like shape. **C,** EDS and **D,** XRD confirming complete conversion to $SnO_2$ (red lines indicate $SnO_2$ reference peaks).

To demonstrate the versatility and tunability of $Sn_3(OH)_2O_2/SiO_2$ nanocomposites as precursor for functional compositions, we develop a second conversion route towards shape-controlled tin methylammonium perovskites ($CH_3NH_3SnX_3$, with X = $Br^-$ or $I^-$). These semiconductors have a tunable bandgap in the visible and near infrared spectrum, which makes them attractive for photovoltaic applications. Moreover, tin perovskites have gained attention as an environmentally friendly alternative to the widely popular lead perovskites, yet control over the 3D morphology has remained limited.[30–33] Inspired by previous conversions to lead halide perovskites,[20] we envisage that conversion of $Sn_3(OH)_2O_2$ to $CH_3NH_3SnX_3$ may be achieved by reaction with methylammonium halide ($CH_3NH_3X$, with X = $Br^-$ or $I^-$) following:

$$Sn_3(OH)_2O_2(s) + 9CH_3NH_3X(s) \rightarrow 3CH_3NH_3SnX3(s) + 4H_2O(g) + 6CH_3NH_3(g) \quad (5.6)$$

We show the proof-of-principle for the conversion towards methylammonium bromide tin perovskite ($CH_3NH_3SnBr_3$). $Sn_3(OH)_2O_2/SiO_2$ nanocomposites and $CH_3NH_3Br$ are placed in a tube oven, which is heated to 120 °C for 30 minutes, and afterwards passively cooled down back to room temperature. SEM analysis shows that the initial macroscopic geometry is well-preserved (Figure 5.4B). XRD and EDS analysis confirm complete conversion of the nanocrystals in the resulting nanocomposites are completely converted to orthorhombic $CH_3NH_3SnBr_3$, as shown by Figure 5.4E,F. Reaction scheme 5.6 suggests that selecting the methylammonium halide precursor enables control over the halide moiety in the perovskite. Indeed, reaction of $Sn_3(OH)_2O_2$ nanocomposites with $CH_3NH_3SnI_3$ results in conversion to methylammonium iodide tin perovskite ($CH_3NH_3SnI_3$, Figure 5.4C,E,F).

Control of the halide moiety during the conversion offers tunability of the bandgap of the perovskite semiconductor. We characterize this bandgap using photoluminescence (PL) spectroscopy. The $CH_3NH_3SnBr_3/SiO_2$ and $CH_3NH_3SnI_3/SiO_2$ nanocomposites show PL at 610 nm and 880 nm respectively (Figure 5.4G), which is slightly blue-shifted to previous reported values, likely because of the quantum confinement of the perovskite nanocrystals in the silica matrix.[30,33,42] Photoluminescence mapping furthermore shows light emission from the entire architecture, thus offering corroborative evidence of complete conversion (Figure 5.4D). These tin perovskites nanocomposites thus have the same semiconducting properties as 2D tin perovskites, while offering the ability to straightforwardly program the 3D shape.

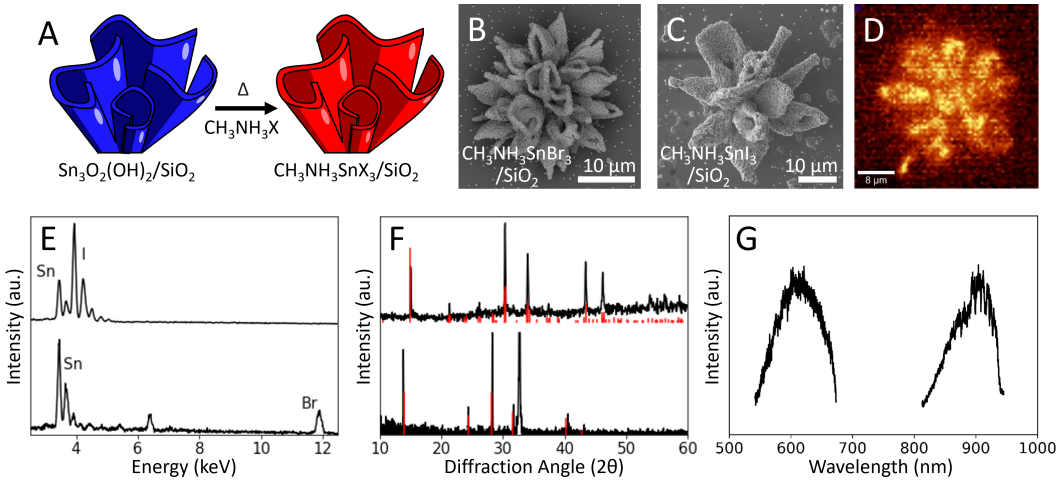


**Figure 5.4: Conversion of $Sn_3(OH)_2O_2/SiO_2$ to $CH_3NH_3SnX_3/SiO_2$ nanocomposites, with X=$Br^-$, $I^-$.** **A,** Cartoon representation of the conversion from $Sn_3(OH)_2O_2/SiO_2$ to $CH_3NH_3SnX_3/SiO_2$ nanocomposites, which occurs at elevated temperatures when $CH_3NH_3X$ is added. **B,** SEM of a $CH_3NH_3SnBr_3/SiO_2$ nanocomposite. **C,** SEM of a $CH_3NH_3SnI_3/SiO_2$ nanocomposite. **D,** PL intensity map of a $CH_3NH_3SnBr_3/SiO_2$ nanocomposite at 610 nm showing emission is coming from the nanocomposite exclusively. Lighter color indicates higher intensity. **E,** EDS and **F,** XRD analysis of coral-like nanocomposites containing $CH_3NH_3SnBr_3$ (top) and $CH_3NH_3SnI_3$ (bottom). **G,** PL spectrum of $CH_3NH_3SnBr_3/SiO_2$ (at 610 nm) and $CH_3NH_3SnI_3/SiO_2$ nanocomposites (at 880 nm).

## 5.4 Conclusion

Here, we introduce a shape-preserving conversion from $BaCO_3/SiO_2$ to $Sn_3(OH)_2O_2/SiO_2$ nanocomposites. We hypothesize that this one-step cation/anion exchange results from a cascade of reactions that are driven by the local pH in the reaction zone. We show that the $Sn_3(OH)_2O_2$ can straightforwardly be converted to functional tin compositions: the semiconductor tin perovskite ($CH_3NH_3SnX_3$) and the conductor tin oxide ($SnO_2$), while maintaining the 3-D geometry and fine features of the original $BaCO_3/SiO_2$ nanocomposite. We envisage that localized reaction zones in nanocomposites may be further exploited for developing conversion routes towards a range of desirable metal nanocomposite compositions, especially ones that lack a stable carbonate intermediate (e.g. molybdenum, ruthenium or palladium). Ultimately, these findings may enable integrating of functional chemical compositions into advanced morphologies for next-generation opto-electronic devices.

# Bibliography


[1] Jiang, W., Qu, Z. B., Kumar, P., Vecchio, D., Wang, Y., Ma, Y., Bahng, J. H., Bernardino, K., Gomes, W. R., Colombari, F. M., Lozada-Blanco, A., Veksler, M., Marino, E., Simon, A., Murray, C., Muniz, S. R., de Moura, A. F., and Kotov, N. A. *Science* **368**(6491), 642–648 (2020).

[2] Aizenberg, J., Weaver, J. C., Thanawala, M. S., Sundar, V. C., Morse, D. E., and Fratzl, P. *Science* **309**(5732), 275–278 (2005).

[3] Mann, S. and Ozin, G. A. *Nature* **382**(6589), 313–318 jul (1996).

[4] Meldrum, F. C. and Coelfen, H. *Chemical Reviews* **108**(11), 4332–4432 nov (2008).

[5] Lowenstam, H. A. and Weiner, S. *On Biomineralization*. Oxford Univ. Press, (1989).

[6] Eder, M., Amini, S., and Fratzl, P. *Science* **362**(6414), 543–547 (2018).

[7] Begley, M. R., Gianola, D. S., and Ray, T. R. *Science* **364**(6447) (2019).

[8] Bargardi, F. L., Le Ferrand, H., Libanori, R., and Studart, A. R. *Nature Communications* **7**, 1–8 (2016).

[9] Shevchenko, E. V., Talapin, D. V., Kotov, N. A., O'Brien, S., and Murray, C. B. *Nature* **439**(7072), 55–59 (2006).

[10] Wegst, U. G., Bai, H., Saiz, E., Tomsia, A. P., and Ritchie, R. O. *Nature Materials* **14**(1), 23–36 (2015).

[11] Whitesides, G. M. and Grzybowski, B. *Science* **295**(5564), 2418–2421 (2002).

[12] Singh, G., Chan, H., Baskin, A., Gelman, E., Repnin, N., Král, P., and Klajn, R. *Science* **345**(6201), 1149–1153 (2014).

[13] Vogel, N., Retsch, M., Fustin, C. A., Del Campo, A., and Jonas, U. *Chemical Reviews* **115**(13), 6265–6311 (2015).

[14] Studart, A. R. *Advanced Materials* **24**(37), 5024–5044 (2012).

[15] García-ruiz, J. M., Melero-García, E., and Hyde, S. T. *Science* **323**, 362–366 (2009).

[16] Noorduin, W. L., Grinthal, A., Mahadevan, L., and Aizenberg, J. *Science (New York, N.Y.)* **340**(6134), 832–7 (2013).

[17] Kaplan, C. N., Noorduin, W. L., Li, L., Sadza, R., Folkertsma, L., Aizenberg, J., and Mahadevan, L. *Science* **355**(6332), 1395–1399 (2017).

[18] Opel, J., Wimmer, F. P., Kellermeier, M., and Cölfen, H. *Nanoscale Horizons* **1**(2), 144–149 (2016).

[19] Opel, J., Brunner, J., Zimmermanns, R., Steegmans, T., Sturm, E., Kellermeier, M., Cölfen, H., and García-Ruiz, J. M. *Advanced Functional Materials* **29**(37), 1–7 (2019).

[20] Holtus, T., Helmbrecht, L., Hendrikse, H. C., Baglai, I., Meuret, S., Adhyaksa, G. W., Garnett, E. C., and Noorduin, W. L. *Nature Chemistry* **10**(7), 740–745 (2018).

[21] De Trizio, L. and Manna, L. *Chemical Reviews* **116**(18), 10852–10887 (2016).

[22] Beberwyck, B. J., Surendranath, Y., and Alivisatos, A. P. *Journal of Physical Chemistry C* **117**(39), 19759–19770 (2013).

[23] Backhaus-Ricoult, M. *Annual Review of Materials Research* **33**(1), 55–90 (2003).

[24] Putnis, A. *Science* **343**(6178), 1441–1442 (2014).

[25] Lothenbach, B., Ochs, M., Wanner, H., and Yui, M. *Japan Nuclear Cycle Development Institute* , 1–356 (2004).

[26] Chen, Y. and Kanan, M. W. *Journal of the American Chemical Society* **134**(4), 1986–1989 (2012).

[27] Barsan, N. and Weimar, U. *Journal of Electroceramics* **7**(3), 143–167 (2001).

[28] Feaster, J. T., Shi, C., Cave, E. R., Hatsukade, T., Abram, D. N., Kuhl, K. P., Hahn, C., Nørskov, J. K., and Jaramillo, T. F. *ACS Catalysis* **7**(7), 4822–4827 (2017).

[29] Chen, J. S. and Lou, X. W. *Small* **9**(11), 1877–1893 (2013).

[30] Konstantakou, M. and Stergiopoulos, T. *Journal of Materials Chemistry A* **5**(23), 11518–11549 (2017).

[31] Snaith, H. J. *Journal of Physical Chemistry Letters* **4**(21), 3623–3630 (2013).

[32] Stoumpos, C. C., Malliakas, C. D., and Kanatzidis, M. G. *Inorganic Chemistry* **52**(15), 9019–9038 (2013).

[33] Hao, F., Stoumpos, C. C., Cao, D. H., Chang, R. P. H., and Kanatzidis, M. G. *Nature Photonics* **8**(6), 489–494 (2014).

[34] Footnote: The X-Ray diffractogram suggests that part of the tin composite is amorphous.

[35] Chen, X. and Grandbois, M. *Journal of Raman Spectroscopy* **44**(3), 501–506 (2013).

[36] Pettine, M., Millero, F. J., and Macchi, G. *Analytical Chemistry* **53**(7), 1039–1043 (1981).

[37] Edwards, R., Gillard, R. D., and Williams, P. A. *Mineralogical Magazine* **56**(383), 221–226 (1992).

[38] Footnote: It should be noted that in the absence of a base abhurite rather than hydroromarchite forms after ca. 30 minutes in the reaction mixture.

[39] Kitabayashi, S. and Koga, N. *Journal of Physical Chemistry C* **119**(28), 16188–16199 (2015).

[40] Wongsaprom, K., Bornphotsawatkun, R. A., and Swatsitang, E. *Applied Physics A: Materials Science and Processing* **114**(2), 373–379 (2014).

[41] Alcántara, R., Fernández Madrigal, F. J., Lavela, P., Pérez-Vicente, C., and Tirado, J. L. *Journal of Solid State Electrochemistry* **6**(1), 55–62 (2001).

[42] Walters, G., Wei, M., Voznyy, O., Quintero-Bermudez, R., Kiani, A., Smilgies, D. M., Munir, R., Amassian, A., Hoogland, S., and Sargent, E. *Nature Communications* **9**(1) (2018).

# Appendix

## Methods and Equipment

# Contents

# A.1 Synthesis and Conversion of Nanocomposite Architectures

## A.1.1 Growth of Barium Carbonate Nanocomposite Architectures

### Growth of $BaCO_3/SiO_2$ architectures on a substrate

A substrate (e.g. 2x2 cm slide of aluminum, glass or silicon) was vertically positioned in a 100 mL beaker containing $BaCl_2$ dihydrate (74 mg, 0.3 mmol) and $Na_2SiO_3$ (16 mg, 0.13 mmol) dissolved in 15 mL of water. The reaction vessel was loosely covered with a Petri dish to allow $CO_2$ from the air to slowly diffuse into the reaction mixture. The pH was measured using a VWR Scientific 8005 pH meter and adjusted by adding HCl or NaOH to a pH of 11.8 for the growth of stem, vase and coral-like architectures, or to a pH of 11.2 for the growth of spiral or leaf-like architectures (See Noorduin *et al.*, *Science*, **2013**, 340, 6134, 832-837 for more details). Typical growth times ranged between 1.5-2.0 hours, after which the substrate was removed from the solution and washed with deionized water and the architectures were converted into other metal carbonates instantly after this (see following sections). The composition of the architectures was determined using SEM, EDS and XRD as shown in Figure A.1 (a, b and c respectively). The used reference for the XRD-diffractogram can be found in the Crystallography Open Database (COD 1000033).

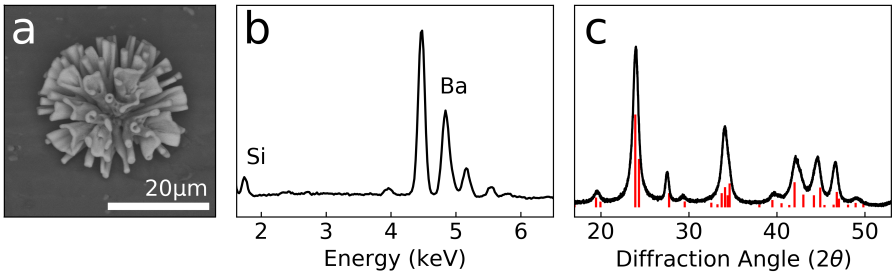


**Figure A.1: a,** SEM, **b,** EDS and **c,** XRD of $BaCO_3/SiO_2$ architectures, with reference lines depicted in red.

### Growth of $BaCO_3/SiO_2$ architectures on the meniscus

A solution of $BaCl_2$ (7.4 g, 30 mmol) in 300 mL water was added to a solution of $Na_2SiO_3$ (1.6 g, 13 mmol) in 1200 mL of water. This solution was shortly stirred and poured into a metal tray (50x30x6 cm) to maximize the surface area in contact with air, and left for 1.5 hours with a cardboard board perforated with 0.8 mm holes on top of it. After the incubation time, the bulk solution was transferred to a new metal tray while the architectures on the water meniscus were filtered and washed with de-ionized water. The resulting nanocomposite architectures were

visualized with SEM as shown in Figure A.2. For further conversions, the architectures were instantly moved from the filtration paper into the reaction mixture with a spatula.

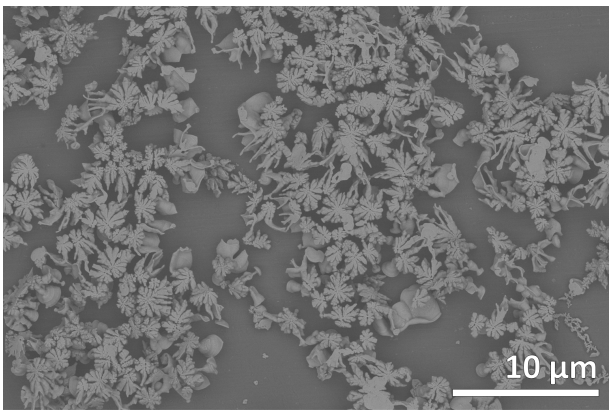


**Figure A.2:** SEM of architectures grown on the meniscus.

### A.1.2 Conversion to Cadmium Salt Nanocomposite Architectures

#### Conversion of $BaCO_3/SiO_2$ to $CdCO_3/SiO_2$ architectures

Anhydrous $CdCl_2$ (460 mg, 2.5 mmol) was dissolved in 50 mL of degassed water. Subsequently, a substrate with freshly converted $BaCO_3$ architectures was placed in the $CdCl_2$ solution for 10 minutes. The resulting $CdCO_3/SiO_2$ architectures were washed in two demineralized water baths followed by an acetone bath. After drying them to air, the architectures were analyzed using SEM, XRD and EDS (Figure A.3a, b and c respectively). The used reference for the XRD-diffractogram can be found in the American Mineralogist Crystal Structure Database (AMCSD 0004324).

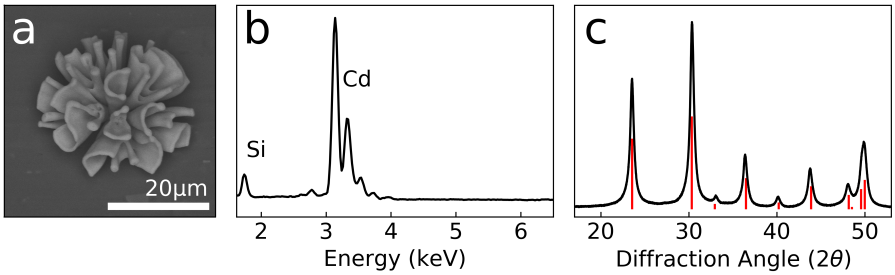


**Figure A.3:** **a,** SEM, **b,** EDS and **c,** XRD of $CdCO_3/SiO_2$ architectures, with reference lines depicted in red.

### Conversion of $CdCO_3/SiO_2$ to $CdO/SiO_2$ architectures

A substrate containing $CdCO_3/SiO_2$ architectures was placed in a single zone tube furnace, where the $CdCO_3$ nanocrystals were converted to CdO by heating the oven to 290 °C for 4 hours while the substrate was kept under nitrogen at atmospheric pressure. The resulting architectures were characterized by XRD, EDS and SEM (Figure A.4). The used reference for the XRD-diffractogram can be found in the Crystallography Open Database (COD 1011003).

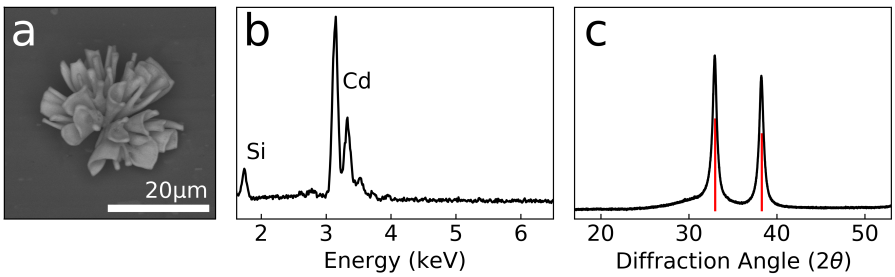


**Figure A.4:** **a,** SEM, **b,** EDS and **c,** XRD of $CdO/SiO_2$ architectures, with reference lines depicted in red.

### Conversion of $CdCO_3/SiO_2$ to $CdS/SiO_2$ architectures

A substrate containing $CdCO_3/SiO_2$ architectures was placed in a single zone tube furnace and heated to 290 °C in argon at atmospheric pressure. Upon reaching stable temperature, $H_2S$ (10 ml/min) and argon (90 ml/min) were flowed into the tube furnace for 10 minutes. After this, the tube furnace was flushed with pure argon gas and allowed to cool. The resulting $CdS/SiO_2$ architectures were characterized by XRD, SEM and EDS (Figure A.5). The used reference for the XRD-diffractogram can be found in the Crystallography Open Database (COD 1011054).

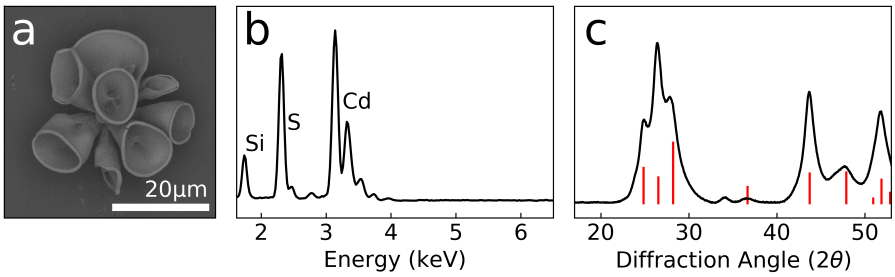


**Figure A.5:** **a,** SEM, **b,** EDS and **c,** XRD of $CdS/SiO_2$ architectures, with reference lines depicted in red.

### A.1.3 Conversion to Manganese Salt Nanocomposite Architectures

#### Conversion of $BaCO_3/SiO_2$ to $MnCO_3/SiO_2$ architectures

Anhydrous $MnCl_2$ (630 mg, 5 mmol) was dissolved in 50 mL degassed water. A substrate containing $BaCO_3/SiO_2$ architectures was placed in this solution under a nitrogen atmosphere for 60 minutes. Afterwards, the substrate was removed from the conversion solution and washed in two demineralized water baths followed by an acetone bath. The resulting architectures were characterized with SEM, EDS and XRD (Figure A.6). The used reference for the XRD-diffractogram can be found in the Crystallography Open Database (COD 5000207).

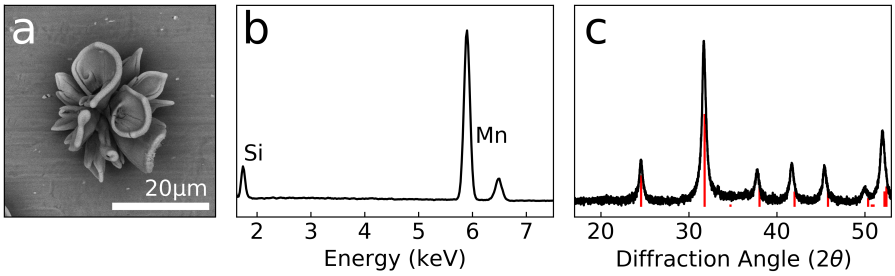


**Figure A.6:** **a,** SEM, **b,** EDS and **c,** XRD of $MnCO_3/SiO_2$ architectures, with reference lines depicted in red.

### Conversion of $MnCO_3/SiO_2$ to $Mn_3O_4/SiO_2$ architectures

A substrate with $MnCO_3/SiO_2$ architectures was placed in a single zone tube furnace under nitrogen atmosphere at atmospheric pressure. The tube furnace was heated to 540 °C for 13 hours and subsequently cooled down to room temperature. The resulting $Mn_3O_4/SiO_2$ architectures were characterized with SEM, EDS and XRD (Figure A.7). The used reference for the XRD-diffractogram can be found in the Crystallography Open Database (COD 9001302).

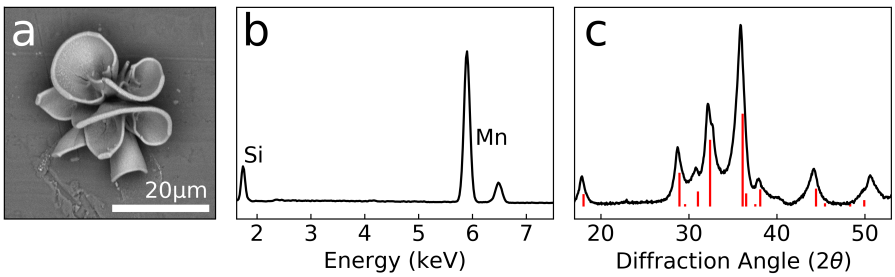


**Figure A.7:** **a,** SEM, **b,** EDS and **c,** XRD of $Mn_3O_4/SiO_2$ architectures, with reference lines depicted in red.

### Conversion of $MnCO_3/SiO_2$ to $\alpha$-$Mn_2O_3/SiO_2$ architectures

$MnCO_3/SiO_2$ architectures were placed in a single zone tube furnace that remained opened to air. The tube furnace was heated to 540 °C and after 24 hours was cooled to room temperature. The resulting $\alpha$-$Mn_2O_3/SiO_2$ architectures were characterized with SEM, EDS and XRD (Figure A.8). The used reference for the XRD-diffractogram can be found in the Crystallography Open Database (COD 9007520).

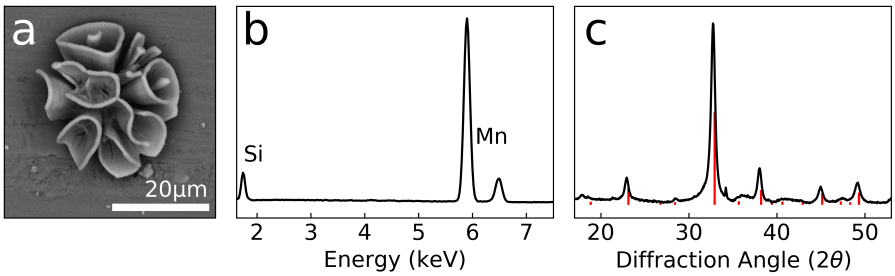


**Figure A.8:** **a,** SEM, **b,** EDS and **c,** XRD of $\alpha$-$Mn_2O_3/SiO_2$ architectures, with reference lines depicted in red.

### Conversion of $MnCO_3/SiO_2$ to $MnS/SiO_2$ architectures

$MnCO_3/SiO_2$ architectures were placed in a single zone tube furnace with argon atmosphere at atmospheric pressure. The tube furnace was heated to 400 °C and as soon as this temperature was reached, 10 vol.% $H_2S$ (10 ml/min) was added to the argon flow (90 ml/min) for 10 minutes. The resulting $MnS/SiO_2$ architectures were characterized by SEM, EDS and XRD (Figure A.9). The used reference for the XRD-diffractogram can be found in the American Mineralogist Crystal Structure Database (AMCSD 0007512).

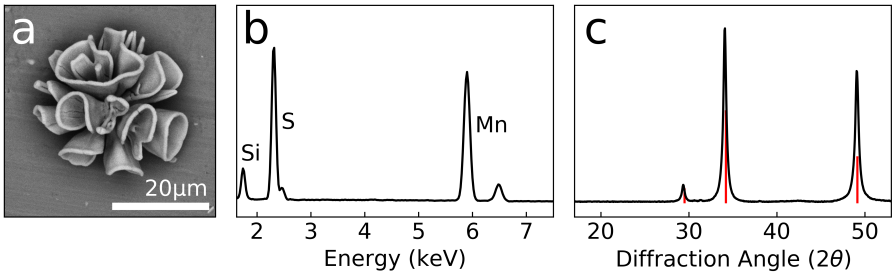


**Figure A.9:** **a,** SEM, **b,** EDS and **c,** XRD of $MnS/SiO_2$ architectures, with reference lines depicted in red.

### A.1.4 Conversion to Iron Salt Nanocomposite Architectures

#### Conversion of $BaCO_3/SiO_2$ to green rust/$SiO_2$ architectures

Anhydrous $FeCl_2$ (506 mg, 4 mmol) was dissolved in 50 mL degassed slightly acidic (pH=4.5, using HCl) water under a nitrogen atmosphere (the lowered pH prevents formation of iron oxide-hydroxide). A substrate containing $BaCO_3/SiO_2$ architectures was placed in the $FeCl_2$ solution. After 80 minutes, the architectures on the substrate had changed color from white to green. For the workup, the substrate was washed in two consecutive demineralized water baths followed by an acetone bath. After exposing the green colored architectures to air, they rapidly turned brown. The resulting architectures were characterized with SEM, EDS and XRD (Figure A.10). The used reference for the XRD-diffractogram can be found in the Crystallography Open Database (COD 5000036). EDS confirmed the cation exchange from barium to iron, though XRD showed that an amorphous material had formed. To further analyze the nanocomposite architectures, IR-spectroscopy was performed, using a Bruker Vertex 80v FT-IR spectrometer equipped with an ATR module (Platinum ATR Diamond) by first measuring a background for 30 minutes and then measuring the converted nanocomposite architectures for 30 minutes. This confirmed the presence of a carbonate anion because as its fingerprint peak at $\sim 1450$ cm$^{-1}$ is visible and the presence of OH bonds because of the OH-bend shown at $\sim 3450$ cm$^{-1}$. The presence of a large peak at $\sim 1700$ cm$^{-1}$ (OH-stretch in $H_2O$) showed that these nanocomposites contain significant amounts of water, contrary to the basic nickel carbonate nanocomposites (Appendix Section A.1.5). Based on these results and the fact that the nanocomposites rapidly decomposed when exposed to air, we expect that green rust ($[Fe_4^{2+}Fe_2^{3+}(OH^-)_{12}]^{2+} \cdot [[CO_3^{2-} \cdot 2H_2O]^{2-}$) is formed during the cation exchange from barium to iron. Furthermore, similar IR-spectra for this material can be found in literature (Legrand, Mazerolles, Chaussé, *GCA*, **2004**, 68, 17, 3497-3507).

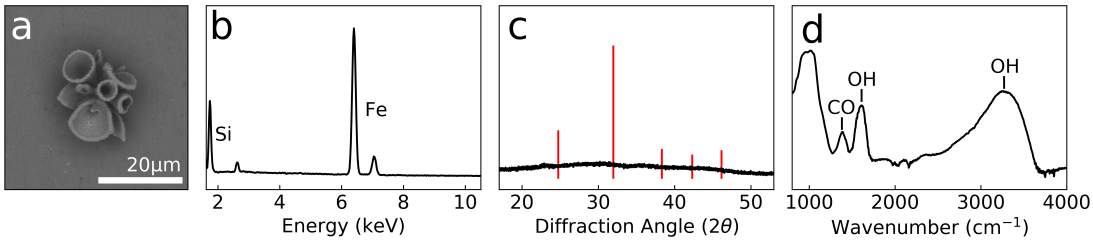


**Figure A.10:** **a,** SEM, **b,** EDS and **c,** XRD of $FeCO_3/SiO_2$ architectures, with the expected $FeCO_3$ reference lines depicted in red. **d** IR spectrum shows the presence of carbonate anions ($\sim 1450$ cm$^{-1}$) and water/hydroxide anions ($\sim 1700$ cm$^{-1}$ and $\sim 3450$ cm$^{-1}$).

### Conversion of green rust/$SiO_2$ to $Fe_3O_4$/$SiO_2$ architectures

A substrate containing green rust/$SiO_2$ architectures was placed in a single zone tube furnace and the architectures were decomposed to $Fe_3O_4$/$SiO_2$ by heating them to 570 °C for 4 hours in a $N_2$ atmosphere. Afterwards the furnace was cooled back to room temperature. The resulting architectures were characterized by SEM, EDS and XRD (Figure A.11), confirming the formation $Fe_3O_4$. The used reference for the XRD-diffractogram can be found in the American Mineralogist Crystal Structure Database (AMCSD 0002400).

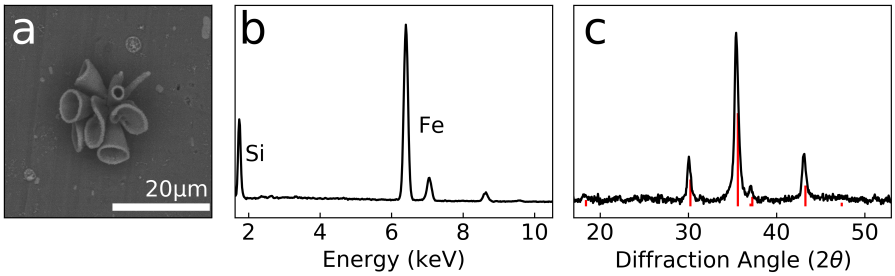


**Figure A.11:** **a,** SEM, **b,** EDS and **c,** XRD of $Fe_3O_4$/$SiO_2$ architectures, with reference lines depicted in red.

### Conversion of green rust/$SiO_2$ to $\alpha$-$Fe_2O_3$/$SiO_2$ architectures

A substrate containing green rust/$SiO_2$ architectures was placed in a single zone tube furnace and the architectures were decomposed to $\alpha$-$Fe_2O_3$/$SiO_2$ by heating them to 570 °C for 4 hours while leaving the tube open to air. Afterwards the furnace was cooled back to room temperature and the resulting architectures were characterized by SEM, EDS and XRD (Figure A.12), confirming the formation of $\alpha$-$Fe_2O_3$. The used reference for the XRD-diffractogram can be found in the American Mineralogist Crystal Structure Database (AMCSD 000143).

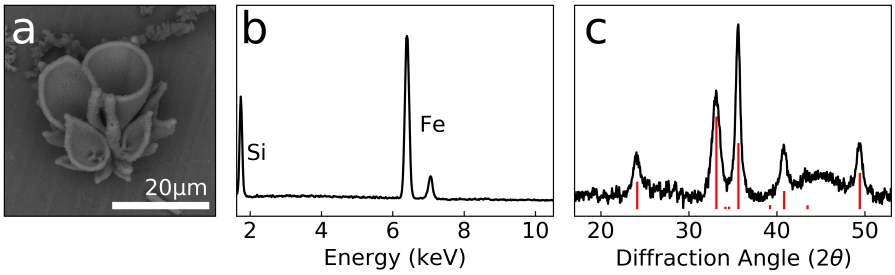


**Figure A.12:** **a,** SEM, **b,** EDS and **c,** XRD of $\alpha$-$Fe_2O_3$/$SiO_2$ architectures, with reference lines depicted in red.

### Conversion of green rust/$SiO_2$ to metallic $\delta$-Fe/$SiO_2$ architectures

A substrate containing green rust/$SiO_2$ architectures was placed in a single zone tube furnace and allowed to decompose to $\delta$-Fe by heating it to 450 °C for 4 hours in a $N_2$ atmosphere with 5 vol% $H_2$. Afterwards the flow of $H_2$ was stopped and the furnace was cooled back to room temperature. The resulting architectures were characterized by SEM, EDS and XRD (Figure A.13), confirming the formation of metallic $\delta$-Fe. The used reference for the XRD-diffractogram can be found in the American Mineralogist Crystal Structure Database (AMCSD 000670).

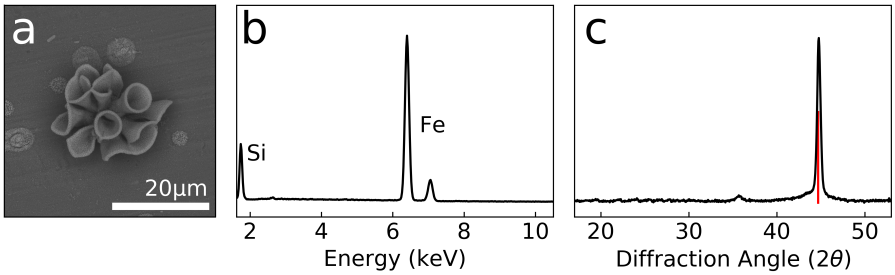


**Figure A.13:** **a,** SEM, **b,** EDS and **c,** XRD of $\delta$-Fe/$SiO_2$ architectures, with reference lines depicted in red.

### A.1.5 Conversion to Nickel Salt Nanocomposite Architectures

#### Conversion of $BaCO_3/SiO_2$ to basic $NiCO_3/SiO_2$ architectures

*With Substrate:* Anhydrous $NiCl_2$ (324 mg, 2,5 mmol) or $NiNO_3$ hexahydrate (727 mg, 2.5 mmol) was dissolved in 50 mL degassed water. A substrate containing freshly made $BaCO_3/SiO_2$ architectures was placed in this solution for 30 minutes. The resulting architectures were washed in two demineralized water baths followed by an acetone bath. The nanocomposite architectures were then characterized with SEM, EDS and XRD (Figure A.14). The used reference for the XRD-diffractogram can be found in the American Mineralogist Crystal Structure Database (AMCSD 0000105). EDS confirmed that the cation exchange from barium to nickel was successful, but the XRD pattern did not match the $NiCO_3$ pattern found in the database. To further analyze the composition of the newly formed salt, IR-spectroscopy was performed as described for the green rust/$SiO_2$ architectures (Appendix Section A.1.4). The peak around $\sim 1450$ $cm^{-1}$ confirmed the presence of a carbonate anion. A broad peak at $\sim 3450$ $cm^{-1}$ was observed, which indicates hydrogen bonded hydroxyl groups, while the absence of peaks around $\sim 3800$ $cm^{-1}$ indicates no unbound hydroxide groups are present. Furthermore the absence of a large peak at $\sim 1645$ $cm^{-1}$ omits the possibility of large amounts of water present in the sample. We believe basic $NiCO_3$ was formed, as the peaks described here match the ones found in literature for basic $NiCO_3$ (Packter and Uppaladinni, *Kristall und Technik*, **1975**, 10, 9, 985-994).

*Without Substrate:* Anhydrous $NiCl_2$ (2,5 g, 0,12 mol) was dissolved in 50 mL degassed water. Freshly made $BaCO_3/SiO_2$ architectures were placed in this solution for 90 minutes while stirring vigorously. The resulting architectures were washed in two demineralized water baths followed by an acetone bath.

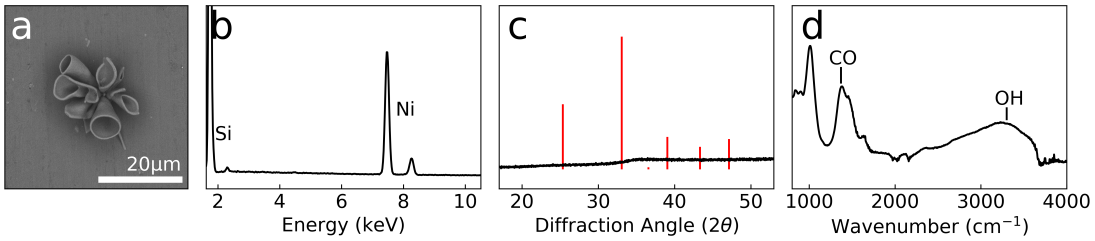


**Figure A.14:** **a,** SEM, **b,** EDS and **c,** XRD of basic $NiCO_3/SiO_2$ architectures, with reference lines of the expected $NiCO_3$ diffraction pattern depicted in red. **d,** IR spectrum showing the presence of peaks corresponding to carbonate anions ($\sim 1450$ $cm^{-1}$) and hydroxide anions ($\sim 3450$ $cm^{-1}$).

### Conversion of Basic $NiCO_3/SiO_2$ to $NiO/SiO_2$ architectures

A substrate with basic $NiCO_3/SiO_2$ architectures obtained as described on the previous page was placed in a single zone tube furnace under nitrogen atmosphere at atmospheric pressure. The tube furnace was heated to 675 °C for 3 hours and subsequently heated to 900 °C for 1.5 hours before allowing it to cool down to room temperature. The resulting architectures were characterized with SEM, EDS and XRD (Figure A.15), confirming the formation of NiO. The used reference for the XRD-diffractogram can be found in the Crystallography Open Database (COD 1010093).

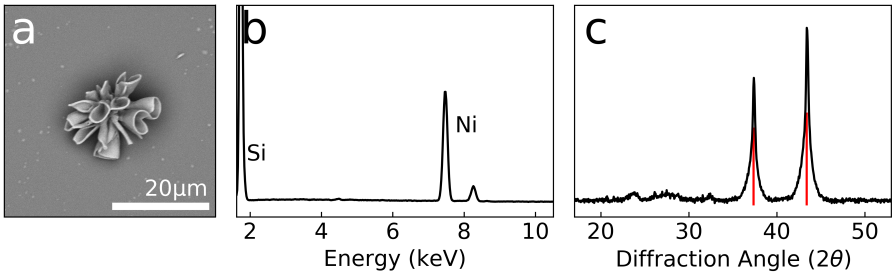


**Figure A.15:** **a,** SEM, **b,** EDS and **c,** XRD of $NiO/SiO_2$ architectures, with reference lines depicted in red.

### A.1.6 Conversion to Cobalt Salt Nanocomposite Architectures

#### Conversion of $BaCO_3/SiO_2$ to basic $CoCO_3/SiO_2$ architectures

Cobalt nitrate hexahydrate ($Co(NO_3)_2$) (727 mg, 2.50 mmol) was dissolved in 50 mL degassed water. A substrate containing $BaCO_3/SiO_2$ architectures was placed in the resulting solution for 50 minutes. The substrate, now containing pink architectures, was removed and washed in two demineralized water baths followed by an acetone bath. Full conversion was determined with EDX analysis , while SEM confirmed perseverance of the shape (Figure A.16). XRD showed amorphous material had formed, rather than the expected $CoCO_3$ crystal structure found in the Crystallography Open Database (COD 1548825). IR-spectroscopy confirmed that indeed an amorphous carbonate had formed, as the presence of a carbonate anion was confirmed with the fingerprint peak at 1450 $cm^{-1}$. Furthermore, a broad peak at 3450 $cm^{-1}$ was observed, which indicates hydrogen bonded hydroxyl groups, while the absence of peaks around 3800 $cm^{-1}$ indicates no unbound hydroxide groups are present. Furthermore, the absence of a large peak at 1645 $cm^{-1}$ omits the possibility of large amounts of water present in the sample. These observations lead to the conclusion that basic cobalt carbonate has formed, especially as the observed spectrum is in good agreement with the IR spectra of basic $CoCO_3$ found in literature (Nassar and Ahmed, *Polyhedron*, **2011**, 30, 2431-2437).

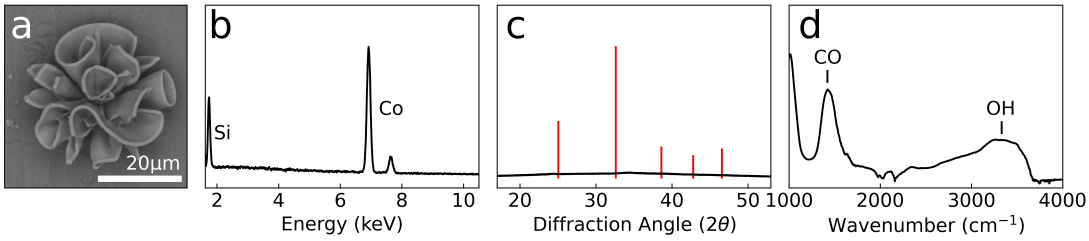


**Figure A.16:** **a,** SEM, **b,** EDS and **c,** XRD of basic $CoCO_3/SiO_2$ architectures, with reference lines of the expected $CoCO_3$ diffraction pattern depicted in red. and **d,** IR spectrum showing the presence of peaks corresponding to carbonate anions ($\sim$ 1450 $cm^{-1}$) and hydroxide anions ($\sim$ 3450 $cm^{-1}$).

### Conversion of basic $CoCO_3/SiO_2$ to $CoO/SiO_2$ architectures

Basic $CoCO_3/SiO_2$ architectures were placed in a single zone tube furnace with nitrogen atmosphere and heated to 350 °C for 4 hours followed by heating it to 530 °C for 3 hours. The resulting $CoO/SiO_2$ architectures were analyzed by SEM, EDS and XRD (Figure A.17). The crystalline part was determined to be composed of $Co_3O_4$ by comparing the XRD pattern with a reference from the Inorganic Crystal Structure Database (ICSD 9865).

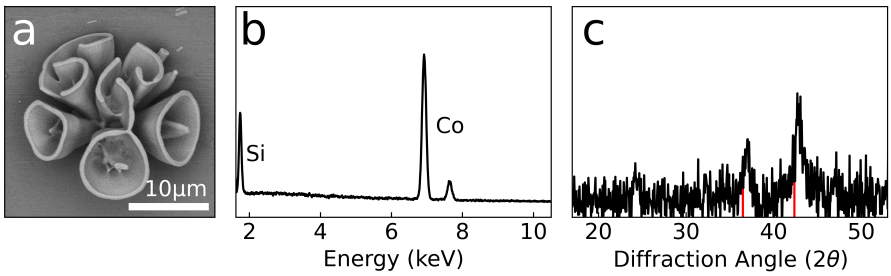


**Figure A.17:** **a,** SEM, **b,** EDS and **c,** XRD of $CoO/SiO_2$ architectures, with reference lines depicted in red.

### Conversion of basic $CoCO_3/SiO_2$ to $Co_3O_4/SiO_2$ architectures

Basic $CoCO_3/SiO_2$ architectures were placed in an open single zone tube furnace and heated to 650 °C for 4 hours to obtain nanocomposites with a grain size of ca. 17 nm. Changing this elevated temperature results in different crystal sizes, with exclusively heating to temperatures of 530, 560, 590 and 620 °C for 4 hours resulting in crystal sizes of ca. 10, 12, 14, and 15 nm respectively (see Appendix A.2.6). The resulting black nanocomposites were determined to be composed of $Co_3O_4$ by XRD, with preservation of microshape and metal to silicon ratio of 4:1 as shown by SEM and EDS respectively (Figure A.18). The used reference for the XRD-diffractogram can be found in the Inorganic Crystal Structure Database (ICSD 27498).

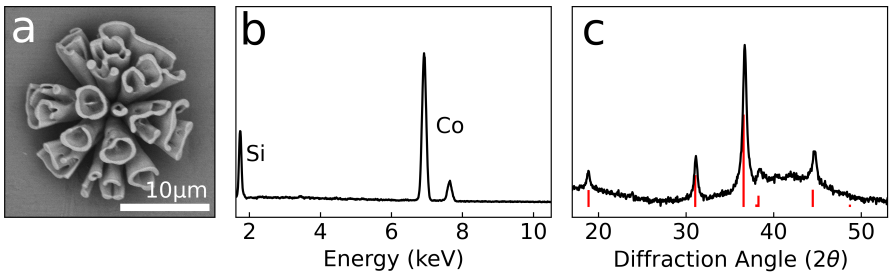


**Figure A.18:** **a,** SEM, **b,** EDS and **c,** XRD of $Co_3O_4/SiO_2$ architectures, with reference lines depicted in red.

### A.1.7 Conversion to Lead Salt Nanocomposite Architectures

#### Conversion of $BaCO_3/SiO_2$ to $PbCO_3/SiO_2$ architectures

Inside an airtight jar with a magnetic stirring bar, 15 g of $Pb(NO_3)_2$ was dissolved in 50 ml of degassed water. The reaction jar was kept under an inert atmosphere by applying a continuous flow of nitrogen via two tubes that were inserted through the cap of the airtight jar. After the $Pb(NO_3)_2$ was completely dissolved (ca. 15 minutes), sample slides containing previously prepared $BaCO_3/SiO_2$ architectures were inserted in the solution for 30-60 seconds. Afterwards the sample slides were washed with deionized water and acetone and carefully dried in air. The resulting $PbCO_3/SiO_2$ architectures were characterized with SEM, EDS and XRD (Figure A.19).

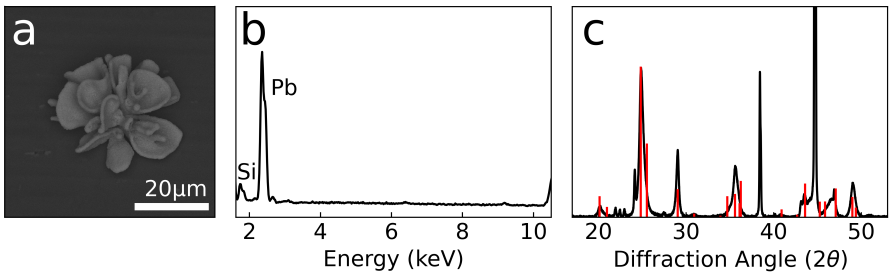


**Figure A.19:** **a,** SEM, **b,** EDS and **c,** XRD of $PbCO_3/SiO_2$ architectures, with reference lines depicted in red. The peaks at $\sim 38$ ° and $\sim 45$ ° are caused by the aluminum background.

### Conversion of $PbCO_3/SiO_2$ to $PbI_2/SiO_2$ architectures

An acidic aqueous solution was prepared by adding 17 µL of $HNO_3$ (70% in $H_2O$) to 50 mL of deionized water. 150 mg KI was added to 10 mL of this acidic aqueous solution. This solution was then used to convert one sample from $PbCO_3$ to $PbI_2$ by dipping the sample in for 45 seconds under ambient conditions. For each consecutive conversion, a new solution was made for each individual conversion. Afterwards the sample slides were washed with deionized water and acetone and carefully dried in air. The resulting $PbI_2/SiO_2$ architectures were characterized with SEM and EDS (Figure A.20).

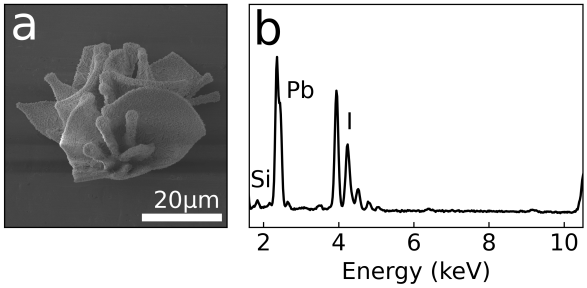


**Figure A.20:** **a,** SEM and **b,** EDS of $PbI_2/SiO_2$ architectures.

### Conversion of $PbCO_3/SiO_2$ or $SrCO_3/SiO_2$ to $CH_3NH_3PbX_3/SiO_2$ architectures

$PbCO_3/SiO_2$ architectures were placed in the middle of a single zone horizontal tube furnace. Subsequently an alumina boat containing methyl ammonium halide (chlorine, bromine or iodine) was placed at the edge of the tube furnace in the cold zone. The pressure inside the tube was lowered to below 0.1 mbar using a vacuum pump. The tube was then flushed with argon until atmospheric pressure was reached. This process was repeated twice to purge the system of oxygen. Afterwards the temperature of the furnace was set to 120 °C and a 30 sccm flow of argon was applied to increase the pressure to 70 mbar. The boat was moved directly next to the $PbCO_3/SiO_2$ architectures in the middle of the oven. After 6 hours the reaction was stopped by opening the oven. XRD, EDS and PL measurements confirmed the formation of a lead halide perovskite (see Figure A.21).

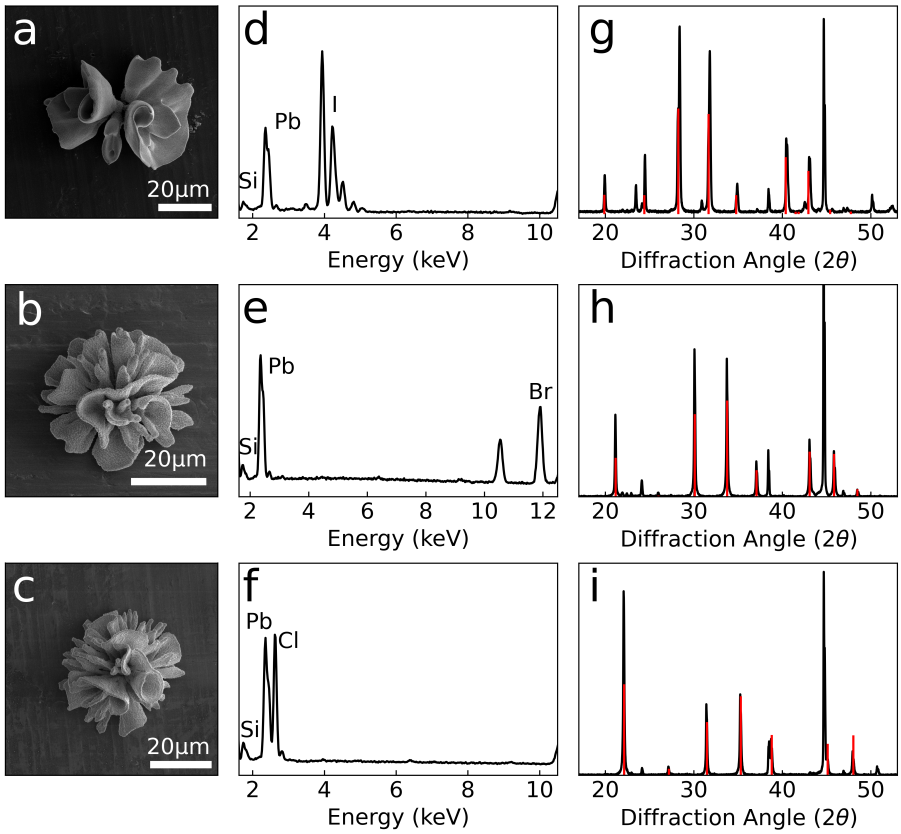


**Figure A.21:** **a-c,** SEM, **d-f,** EDS and **g-i,** XRD of $CH_3NH_3PbI_3/SiO_2$ (top), $CH_3NH_3PbBr_3$ /$SiO_2$ (middle) and $CH_3NH_3PbCl_3/SiO_2$ (bottom) architectures, with reference lines depicted in red. The peaks at $\sim 38$ ° and $\sim 45$ ° are caused by the aluminum background.

**Preparation and conversion of $CaCO_3$ biomineralized structures to lead perovskite**

Sand dollars shells and cuttlefish bones are biominerals composed of $CaCO_3$ crystals that can be converted to $PbCO_3$ following the procedure described for the conversion of the nanocomposite architectures. To facilitate the conversion of the cuttlefish bone, its organic tissue was first removed with bleach, while the sand dollar shells were not bleached. For bleaching, slices of cuttlefish bone were infiltrated with acetone at lowered pressure (250 mbar) for one hour. To remove the acetone, the cuttlefish bone was transferred to water and stored under 250 mbar for 1 hour. The cuttlefish bone then was bleached in 0.5M KOH for 10 days. Immersing the sample in deionized water stopped the bleaching process and the KOH was allowed to diffuse out of the sample for 24 hours. After this, the samples were placed in acetone for 24 hours to replace the water in the structure, and dried at ambient atmosphere. Prior to the conversion to $PbCO_3$, both the cuttlefish bone and sand dollar shell were again infiltrated with acetone. For the conversion 15 g $Pb(NO_3)_2$ was dissolved in 50 ml of degassed, deionized water (0.9M) under $N_2$ atmosphere. The infiltrated samples were placed in the $Pb(NO_3)_2$ solution at lowered pressure to infiltrate them completely with the aqueous solution. The exchange reaction was allowed to continue for 120 minutes. Immersing the biominerals in deionized water for 24 hours stopped the conversion reaction and removed the $Pb(NO_3)_2$. Finally, the samples were transferred to acetone for 1 hour and dried at lowered pressure for 20 minutes. The conversion to $CH_3NH_3PbX_3$ follows the same route as for the nanocomposite architectures, but due to the large sample size the reaction time was increased to 24 hours instead of 6 hours.

The exchange reaction to $CH_3NH_3PbX_3$ can also be performed in a liquid phase. This circumvents the size limitations given by the diameter of the reaction tube in the furnace. To convert a large piece of cuttlefish bone, 500 mg of methyl ammonium bromide was dissolved in 50g of isopropanol. Similar to the previous steps the cuttlefish bone got infused with isopropanol at lowered pressure and then transferred to the prepared solution of methyl ammonium bromide. To allow diffusion of methyl ammonium bromide into the structure the sample was left in the solution for 24h. To convert the surface of a sand dollar a solution of 25 mg methyl ammonium bromide in 2.5 g of isopropanol was prepared. The solution was then applied onto the sand dollar shell using a Pasteur pipet. When the conversion reaction was performed under UV radiation, the formation of the perovskite can be observed in real-time. The initially white sand dollar turns light orange in daylight and fluoresces bright green under UV irradiation (Figure A.22).

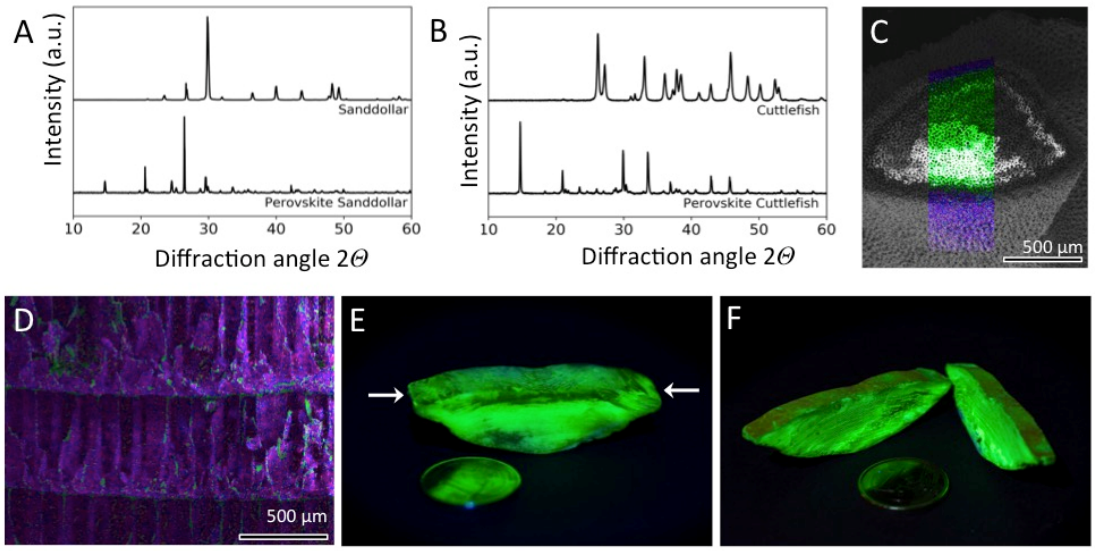


**Figure A.22: Conversion of biominerals to lead halide perovskites.** **A,** X-ray powder diffraction data showing the conversion of biomineralized $CaCO_3$ (aragonite) of a cuttlefish bone into $CH_3NH_3PbBr_3$. **B,** X-ray powder diffration showing the conversion of biomineralized $CaCO_3$ (calcite) of a sand dollar shell into $CH_3NH_3PbBr_3$. **C,** EDS map of a cross-section of a sand dollar shell showing partial conversion of $CaCO_3$ into the $CH_3NH_3PbBr_3$, leading to a core-shell structure with semiconducting perovskite enveloping the insulating $CaCO_3$ (green: calcium, blue: lead and purple: bromine). **D,** EDS map of a cross-section of a cuttlefish bone showing almost complete conversion (same color code as in C). **E,** Slice of a cuttlefish bone (6.5x1.5x1.7mm, 1 euro coin for scale) converted to $CH_3NH_3PbBr_3$ showing photoluminescence under UV illumination. **F,** Cross section of the sample shown in E cut along the long axis indicated by arrows, showing conversion throughout the interior.

### A.1.8 Conversion to Tin Salt Nanocomposite Architectures

#### Conversion of $BaCO_3/SiO_2$ to $Sn_3(OH)_2O_2/SiO_2$ architectures

Anhydrous $SnCl_2$ (948 mg, 100 mM) was dissolved in 50 mL degassed water. Subsequently a substrate with $BaCO_3/SiO_2$ architectures was placed in the solution for 30 seconds. The resulting $Sn_3(OH)_2O_2$ /$SiO_2$ architectures were washed in two demineralized water baths followed by an acetone bath. After drying to the air, the architectures were analyzed using SEM, XRD and EDS (Figure A.23). The used reference for the XRD-diffractogram can be found in the Crystallography Open Database (COD 9011384). Furthermore, to confirm the replacement of the carbonate anion with an hydroxide anion, IR was performed which confirmed both the presence of hydroxide anions (3350 $cm^{-1}$) and the absence of the carbonate anion (absence of the fingerprint peak at 1400 $cm^{-1}$).

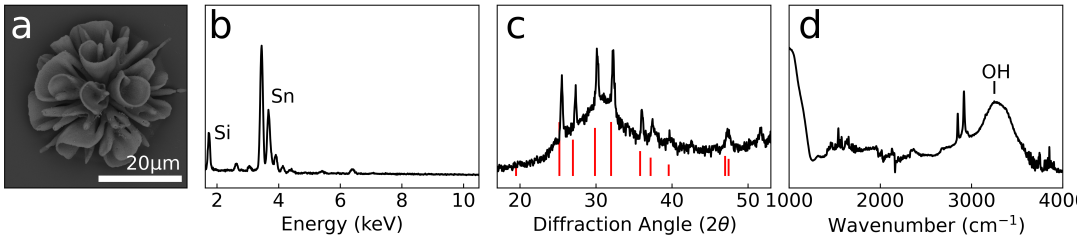


**Figure A.23:** **a,** SEM, **b,** EDS, **c,** XRD and **d,** IR of basic $Sn_3(OH)_2O_2/SiO_2$ architectures, with reference lines of the diffraction pattern depicted in red. IR spectra shows the absence of carbonate anions as the fingerprint peak ($\sim$ 1400 $cm^{-1}$) is missing, while a new peak indicating hydroxide anions has formed ($\sim$ 3350 $cm^{-1}$).

### Conversion of $Sn_3(OH)_2O_2/SiO_2$ to $SnO_2/SiO_2$ architectures

A substrate containing $Sn_3(OH)_2O_2/SiO_2$ architectures was placed in the middle of a single zone horizontal tube furnace. The oven was heated to 200 °C for 3 hours and was subsequently heated to 600 °C for 3 hours to convert the nanocomposite architectures to $SnO_2$. SEM, EDS and XRD analysis was performed, where XRD confirmed formation of $SnO_2$ (A.24, reference used for XRD measurements is COD 1534785).

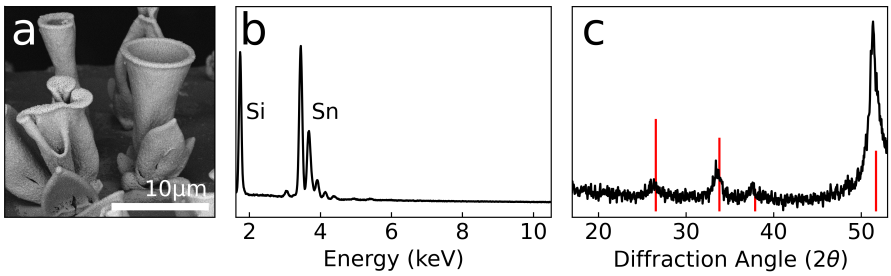


**Figure A.24:** **a,** SEM, **b,** EDS and **c,** XRD of $SnO_2/SiO_2$ architectures, with reference lines depicted in red.

### Conversion of $Sn_3(OH)_2O_2/SiO_2$ to $CH_3NH_3SnX_3/SiO_2$ architectures

A substrate containing $Sn_3(OH)_2O_2/SiO_2$ architectures was placed in the middle of a single zone horizontal tube furnace. Subsequently an alumina boat containing methyl ammonium halide (bromine or iodine) was placed next to the substrate. The pressure inside the tube was lowered to below 0.1 mbar using a vacuum pump. The tube was then flushed with nitrogen until atmospheric pressure was reached. This process was repeated twice to purge the system of oxygen. Afterwards the temperature of the furnace was set to 120 °C and a 30 sccm flow of nitrogen was applied to increase the pressure to 70 mbar. After 30 minutes the reaction was stopped and the oven was passively cooled to room temperature. XRD, EDS and PL measurements confirmed the formation of a tin halide perovskite (Figure A.25, references used for the XRD measurements are COD 2104791 and 4335632 for bromide and iodide perovskite respectively).

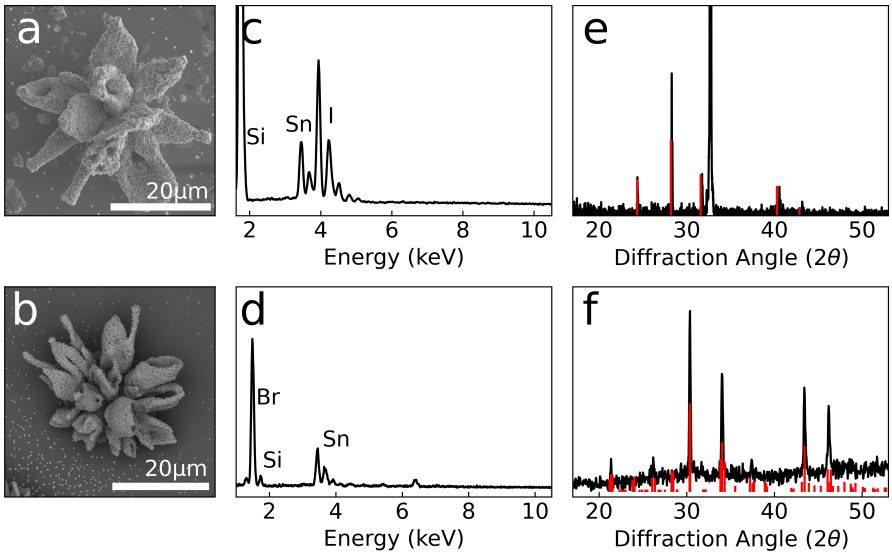


**Figure A.25:** **a,b,** SEM, **c,d,** EDS and **e,f,** XRD of $CH_3NH_3SnI_3/SiO_2$ (top) and $CH_3NH_3SnBr_3$ $/SiO_2$ (bottom) architectures, with reference lines depicted in red.

## A.2 Composition Analysis Equipment and Methods

### A.2.1 Scanning Electron Microscopy (SEM) and Energy-dispersive X-ray Spectroscopy (EDS) Characterization

Samples were loaded into the SEM without applying a conductive metal coating. SEM images were obtained using a FEI Verios 460 equipped with an Everhart-Thornley detector (ETD) and a circular backscatter detector (CBS). The images were recorded between 5 and 10 kV using a 100 pA current in all instances. EDS was measured with the same electron microscope using an Oxford X−Max$^n$ energy dispersive X-ray spectrometer with an accelerating voltage of 20 to 30 kV using a 100 pA current.

### A.2.2 Infrared Spectrometry (IR) Characterization

IR spectra were recorded using a Bruker Vertex 80v FT-IR spectrometer equipped with an ATR module (Platinum ATR Diamond) by first measuring a background after 30 minutes to flush water vapor and $CO_2$ out and then measuring the converted nanocomposites after a similar 30 minutes wait time.

### A.2.3 Transmission Electron Microscopy (TEM) Characterization

TEM samples were prepared through focused ion beam (FIB) milling (FEI Helios 600 NanoLab Dual Beam). Nanocomposite architectures of interest were first identified with SEM imaging. Typically, vase- or leaf-like architectures were chosen due to their relatively flat geometry. The architectures were first coated with a platinum protective layer (thickness, $\sim 1$ µm). They were then attached to a micromanipulator (OMNIProbe) and transferred to a TEM copper grid inside the Dual Beam electron microscope. The specimens were then sequentially thinned by FIB at 30, 16, 5, and 2 kV ion beam voltages in order to reach electron transparency. As the structural non-flatness is inevitable, the thinning area was kept narrow typically compared to the total size of the specimens. Imaging techniques such as bright-field, high-resolution TEM imaging, SAED were acquired by using a JEOL 2100 operated at 120 kV and 200kV and a field emission JEOL 2100 at 200 kV. Intensity profiles of diffraction peaks in SAED patterns were obtained by the azimuthal and radial integration of the patterns using customized MATLAB codes. The azimuthal integration of the diffraction peaks was further analyzed with OriginLab for peak identification and quantification of misorientation (Figure 2.2). The radial integration of the SAED pattern in combination with standard diffraction data was used to label the diffraction peaks.

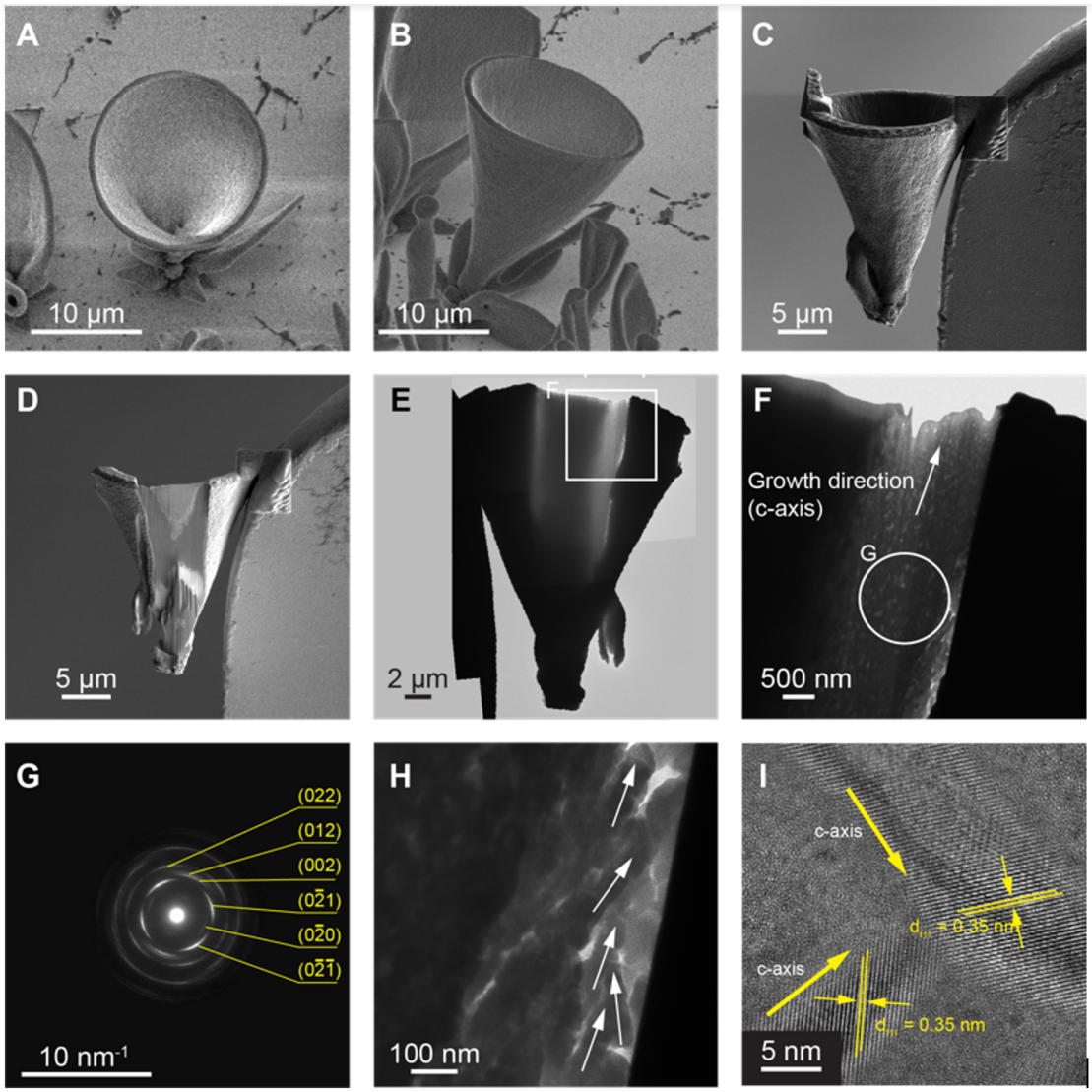


**Figure A.26: Structural analysis of $BaCO_3/SiO_2$ nanocomposites. A,** Top-view and **B,** side-view SEM images of the original vase-like $BaCO_3/SiO_2$ nanocomposite used for TEM sample preparation. **C,** SEM image of the nanocomposite attached to a copper TEM grid by using an OMNIProbe. **D,** SEM and **E,** TEM Images of the sample after thinning. **F,** TEM image of the thinned region close to the top of the structure. The growth direction is indicated by the arrow, which is aligned with the c-axis of $BaCO_3$. **G,** A SAED pattern labeled with the orthorhombic phase of $BaCO_3$. The region used to acquire this SAED pattern is shown in F. **H,** A TEM image revealing rod-like structures (highlighted by white arrows). **I,** A high-resolution TEM (HRTEM) image showing the individual rod-like $BaCO_3$ crystals embedded in the amorphous silica matrix.

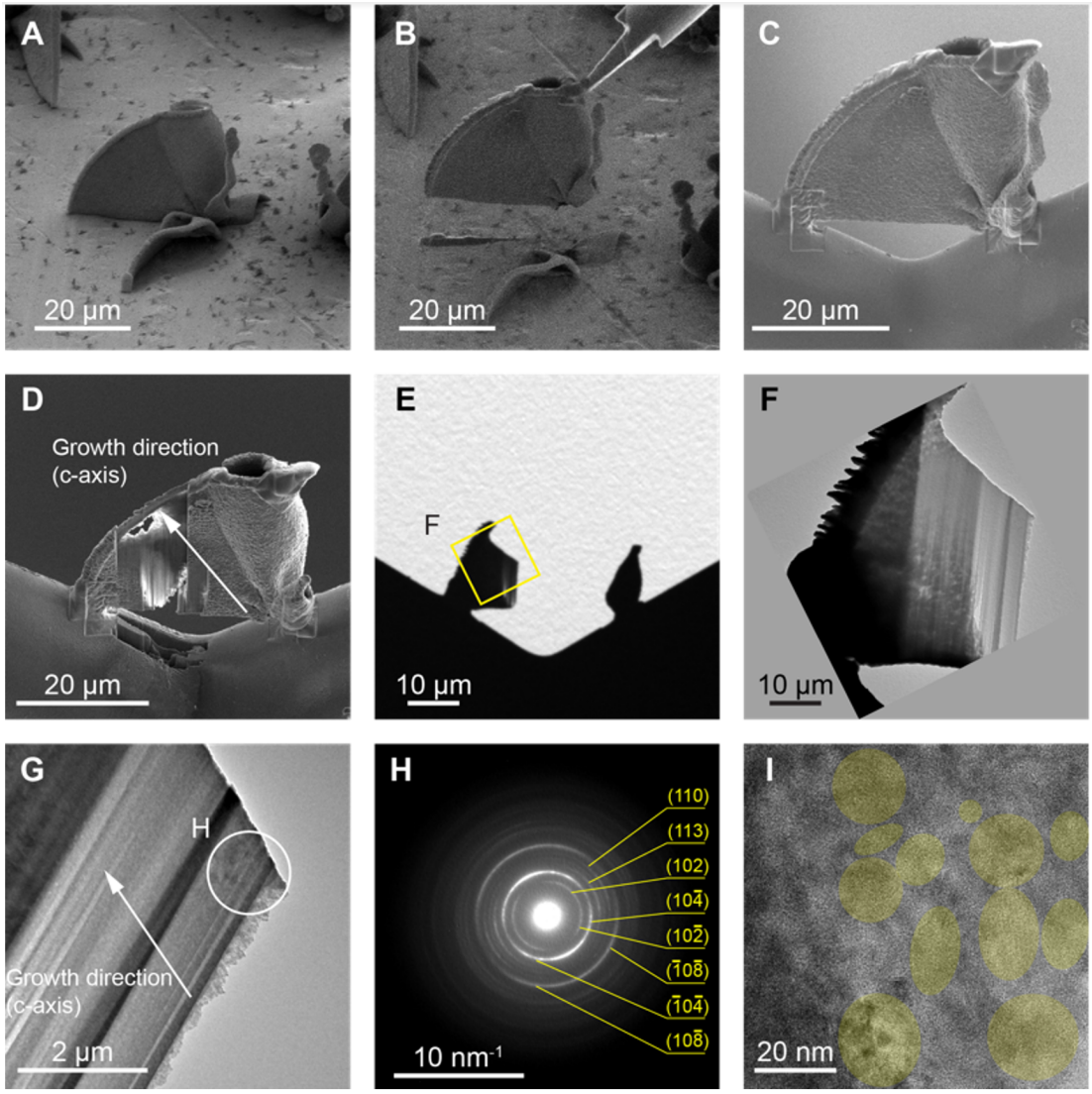


**Figure A.27: Structural analysis of $CdCO_3/SiO_2$ nanocomposites. A,** Side-view SEM images of the original $CdCO_3SiO_2$ nanocomposite and **B,** the nanocomposite attached to an AMNIProbe used for TEM sample preparation. **C,** SEM image of the structure attached to a copper TEM grid by using the OMNIProbe. **D,** SEM and **E,F,** TEM images of the sample after thinning. The growth direction is indicated by the arrow, which is aligned with the c-axis of $CdCO_3$. **G,** TEM image of the thinned region close to the top of the structure. **H,** A SAED pattern labeled with the trigonal phase of $CdCO_3$. The region used to acquire this SAED pattern is shown in G. **I,** A HRTEM image showing the $CdCO_3$ crystals embedded in the amorphous silica matrix. The crystalline regions are highlighted with a yellow color.

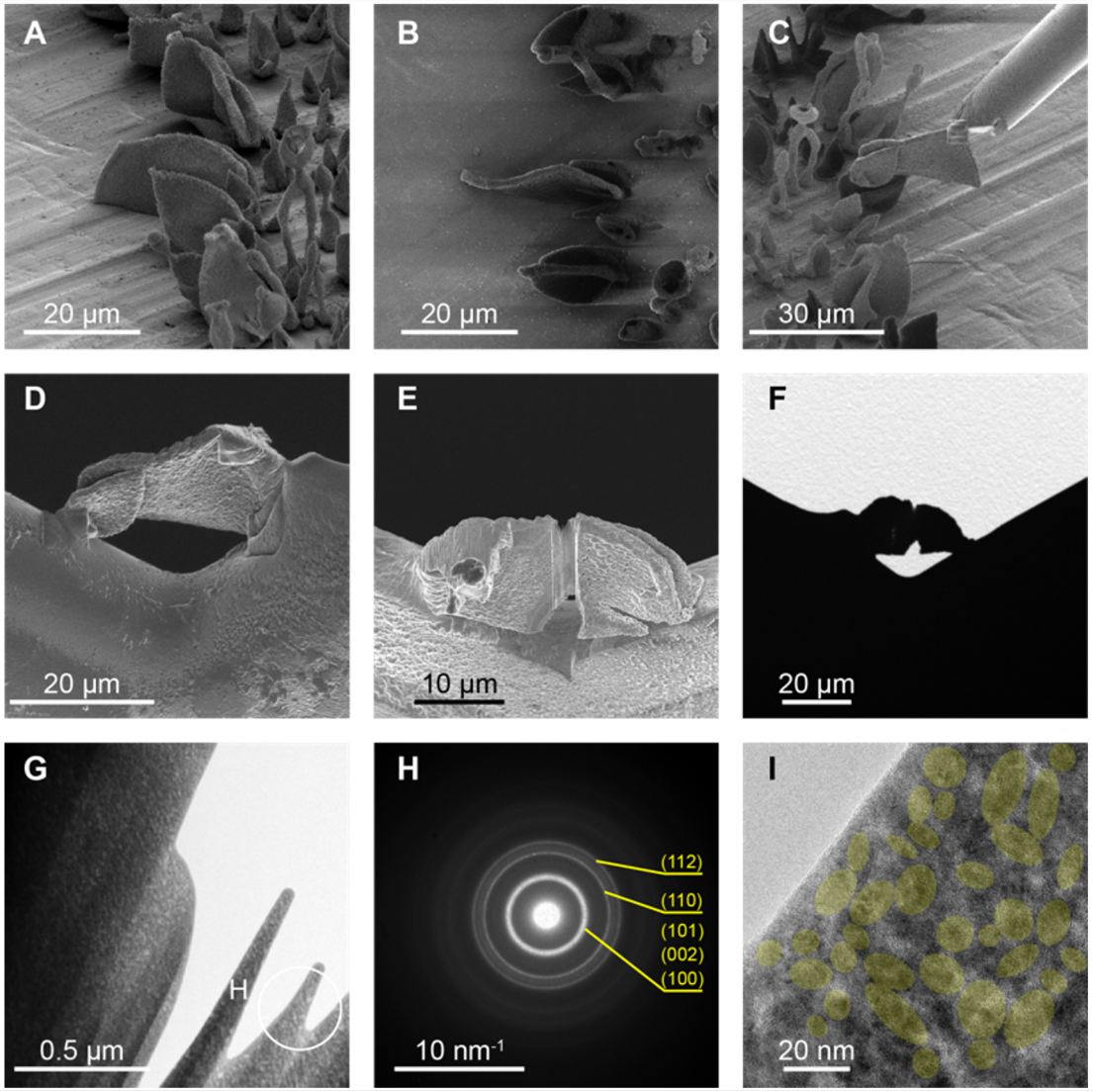


**Figure A.28: Structural analysis of $CdS/SiO_2$ nanocomposites. A,** Side-view and **B,** top-view SEM images of the original $CdS/SiO_2$ nanocomposite used for TEM sample preparation. **C,** SEM image of the structure picked up by an OMNIProbe. SEM images of the structure attached to a TEM copper grid **D,** before and **E,** after FIB thinning. **F,** TEM overview image of the sample. **G,** TEM image of the thinned region at the tip of the structure. **H,** A SAED pattern labeled with the CdS crystal structure, showing its polycrystalline nature with no preferred crystal alignment. The region used to acquire this SAED pattern is shown in G. **I,** A HRTEM image showing the CdS crystals embedded in the amorphous silica matrix. The crystals are highlighted with a yellow color.

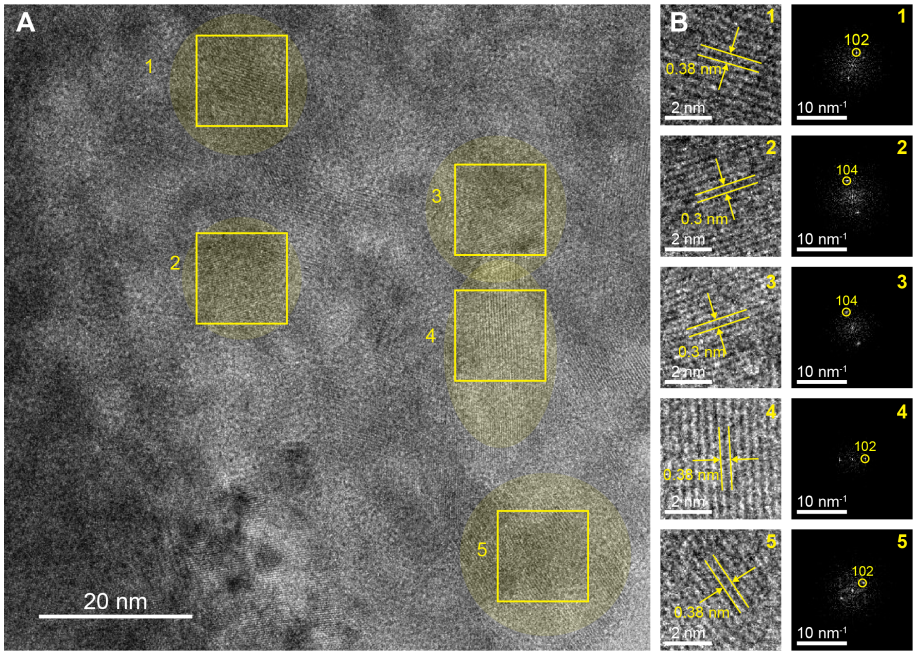


**Figure A.29: HRTEM imaging analysis of $CdCO_3/SiO_2$ nanocomposites.** **A,** Original HRTEM image with regions of interest highlighted in yellow. **B,** The images in the left column show the magnified view of the regions of interest with prominent lattice spacings highlighted. The images in the right column show the corresponding FFT patterns.

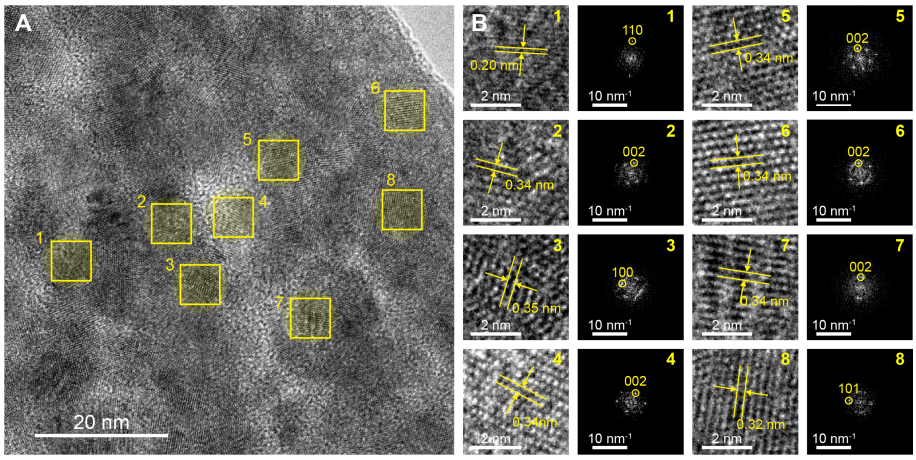


**Figure A.30: HRTEM imaging analysis of $CdS/SiO_2$ nanocomposites.** **A,** Original HRTEM image with regions of interest highlighted in yellow. **B,** The images in the first and third column show the magnified view of the regions of interest with prominent lattice spacings highlighted. The images in the second and fourth column show the corresponding FFT patterns.

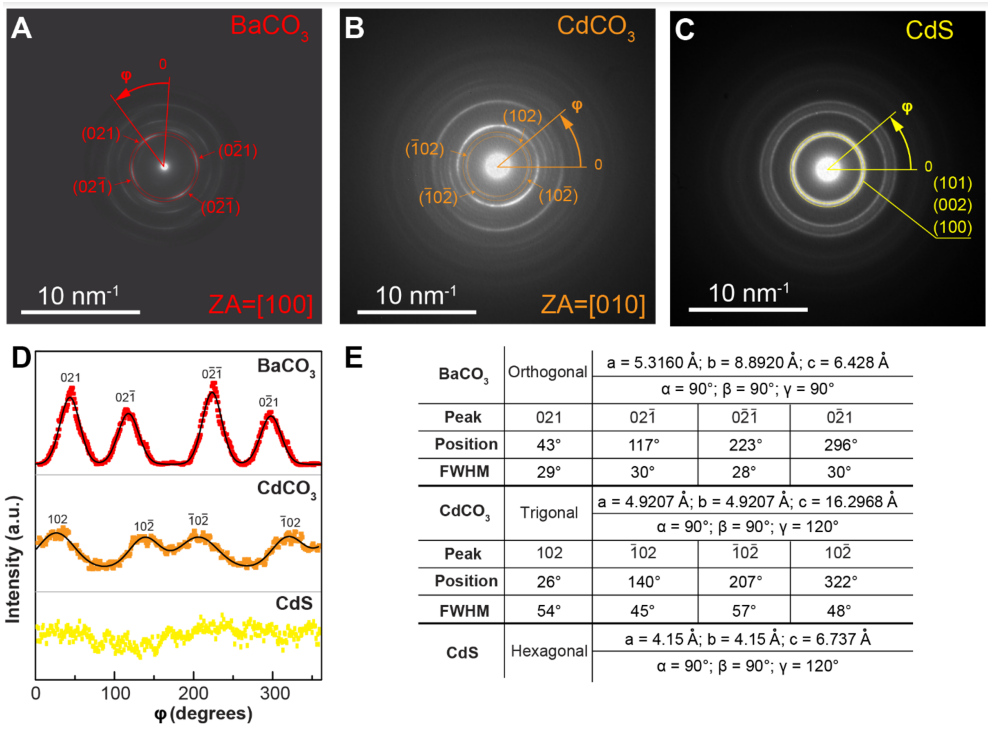


E

| | | | | |
|---|---|---|---|---|
| $BaCO_3$ | Orthogonal | a = 5.3160 Å; b = 8.8920 Å; c = 6.428 Å | | |
| | | α = 90°; β = 90°; γ = 90° | | |
| Peak | 021 | 02$\bar{1}$ | 02$\bar{1}$ | 02$\bar{1}$ |
| Position | 43° | 117° | 223° | 296° |
| FWHM | 29° | 30° | 28° | 30° |
| $CdCO_3$ | Trigonal | a = 4.9207 Å; b = 4.9207 Å; c = 16.2968 Å | | |
| | | α = 90°; β = 90°; γ = 120° | | |
| Peak | 102 | $\bar{1}$02 | $\bar{1}$0$\bar{2}$ | 10$\bar{2}$ |
| Position | 26° | 140° | 207° | 322° |
| FWHM | 54° | 45° | 57° | 48° |
| CdS | Hexagonal | a = 4.15 Å; b = 4.15 Å; c = 6.737 Å | | |
| | | α = 90°; β = 90°; γ = 120° | | |

**Figure A.31: Quantification of crystallographic misorientation.** SAED patterns of **A,** $BaCO_3$, **B,** $CdCO_3$, and **C,** CdS with peaks labeled and highlighted for intensity integration with respect to the azimuthal angle, $\phi$. **D,** Intensity profile of the (02$\bar{1}$)/(02$\bar{1}$)/(02$\bar{1}$)/(021), (10$\bar{2}$)/(102)/($\bar{1}$02)/($\bar{1}$0$\bar{2}$), and (101)/(002)/(100) peaks for $BaCO_3$, $CdCO_3$, and CdS, respectively. **E,** Fitted peak position and corresponding full width at half maximum (FWHM) for each peak for $BaCO_3$ and $CdCO_3$.

### A.2.4 X-ray Diffraction (XRD) Characterization

X-ray diffraction measurements were performed using a Bruker D2 Phaser (Bragg-Brentano geometry) using a K-alpha Cu X-ray source with an emission energy of 8.0415 keV. The samples were mounted inside a chamber filled with ambient air at room temperature. All measurements were performed using a 1.0 mm beam knife to reduce unwanted scattering and optimize the low angle part of the diffractogram. A nickel filter was used to reduce the 20-30% contribution from the k-beta Cu X-ray source. A divergence slit of 0.1 or 1 mm was used to control the illuminated area of the sample, based on the available material. Diffracted X-rays were detected using a Lynxeye detector and were collected for at least 12 hours with a scan interval ($\Delta 2\vartheta$) of 0.01°. Diffractograms were calibrated using reference spectra mentioned in the synthesis of each material. It should be noted that in general nanocomposites grown on the meniscus as described in Section A.1.1 were used for this analysis, rather than nanocomposites grown on a substrate to maximize the signal to noise ratio in the XRD measurement.

### A.2.5 Grain Size Determination from XRD Patterns

The average grain size was determined using the Debye Scherrer Equation (A.1):

$$\tau = \frac{K\lambda}{\beta cos\theta} \tag{A.1}$$

where τ is the mean size of the crystalline domains, K is the shape factor and is estimated to be 0.9, λ is the wavelength of the x-ray source (1.54060 Å), B is the line broadening at half height (fwhm) and ϑ is the Bragg angle. As an example, B and ϑ are determined from an isolated peak in the XRD diffractogram of $CdCO_3$ (Figure A.3). Here B is the line broadening at half height (0.0089 rad) and ϑ is the peak position in radians (0.206 rad). Inserting these values into the equation gives τ=16.05 nm, which was verified using the [2-10] peak, which gives τ=15.32 nm, corresponding well with the crystal size observed with TEM (Figure A.27). A complete list of all the metal oxide and sulfide crystal sizes discussed in Chapter 2 can be found in Table A.1.

| **Crystal** | **Average Grain Size (nm)** |
|---|---|
| $BaCO_3$ | 21 |
| $CdCO_3$ | 16 |
| CdO | 14 |
| CdS | 6 |
| $MnCO_3$ | 16 |
| MnO | 9 |
| $Mn_2O_3$ | 16 |
| $Mn_3O_4$ | 12 |
| MnS | 23 |
| $NiCO_3$* | Amorphous |
| NiO | 21 |
| $FeCO_3$* | Amorphous |
| Fe | 21 |
| $Fe_2O_3$ | 9 |
| $Fe_3O_4$ | 18 |
| $CoCO_3$* | Amorphous |
| $Co_3O_4$** | 10 |

**Table A.1:** Average grains sizes for metal oxide and sulfide crystals discussed in Chapter 2. *:Amorphous Carbonate formed, thus grain size could not be determined from XRD. **:Grain size from decomposition at 530 °C, for other grain sizes see Section A.2.6.

### A.2.6 Temperature Dependent Grain Size Determination

The crystal domain size at various decomposition temperatures T was determined using XRD. The [311] peaks of five $Co_3O_4/SiO_2$ nanocomposites, obtained with the preparation methods described in Experimental Section A.1.6, were measured. Debye-Scherrer theory (A.L. Patterson, *Phys. Rev.*, **1939**, 56, 987-982) relates the crystal domain size $\tau$ to the full width at half maximum (FWHM) $\beta$ of spectral peaks via

$$\tau = \frac{K\lambda}{\beta cos\theta} \tag{A.2}$$

where K is a material-dependent shape factor that is estimated at 0.9 given the material's cubic symmetry (J.I Langford and A.C.J. Wilson, *Journal of Applied Crystallography*, **1978**, 11, 102-113) , $\lambda = 0.154060$nm the incident wavelength, and $\vartheta_p$ the peak angle.

The experimental data (Figure A.32A,B) show a Lorentzian peak (J.I Langford, D.Louër, *Report on Progress in Physics*, **1996**, 59, 131-234) of amplitude $I_{max}$ with a linear offset $2B\varphi + C$, which we fit numerically with the model:

$$I_{max} = \frac{(\frac{\beta}{2})^2}{(\frac{\beta}{2})^2 + (2\phi - 2\theta_p)^2} + 2B\phi + C \tag{A.3}$$

Least-squares fitting via a custom Python script yields estimates for $\vartheta_p$ and $\beta$, as well as their errors in the form of a covariance matrix. Ignoring correlations, the square roots of the matrix' diagonal entries form lower bounds for the standard errors $\Delta\vartheta_p$ and $\Delta\beta$, which yield a minimal standard error

$$\sqrt{(\frac{\Delta\beta}{\beta})^2 + (\Delta\theta_p tan\theta_p)^2\tau} \tag{A.4}$$

on the domain size via established uncertainty propagation methods (Figure A.32C, H.H. Ku, *Journal of research of the national bureau of standards C*, **1966**, 70, 263-273). Reducing the signals' white Gaussian noise level with various filtering methods does not lead to significantly different domain size estimates (Figure A.32D). In the case of the nanocomposites heated to 530 °C, the calculated crystal domain size of $\tau = 9.9 \pm 0.5$nm. The crystal size for the other decomposition temperatures was determined in a similar fashion. Table A.2 summarizes the results, while Figure A.32 shows the used fits and peaks.

| Decomposition Temperature (°C) | Grain Size (nm) |
|---|---|
| 530 | 9.9 ± 0.5 |
| 560 | 12.2 ± 0.3 |
| 590 | 14.4 ± 0.3 |
| 620 | 620 ± 0.4 |
| 650 | 650 ± 0.3 |

**Table A.2:** Obtained $Co_3O_4$ Grain Sizes using different decomposition temperatures.

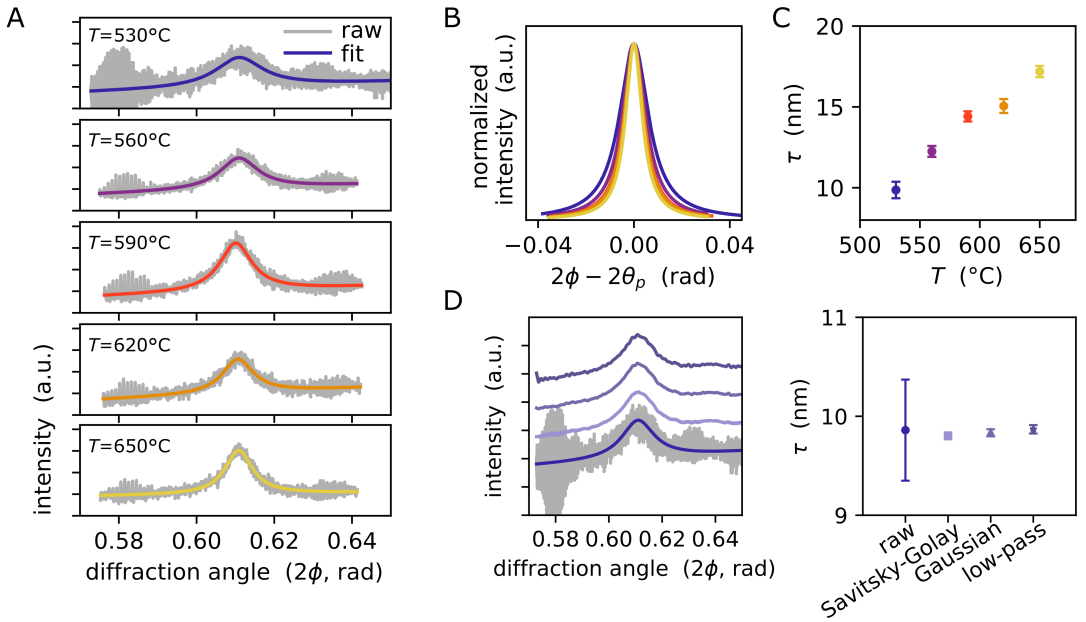


**Figure A.32:** Full width half maximum determination of [311] peak of $Co_3O_4$, heated to **A,** T = 530 to 650°C. Gray lines show the original diffractogram and coloured lines the fit used to determine crystal size. **B,** Overlay of normalized fits obtained in A, with linear offset subtracted. **C,** Grain sizes τ measured at various decomposition temperatures. **D,** Left: noise reduction on raw data (gray line, T = 530°C) with Savitsky-Golay, Gaussian, and low-pass filters (colours; offset added for clarity) do not lead to significantly different fitted grain sizes (right).

### A.2.7 Mechanism of the Conversion to Tin

#### Allowing equilibrium between bulk and local reaction conditions

To demonstrate the importance of the temporal local reaction zone, a substrate with nanocomposites was kept in a conversion solution for 2 minutes. At this time, the $BaCO_3$ has completely dissolved and the local reaction zone has disappeared. Without the locally increased pH, the $Sn_3(OH)_2O_2$ inside the nanocomposites dissolves, leaving behind an empty $SiO_2$ shell (Figure A.33).

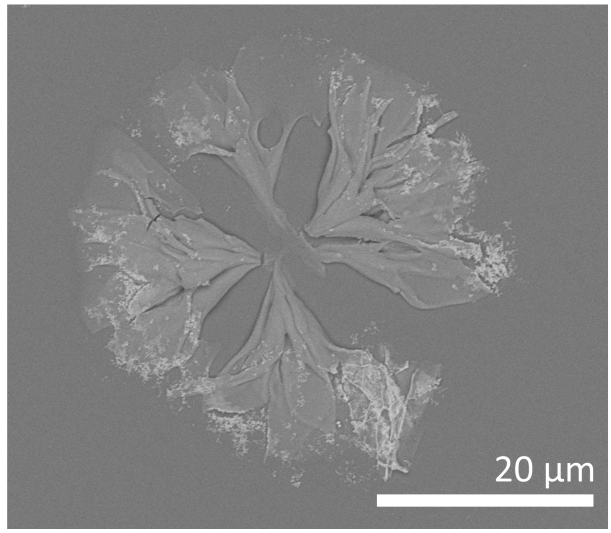


**Figure A.33:** Nanocomposite kept in a $SnCl_2$ conversion solution for 2 minutes. As the local reaction zone disappears around the nanocomposites after 30 seconds, this nanocomposite is depleted of its tin content.

#### Increasing pH throughout the whole solution

To discover the mechanism behind the tin conversion, we looked more carefully at the reaction of tin with water without the addition of $BaCO_3/SiO_2$ nanocomposite architectures. If tin is dissolved in water and kept under nitrogen atmosphere, a white precipitate is formed after 30 minutes. This white precipitate was collected via vacuum filtration and analyzed using XRD. Comparing the obtained XRD diffractogram (Figure A.34, top) with AMCSD 0015835 confirmed the formation of Abhurite ($Sn_{21}O_6(OH)_{14}Cl_{16}$). Abhurite also forms under atmospheric conditions (Figure A.34, middle) at an accelerated rate (within 5 minutes), and an amorphous bump is also observed in the XRD pattern.

We hypothesize that the nanocomposites locally change the reaction conditions. This is based on the formation of hydroromarchite in the nanocomposites, rather than abhurite. Furthermore, the time scale of the formation rate also is widely different when adding the nanocomposites compared to precipitation without (30 seconds with vs. 30 minutes without), We theorized that this could be due to a change in pH, as abhurite is stable at pH 2-5.5 (Edwards, R., Gillard, R.D., Williams, P.A. *Mineral. Mag.* **1992**, 56, 221–226), while hydroromarchite only precipitates above a pH of 3.5. As the pH of the bulk solution is around 2.0, it seems likely that hydroromarchite only forms because of an elevated pH in the nanocomposites. To confirm this, we repeated the above mentioned experiment, but now at the start we also added 1M NaOH (10 mL to a 50 mL 2M $SnCl_2$ solution). Now, precipitate formed instantly, much like the 30 second conversion we observe with our nanocomposites. Analyzing this precipitate with XRD (Figure A.34, bottom) furthermore confirmed the formation of hydroromarchite (compared with COD 9011384). Finally, when we use the nanocomposites, the precipitate only forms locally in the nanocomposites. Thus, we concluded that the basic conditions induced by the dissolving the $BaCO_3$ allows the hydroromarchite to form inside the nanocomposites.

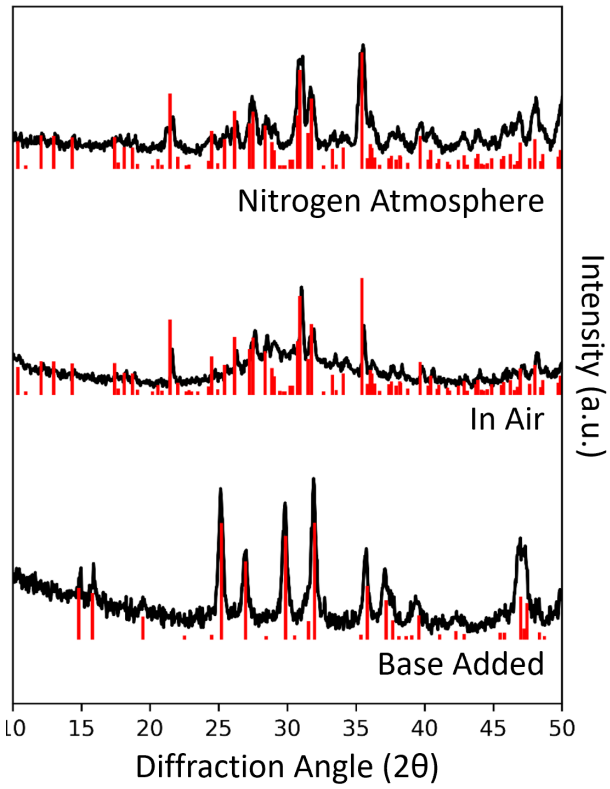


**Figure A.34:** XRD of precipitate formed in water when dissolving $SnCl_2$ under nitrogen (top), in air (middle) and after adding 1M NaOH (bottom).

### A.2.8 Change in Volume Determination

The microscale shrinking during the transition from $BaCO_3/SiO_2$ architectures to $CdS/SiO_2$ architectures was determined before and after conversion. We explain the procedure with the architecture in Figure A.35.

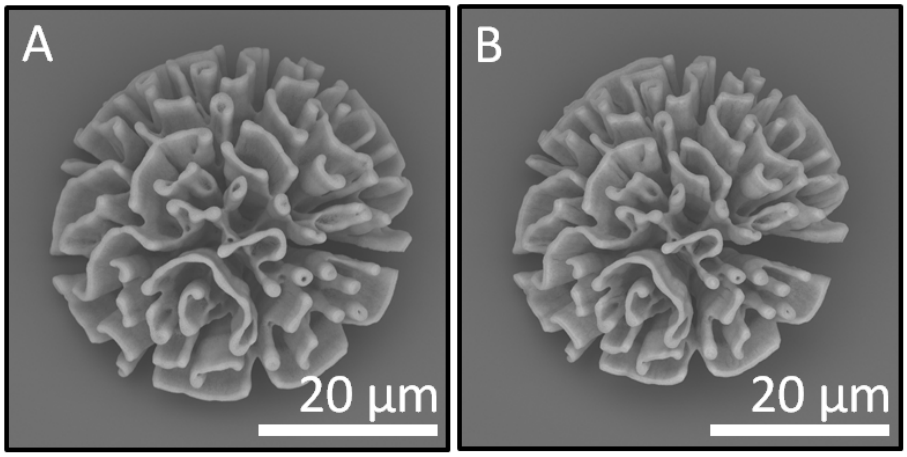


**Figure A.35:** SEM images of $BaCO_3/SiO_2$ architectures **A,** before and **B,** after conversion to CdS.

All of the analyzed architectures are coral-shaped with multiple extrusions. To quantize the size of each individual extrusion the coordinates of its outermost right ($\vec{p_i}$)and outermost left part ($\vec{q_i}$) were determined as shown for the $BaCO_3/SiO_2$ architecture in Figure A.36 in yellow. Only extrusions in the imaging plane were used for further calculations to prevent errors due to taking the coordinates of the 2D representation of the extrusions, instead of the actual coordinates of the 3D extrusions.

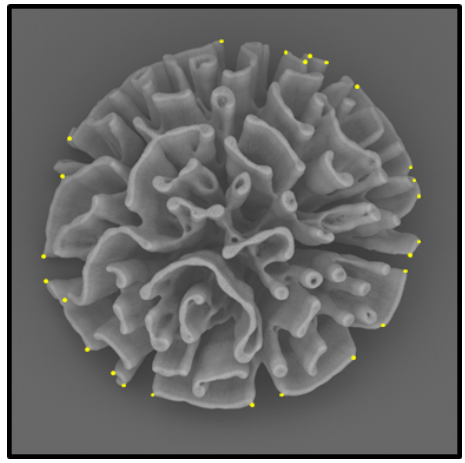

**Figure A.36:** $BaCO_3/SiO_2$ architecture with yellow points on $\vec{p_i}$ and $\vec{q_i}$.

$\vec{p_i}$ and $\vec{q_i}$ were placed in a Cartesian coordinate system where the origin is the center of the nanocomposite architecture were all extrusions originate. The origin point was determined by assuming that all extrusions roughly grow at the same rate and thus the origin is the average middle of all extrusions. As the extrusions are not uniformly distributed around the center, an ellipse fit was done on the sum of all $\vec{p_i}$ and $\vec{q_i}$ according to the technique described by Fitzgibbon, Pilu and Fischer (Direct least squares fitting of ellipsees, Proc. of the 13th Internation Conference on Pattern Recognition, 1996, Vienna, 253–257) based on code made by van Foreest (http://nicky.vanforeest.com/misc/fitEllipse/fitEllipse.html). The center of this ellipse was used as the center of all extrusions, as shown in Figure A.37.

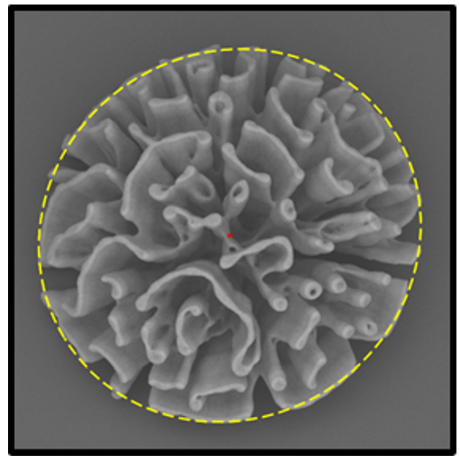

**Figure A.37:** Eclipse fit (in yellow) and its center (in red) of the $BaCO_3/SiO_2$ architecture

With the coordinate system set up, the azimuthal length ($w_i$) of an extrusion can be defined as the distance between $\vec{p_i}$ and $\vec{q_i}$ of the extrusion:

$$w_i = \left| \vec{p_i} - \vec{q_i} \right|$$

Furthermore, the radial length ($l_i$) is then defined as the distance between the middle of $w_i$ and the center of mass of all marked points $\vec{p_i}$ and $\vec{q_i}$ (Figure A.38):

$$l_i = \frac{\left| \vec{p_i} + \vec{q_i} \right|}{2}$$

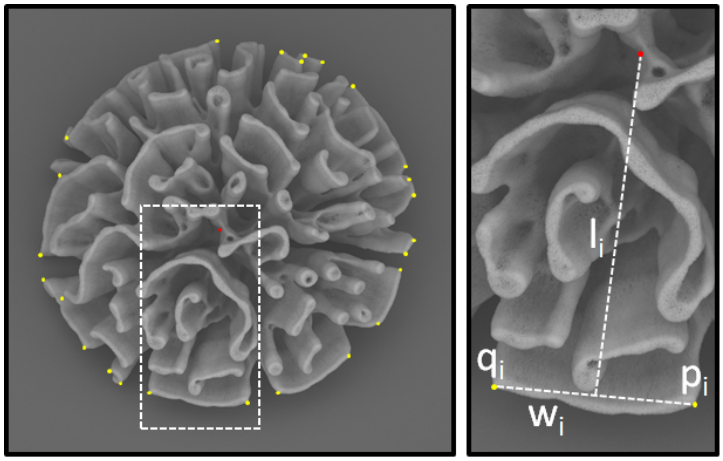


**Figure A.38:** $w_i$ and $l_i$ shown for an extrusion of the $BaCO_3/SiO_2$ architecture.

Based on these definitions of the width and length of an extrusion, the deformation of a nanocomposite architecture was determined before and after the conversion from $BaCO_3$ to CdS. The deformation in azimuthal ($\varepsilon_i^w$) direction is then the azimuthal length of the CdS extrusion ($w_i'$) expressed as its ratio to its $BaCO_3$ extrusion counterpart ($w_i$):

$$\varepsilon_i^w = \frac{w_i'}{w_i}$$

The deformation in the radial ($\varepsilon_l^i$) direction is expressed similarly as:

$$\varepsilon_i^l = \frac{l_i'}{l_i}$$

To statistically analyze the shrinkage of the nanocomposite architectures, the deformation of each individual extrusion was compared to the mean. For this the mean of $\varepsilon^{\bar{w}}$ was defined as:

$$\varepsilon^{\bar{w}} = \sum_{i=1}^{n} \frac{\varepsilon_i^w}{n}$$

with $n$ as the total amount of extrusions. Furthermore, the standard deviation was defined as follows:

$$\sigma_{\varepsilon^w} = \sqrt{\frac{\sum_{i=1}^{n}(\varepsilon_i^w - \varepsilon^{\bar{w}})^2}{n}}$$

A visual representation of $\varepsilon_i^w$ is plotted against the location of the corresponding extrusion in Figure A.39, where 0°corresponds to the positive y-axis, while going clockwise around the origin point. The dashed black line is $\varepsilon^{\bar{w}}$ and the grey domain is the area between $\varepsilon^{\bar{w}} + \sigma_{\varepsilon_w}$ and $\varepsilon^{\bar{w}} - \sigma_{\varepsilon_w}$.

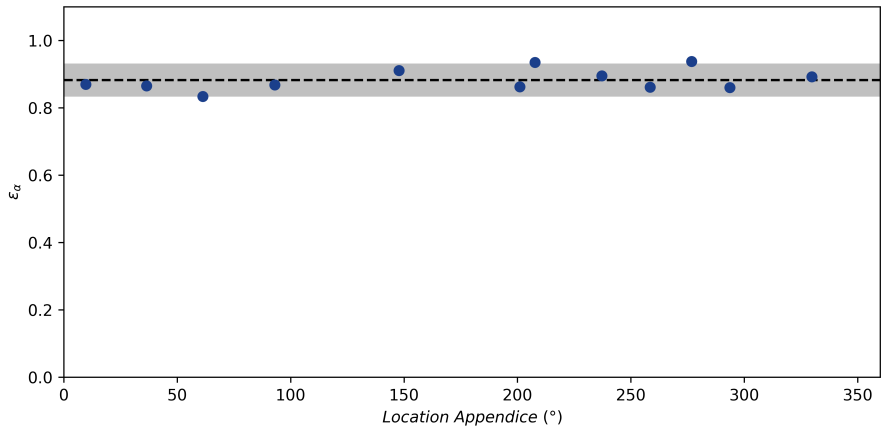


**Figure A.39:** $\varepsilon_i^w$ (blue dots)) plotted against the location of the corresponding extrusion along with the mean (black dashed line) and ±1 standard deviation domain (grey zone).

In similar fashion $\varepsilon_i^l$ can be plotted against the corresponding extrusion location in Figure A.40.

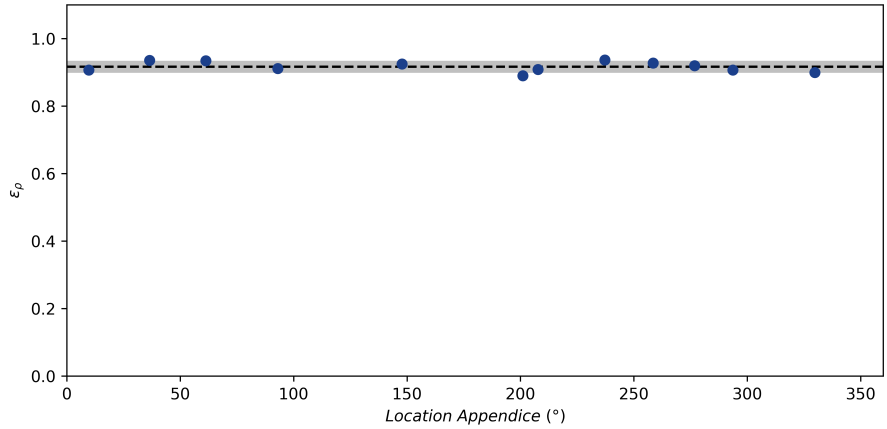


**Figure A.40:** $\varepsilon_i^l$ (blue dots)) plotted against the location of the corresponding extrusion along with the mean (black dashed line) and ±1 standard deviation domain (grey zone).

Based on these results the mean and standard deviation for both the radial and azimuthal deformation was determined to be $0.92 \pm 0.015$ and $0.88 \pm 0.031$ respectively. The volume ratio ($\varepsilon^{vol}$) was determined by assuming that this ratio between the two shapes is equal to the ratio between length·width·height, where length is equal to the radial deformation and width and height is equal to the azimuthal deformation, which results in the following formula:

$$\varepsilon^{vol} = \varepsilon^{l} \cdot (\varepsilon^{w})^2$$

From this the volume change was determined to be $0.71 \pm 0.062$. The individual volume changes and deformations for $BaCO_3$ to $CdCO_3$ and $CdCO_3$ to CdS were also determined in a similar fashion. The results are summarized in Table A.3.

| | **Radial Deformation** | **Azimuthal Deformation** | **Volume Ratio** |
|---|---|---|---|
| **$BaCO_3$ to $CdCO_3$** | $0.99 \pm 0.004$ | $0.98 \pm 0.011$ | $0.95 \pm 0.025$ |
| **$CdCO_3$ to CdS** | $0.93 \pm 0.012$ | $0.90 \pm 0.030$ | $0.74 \pm 0.059$ |
| **$BaCO_3$ to CdS** | $0.92 \pm 0.015$ | $0.88 \pm 0.031$ | $0.71 \pm 0.062$ |

**Table A.3:** Ratio of architectures volume after versus before.

**Detection of Methylamine with HPLC**

HPLC analysis was performed using an Agilent Technologies Infinity 1260 HPLC system equipped with a Chiralpak IA (250 x 4.6 mm, 5-µm) column, eluent: n-heptane/isopropanol 80/20 (v/v), flow rate: 0.7mL/min., detection: 220 nm). Retention times of 2-napthalaldehyde and the corresponding N-methylimine were determined following the procedure below 1). A 2-napthalaldehyde droplet was dissolved in isopropanol (1.0 mL). HPLC analysis of the resulting solution indicated that retention time of the aldehyde is 7.1 min. (see Figure A.41A). 2). N-methylimine ($MeNH_2$, 50 µL of 33 wt.% solution in MeOH) was added to a solution of 2-napthalaldehyde (2 mg) in isopropanol (1.0 mL). The resulting mixture was shaken for 30 seconds and allowed to react for 15 minutes at ambient temperature without stirring. HPLC analysis of the resulting solution indicated complete conversion of 2-napthalaldehyde into the corresponding imine (retention time 6.4 min., see Figure A.41 (bottom) Chromatogram B).

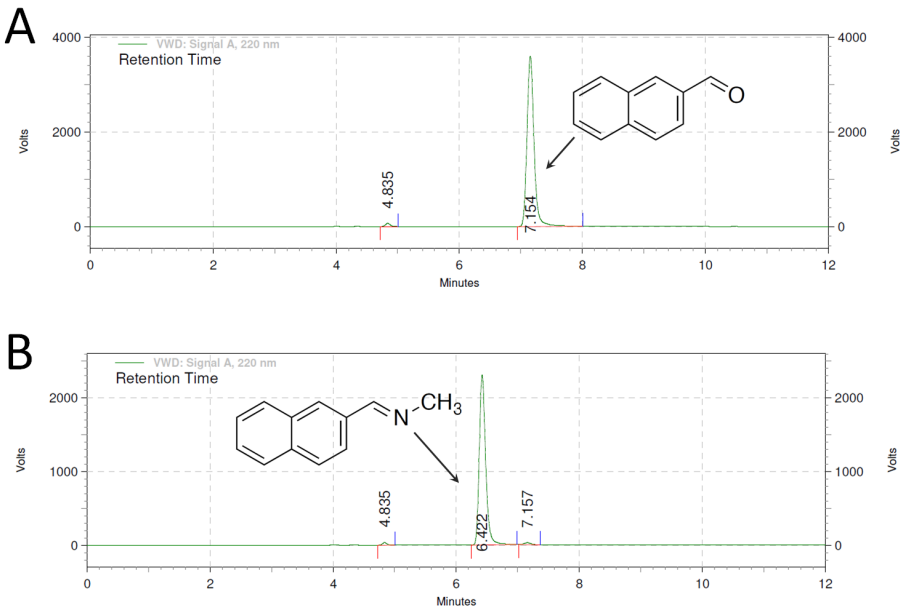


**Figure A.41:** Chromatograms of **A,** 2-napthalaldehyde, and **B,** the resulting imine.

The reaction was performed following the standard protocol in the presence of 2-napthalaldehyde. A stock solution of $MeNH_3Br$ (10 mg) and 2-napthalaldehyde (5 mg) in isopropanol (10 mL) was prepared. As expected, HPLC analysis of the stock solution confirmed that virtually only 2-napthylaldehyde was present in the mixture, thus indicating no formation of methylamine (Figure A.42A). Then, solid PbCO3 (3 mg) was added to the stock solution (0.3 mL) resulting the release of methylamine and its subsequent reaction with the present 2-napthalaldehyde to form the corresponding imine as indicated by HPLC (Figure A.42B).

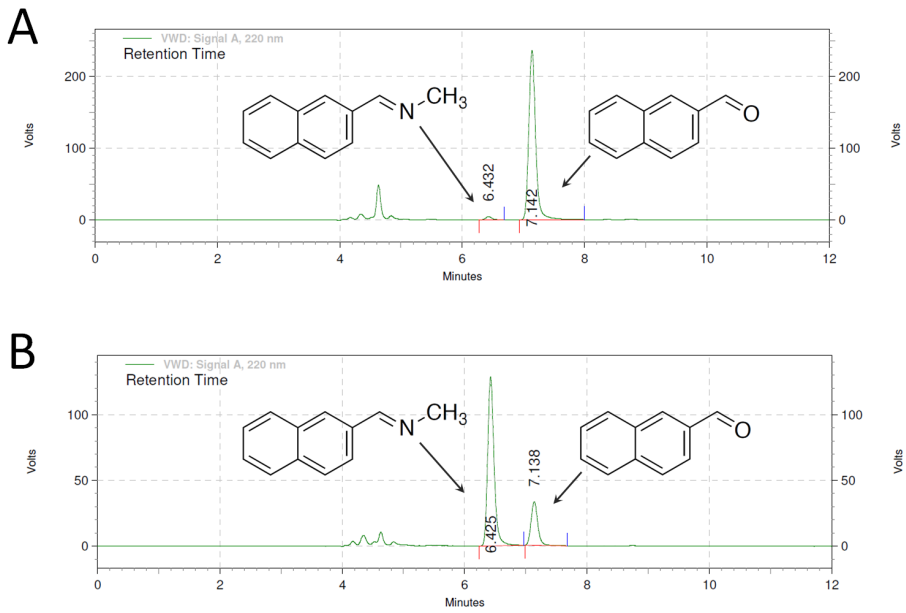


**Figure A.42:** Chromatograms of the stock solution of **A,** 2-napthalaldehyde and methylammonium bromide, and **B,** the reaction mixture upon addition of $PbCO_3$, showing the presence of the imine, which indicates the formation of methylamine during the reaction of $PbCO_3$ to methylammonium lead bromide.

## A.3 Optical Analysis Equipment and Methods

### A.3.1 Optical Microscopy Characterization

Optical microscopy analysis was performed using a Leica DMRX optical microscope equipped with cross polarizers, a Basler aCA1920-40gc camera and Pylon Viewer software. Optical microscopy analysis using crossed polarizers of the $BaCO_3/SiO_2$ coral architectures shows a Maltese cross birefringent pattern, which arises from the crystallographic alignment the c-axis of the $BaCO_3$ nanocrystals along the growth direction of the nanocomposite architecture (Figure A.43A). After conversion of the $BaCO_3$ into $PbCO_3$ this Maltese cross birefringent pattern is preserved, suggesting that the nanocrystals remain aligned (Figure A.43B).

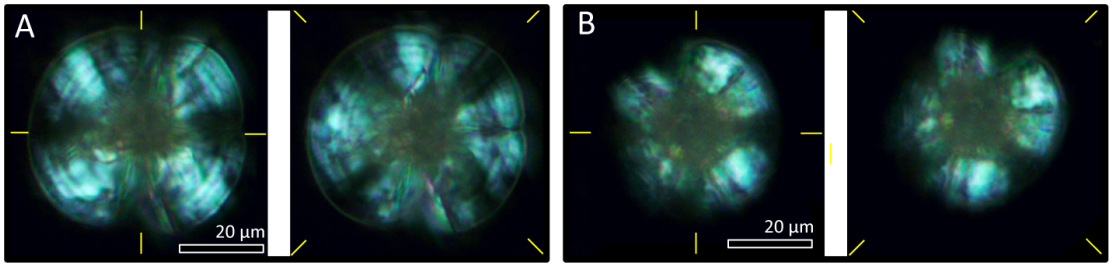


**Figure A.43: Crossed polarization microscopy study of $BaCO_3/SiO_2$ nanocomposite architectures before and after conversion to $PbCO_3/SiO_2$. A,** Maltese cross birefringent pattern of a $BaCO_3/SiO_2$ nanocomposite architecture. Alignment of the polarizers is depicted by the yellow lines. **B,** Crossed polarization microscopy image of a similar architecture after conversion into $PbCO_3/SiO_2$, demonstrating the preservation of the birefringent pattern.

### A.3.2 Photoluminescence and Fluorescence Microscopy Characterization

The photoluminescence measurements were performed on a WITec alpha 3000 SR. As light sources a 532 nm laser, a 405 nm laser (Thorlabs fiber coupled laser source S1FC405) and a 365 nm led (LedEngin Inc LZ1-10UV00-0000) were used to excite the iodide, bromide and chloride perovskite respectively. The signal was collected with a WITec UHTS 300 spectrometer and the corresponding detector (DV401A-BV-352). It should be noted that the initial calcium carbonate biominerals, the $BaCO_3/SiO_2$, $SrCO_3/SiO_2$ and $CaCO_3/SiO_2$ architectures and the converted $PbCO_3$ did not display any photoluminescence. The light emission of especially the lead bromide perovskite can be easily seen under a light microscope with the appropriate filter cube. For Figure 4.3c and Figure 4.4f a Nikon Eclipse Ci Pol microscope with a Basler aCA1920-40gc camera, Pylon Viewer software and a Nikon FITC filter cube (Ex 465-495, DM 505, BA 515-555) was used. For Figure 4.4g, a conventional photo camera (Olympus OM-D E-M1 with Olympus 12-40 pro) was used without additional filters.

### A.3.3 Cathodeluminescence Characterization

The cathodoluminescence (CL) spectroscopy characterization was performed using a FEI Quanta scanning electron microscope at 5 keV. The CL collection system was designed by Delmic. Two types of experiments have been performed. First standard CL spectroscopy, where simultaneously a spectrum and a secondary electron (SE) contrast are taken. It allows a perfect correlation between the spectrum and the SE image. The pixel size was around 400 nm, and each pixel was scanned during the pixel acquisition. The acquisition time was 100 ms per pixel. In Figure A.45 the average spectrum taken on individual coral-shaped nanocomposite architectures is shown. The main peak of chloride (left, blue), bromide (middle, green) and iodide (right, red) lead halide perovskite is respectively around 420 nm, 550 nm and 800 nm, which are compatible with the PL measurements (Figure A.44 and Figure 4.4). The nanocomposites were stable enough under the beam to allow multiple acquisitions, a slight decrease of the intensity was observed but no change in the shape of the spectrum was measured.

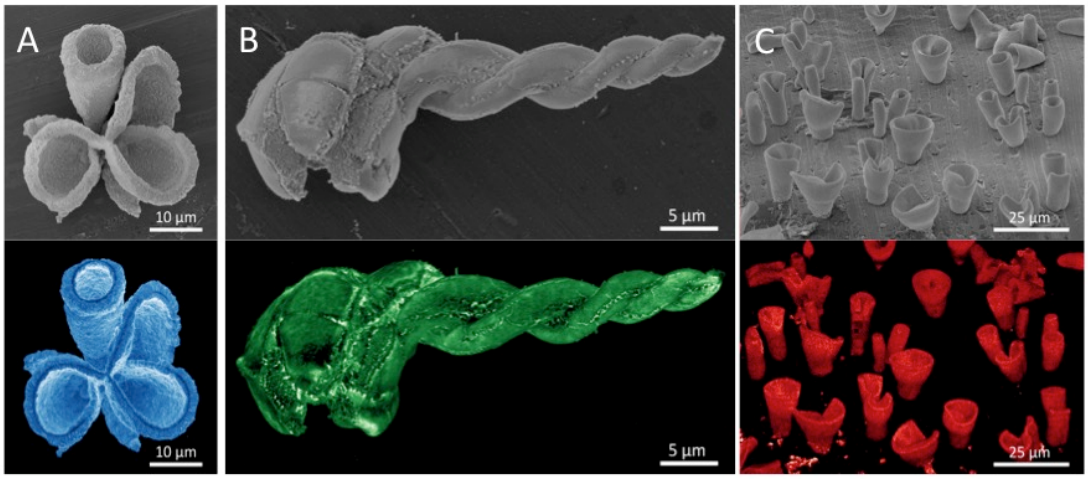


**Figure A.44: SEM and corresponding CL images of $CH_3NH_3PbX_3/SiO_2$ nanocomposite architectures.** **A,** Coral architecture containing $CH_3NH_3PbCl_3$ **B,** spiral architecture containing $CH_3NH_3PbBr_3$ and **C,** field of vase-shaped architectures containing $CH_3NH_3PbI_3$.

The CL signal can also be collected using a photomultiplier tube (PMT), in this case without any spectral selectivity. The time per pixel is therefore drastically reduced to 100 µs per pixel and large area can be scanned with a good spatial resolution. In the case of Figure 4.4 the pixel size is between 20 nm and 100 nm. These images are intensity maps, they have been color coded to represent the range of the emitted light deduced from spectra of Figure A.45: blue for $CH_3NH_3PbCl_3$, green for $CH_3NH_3PbBr_3$, and red for $CH_3NH_3PbI_3$ structures.

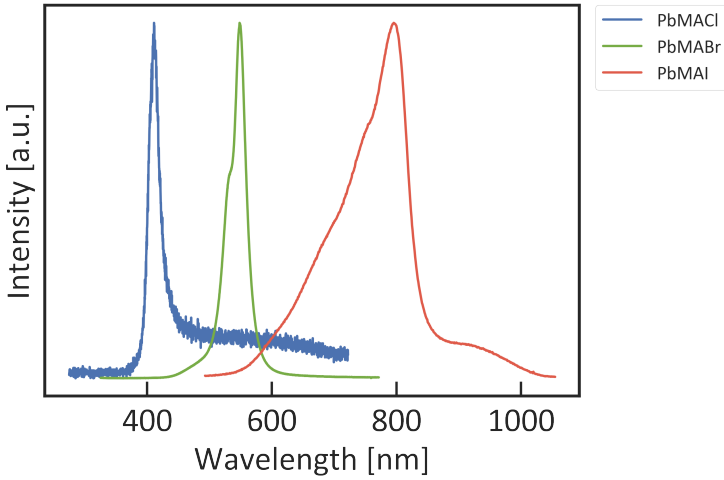


**Figure A.45: Cathodeluminescence of lead halide perovskite nanocomposite architectures.** Spectrum of $CH_3NH_3PbCl_3/SiO_2$ (blue, PbMACl), $CH_3NH_3PbBr_3/SiO_2$ (green, PbMABr) and $CH_3NH_3PbI_3/SiO_2$ (red, PbMAI) architectures.

# A.4 Catalysis Equipment and Methods

## A.4.1 XPS measurements

Surface-sensitive characterization of the composition of NiO architectures was performed using X-ray photoelectron spectroscopy of powders on Carbon tape in an ultra-high vacuum setup equipped with a Scienta Omicron HIPP-3 analyzer and a monochromated XM1200 Al K-alpha X-ray source ($E_{Photon}$=1486.7 eV). In order to quantify the Ni content and overall composition of the surface region, the integrated area of peaks of similar binding energies (Si 2p, Ni 3p, Ba 4d at kinetic energies in the range from 1380 eV to 1420 eV) have been determined and divided by the respective photoionization cross sections. The respective ratios for the nancomposite catalyst ($Ni_{convent}$) and the reference catalysts ($Ni_{equiv}$ and $Ni_{coral}$) are provided in Table A.4.

| **Ratio** / **Sample** | **Ni/Si** | **Ba/Si** | **Ni/Ba** |
|---|---|---|---|
| **$Ni_{convent}$** | 0.029 | - | - |
| **$Ni_{equiv}$** | 2.718 | - | - |
| **$Ni_{coral}$** | 2.177 | 0.437 | 4.986 |

**Table A.4:** Cation ratios in the surface region determined by XPS peak areas (Ni 3p, Si 2p, Ba 4d) corrected for photoionization probability

The observed ratios demonstrate a very low loading with Ni in the surface region for the sample with $Ni_{convent}$. Owing to the very low intensity on Ni 3p, the absolute value should be considered only with error bars of approximately 50% for this sample. In both other samples, the Ni content is substantially higher and therefore have more accurate results with error bars below 10%.

## A.4.2 Dry Reforming Measurements

### Synthesis of reference catalysts

$Ni_{convent}$ ($NiO/SiO_2$ with a 5 wt.% Ni metal loading) and $Ni_{equiv}$ ($NiO/SiO_2$ with a 77 wt.% Ni metal loading) catalysts were prepared by the wet impregnation method. The desired amount of $Ni(NO_3)2 \cdot 6H_2O$ (98%, Alfa Aesar) was impregnated on $SiO_2$ (Davison Grace 62), using a water to solid ratio of 10 $mL \cdot g^{-1}$. The formed slurry was dried under stirring at 65 °C for 24 h. After impregnation, the final solid was dried at 120 °C during 2 h and then calcined in air at 450 °C for 4 h (heating rate of 4 °C $\cdot$ $min^{-1}$). The available Ni atoms of $Ni_{convent}$, $Ni_{equiv}$ and the $Ni_{coral}$ were determined with XPS (Table A.4.1) to be 3%, 73% and 52.5% respectively.

### Catalytic tests

The catalytic tests were carried out under atmospheric pressure in an automated six-flow parallel reactor system. It consists of six individual fixed-bed quartz reactors located in a furnace. 67 mg of $Ni_{coral}$, 20 mg of $Ni_{convent}$ and 67 mg of $Ni_{equiv}$ were tested in the form of pellets (1.0-0.7 mm of diameter). The reaction was carried out at 400 °C using stoichiometric ratio of the reactants ($CO_2$:$C_4H_{10}$=4:1). The feed gas was diluted with 80% of Ar and a total flow of 10 mL/min was passed through the reactors. The reactants and products were analyzed with a gas chromatograph (Interscience microGC), which contains two detectors (flame ionization (FID) and thermal conductivity (TCD)), and four separation columns (Wax column (4 m length) + RTX-1 column (0.5 m length) and Rt-Alox/Na2SO4 column (10 m length and 0.32 mm width) for FID, and RT-Q bond column (3.0 m length and 0.32 mm width) and Carboxen 1010 column (15 m length and 0.32 mm width) for TCD).

The formulas used to calculate conversion, selectivity (product fraction) and carbon balance are:

$$CO_2 \text{ conversion}(\%) = \frac{[CO_2]_{in} - [CO_2]_{out}}{[CO_2]_{in}} \cdot 100 \tag{A.5}$$

$$CO \text{ fraction}(\%) = \frac{[CO]_{out}}{\sum [products]_{out}} \cdot 100 \tag{A.6}$$

$$\text{Carbon balance}(\%) = \frac{[C]_{out}}{[C]_{in}} \cdot 100 \tag{A.7}$$

The turn over frequency (TOF) was calculated using the following formula, where % NiO available on the surface is obtained from the XPS results.

$$\text{TOF } CO_2 = \frac{[CO_2]}{\%NiO_{surface} \cdot [NiO]_{catalyst}} \tag{A.8}$$

An overview of the catalytic results obtained after 30 minutes are shown in Table A.5.

| Catalyst | $CO_2$ conversion (%) | Butane Conversion (%) | $CO_2$ TOF | Butane TOF | CO selectivity (%) | $H_2$ selectivity (%) | $CH_4$ selectivity (%) | $C_2$ species selectivity (%) | Carbon balance (%) |
|---|---|---|---|---|---|---|---|---|---|
| $Ni_{coral}$ | 10.3 | 3.2 | 48.4 | 37.6 | 52.5 | 47 | 0 | 0.6 | 93.2 |
| $Ni_{equiv}$ | 31 | 3.1 | 31.1 | 75.4 | 21.0 | 45.8 | 7.0 | 19.2 | 83.3 |
| $Ni_{convent}$ | 0 | 0 | - | - | - | - | - | - | - |

**Table A.5: Catalytic performance of the Ni materials after 30 min on stream.** Reaction conditions: 400 °C, atmospheric pressure, $CO_2$:Butane = 4:1, total flow = 10 mL/min.

### A.4.3 Catalytic Reactor Fischer-Tropsch

Cobalt-containing nanocomposite catalysts were tested for the FTS at 20 bar, 220 °C, $H_2$/CO = 2/1 and GHSV =320 mL/gcat/min. Figure A.46 shows the experimental set-up used for the FTS experiments. The $Co_3O_4/SiO_2$ nanocomposite catalysts (160 mg) were diluted with SiC (1:6), located in a 10 mm diameter Hastelloy reactor, and reduced to $Co/SiO_2$ nanocomposites at 400 °C with $H_2$ (10 vol% in $N_2$ with a flow rate of 50mL/min). Above the catalysts and next to the reactor inlet, a bed of SiC was placed to ensure the gases pre-heaten. The reactor was placed in an oven (Carbolite Gero) and the temperature was measured with a thermocouple at the reactor exit and one thermocouple inserted in the SiC bed. The liquid products are collected in a hot-trap at the reactor exit, while the gases flown through a heated line at 250°C, towards the gas chromatograph (Trace 1300, Thermo Fisher Scientific).

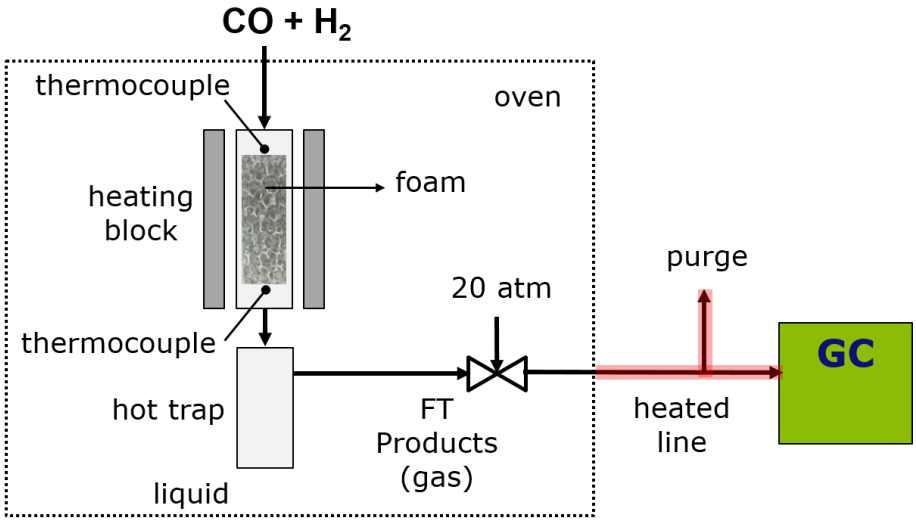


**Figure A.46:** Experimental set-up for the FTS.

The gas chromatograph contains two TCD and two FID detectors. One line (columns MXT-1 and MXT-QBond), connected to a FID detector, is used to quantify the short hydrocarbons ($C_1$-$C_3$); and $CO_2$ in a TCD detector. In the second line (column RTX-1) the long hydrocarbons ($C_4$-$C_{25}$) are analyzed in an FID detector. The permanent gases are quantified using a TCD detector.

# Abstract

Imagine if a house would not need effort to be build, but rather assembled on its own. Or if a car would repair itself if it broke down. This might sound like a futuristic perspective, but in nature it is quite a common phenomenon: a chick 'assembles' itself inside an egg without any outside interference, and a broken bone can repair itself over time. What if we could unravel the processes behind this self-assembly and use it to build our own materials?

In this thesis, we use a bioinspired strategy to bring self-assembly processes to man-made materials. In this strategy, barium carbonate ($BaCO_3$) co-precipitates with silica ($SiO_2$) to form nanocomposites: a material where nanocrystals of $BaCO_3$ are embedded in a supporting matrix of $SiO_2$. These nanocomposites have two particular properties that we exploit in this thesis: First, their shape can be sculpted during the co-precipitation, allowing the overall nanocomposite's architecture to be tailor-made for its intended application. Second, the small size of the $BaCO_3$ crystals makes them very reactive, whereas the $SiO_2$ gives the nanocomposites mechanical stability. We use this combination of chemical reactivity and mechanical stability to change the composition of the nanocomposites, where the new composition inherits the shape of the original nanocomposite. In short, this allows us to shape a material for processes like catalysis or photovoltaics, and then change its composition to make it functional for their intended purpose.

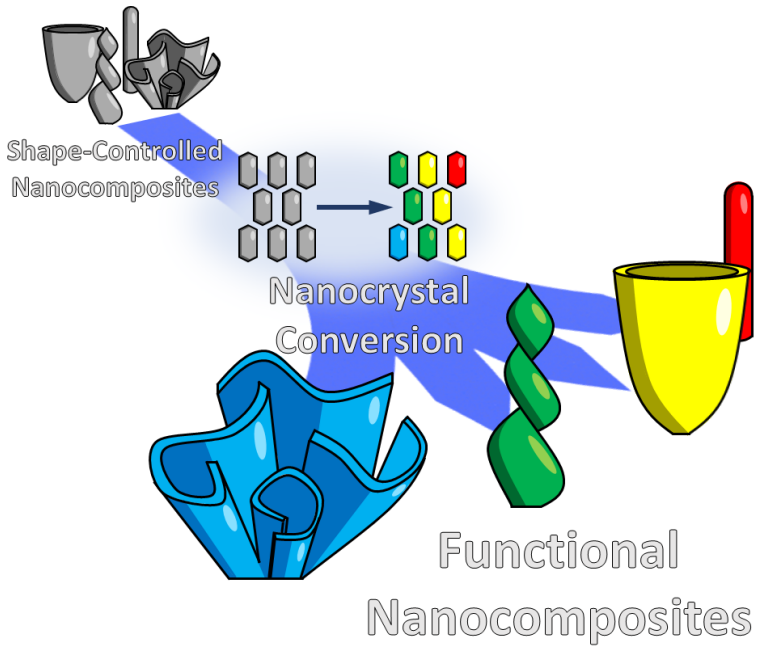


**Figure 1: Main concept of the thesis.** We first sculpt the nanocomposites into an architecture with a particular shape. These nanocomposites are made out of nanometer-sized crystals, which we convert in a second step to new crystals with various functionalities. Hence, we create functional nanocomposites whose shape can be sculpted independently of the resulting material.

To develop this assembly/conversion strategy, we first investigate a single conversion pathway as a case study. **In Chapter 2**, we investigate the conversion from $BaCO_3$ to cadmium carbonate ($CdCO_3$), and subsequently the conversion from $CdCO_3$ to cadmium sulfide (CdS). These conversions are driven by a difference in solubility and concentration ($BaCO_3$ to $CdCO_3$), or *via* the decomposition of the carbonate anion in a sulfide-rich environment ($CdCO_3$ to CdS). We observe a complete overhaul of the elemental and crystallographic structure of the nanocomposite while performing these conversion reactions, which confirms their feasibility.

We then delve deeper into the mechanism of these conversions and analyze how the conversion affects the individual crystals of the nanocomposite, as well as its effect on the overall architecture of the nanocomposite. We observe a shrinkage of the microscale architecture, which can be correlated to the reduced volume of the individual nanocrystals. Yet, the overall shape of the architecture remains preserved throughout the conversion, indicating that the mechanical stability of the $SiO_2$ matrix is sufficient to overcome the stress induced by this shrinkage.

The lessons learned from analyzing the conversion from $BaCO_3$ to the eventual CdS are readily expanded to other metals. We finish Chapter 2 by assembling nanocomposites with various shapes and converting them to iron-, manganese-, cobalt-, and nickel-oxide/sulfides. With this, we demonstrate that our assembly/conversion strategy gives independent control over shape and composition, which in turn makes any combination of shape and composition possible for the nanocomposites.

**In Chapter 3**, we investigate potential applications for the converted nanocomposites. We start with exploring the field of catalysis, as the structural layout of the nanocomposites has many desirable properties for catalysis (e.g. high metal content, large surface area and small individual crystal sizes). To test whether the nanocomposites benefit catalytic processes, we employ nickel- and cobalt-containing nanocomposites as heterogeneous catalysts.

The nickel-nanocomposites are used for dry reforming. In this process, butane ($C_4H_{10}$) and carbon dioxide ($CO_2$) are converted into hydrogen ($H_2$) and carbon monoxide (CO). To benchmark the nanocomposite catalysts, we compare them to traditionally prepared catalysts under identical reaction conditions. Remarkably, the nanocomposite catalysts outperform traditional catalysts at low temperature in these tests, thus making the nanocomposite catalysts interesting candidates for this process.

We then use the cobalt-nanocomposites for the Fischer-Tropsch synthesis, where $H_2$ and CO are converted to hydrocarbons ($C_xH_{x+2}$) and water ($H_2O$). Here we vary the conditions of our conversion reactions to change the size of the nanocomposite's individual crystals. In doing so, we are able to tune the carbon chain length of the formed hydrocarbon, allowing us to produce different products like gasoline or lubricant oil. Combined with the dry reforming results, these results demonstrate that converted nanocomposites can be used as catalysts with competitive activity, as well as tunable selectivity.

The range of applications for the converted nanocomposites can be expanded beyond the field of catalysis. **In Chapter 4**, we develop a new conversion pathway to lead halide perovskites, a material currently receiving much scientific attention because of its photovoltaic properties. These perovskites show great potential as semiconductors for the next generation of solar cells and light emitting devices, while many opportunities for these perovskites remain yet to be discovered. One of these opportunities is to shape the perovskite in 3D. We demonstate a strategy to do so by converting the nanocomposites to perovskites, where a sculptable 3D shape can be inherited from the original nanocomposites, giving rise to shapeable 3D perovskites. Furthermore, these nanocomposite perovskites still demonstrate the same photovoltaic properties as 2D state-of-the-art perovskites. Thus, our assembly/conversion strategy allows the formation of 3D materials with potential application in the field of photovoltaics.

Finally, we investigate other potential conversion pathways for the nanocomposites. **In Chapter 5**, we convert the crystals in the nanocomposites to tin-containing compounds. This is impossible *via* a traditional cation exchange ($BaCO_3$ to $SnCO_3$), as tin does not form a stable carbonate. Yet, we discover in this chapter that the local reaction conditions stabilize the conversion to a different tin intermediate: hydroromarchite ($Sn_3(OH)_2O_2$). Moreover, this $Sn_3(OH)_2O_2$ can be further converted to both tin dioxide ($SnO_2$) and tin perovskite ($CH_3NH_3SnX_3$), making it behave very similar to the carbonate intermediates synthesized in the earlier chapters. With this, we show the versatility of our assembly/conversion strategy, and hint that many more possible conversion pathways are yet to be discovered.

Overall, this thesis describes a new assembly/conversion strategy for nanocomposites, where control over their shape and composition are divided in two seperate steps. This allows for the creation of nanocomposites with a wide range of shapes and compositions, which can be tailored to specific applications. We demonstrate the potential of this by applying the converted nanocomposites for both catalytic and photovoltaic applications. In doing so, we demonstrate the strength of bioinspired self-assembly (where matter organizes itself in complex architectures), when combined with conversion reactions (where the composition can be tuned for man-made applications).

# Samenvatting

Stel je voor dat je geen moeite in het bouwen van een huis hoeft te stoppen, maar dat het zichzelf in elkaar zet. Of wanneer een auto kapot gaat, deze zichzelf weer repareert. Dit klinkt misschien futuristisch, maar in de natuur komt dit gewoon voor: een kuiken 'zet zichzelf in elkaar' in zijn ei zonder dat het daar hulp van buiten voor nodig heeft, terwijl een gebroken bot zichzelf over tijd weer heelt. Wat nou als we het mechanisme achter zulke zelf-assemblage zouden begrijpen en konden gebruiken in onze eigen materialen?

In deze thesis gebruiken we een strategie geïnspireerd door de natuur om zelf-assemblage naar artificiële materialen te brengen. In deze strategie co-precipiteert barium carbonaat ($BaCO_3$) samen met silica ($SiO_2$) om nanocomposieten te vormen: een materiaal waar nanokristallen van $BaCO_3$ in een ondersteunende matrix van $SiO_2$ zijn ingebouwd. Deze nanocomposieten hebben twee eigenschappen die we in deze thesis zullen gebruiken: Ten eerste kan hun vorm geboetseerd worden tijdens de co-precipitatie, waardoor hun volledige architectuur afgestemd kan worden op hun uiteindelijke functie. Ten tweede maakt de kleine afmetingen van de $BaCO_3$ kristallen deze zeer reactief, terwijl de $SiO_2$ de nanocomposiet mechanische stabiliteit geeft. We gebruiken deze combinatie van chemische reactiviteit en mechanische stabiliteit om de compositie van de nanocomposieten te veranderen, waar de nieuwe compositie de vorm van de originele nanocomposiet overneemt. Kort samengevat betekent dit dat we een materiaal een specifieke vorm voor zijn toepassing kunnen geven, en vervolgens de compositie van dat materiaal kunnen aanpassen om deze functioneel te maken voor die toepassing.

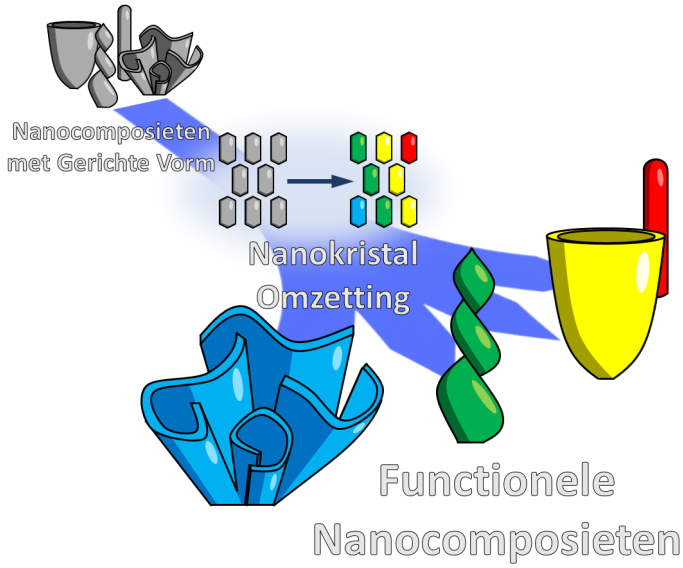


**Figuur 1: Het hoofdprincipe van deze thesis.** Eerst geven we nanocomposieten een architectuur met een gerichte vorm. Deze nanocomposieten bestaan uit nanometer-grote kristallen, die we in een tweede stap omzetten naar nieuwe kristallen met verscheidene functies. Hiermee kunnen we functionele nanocomposieten maken die we ongeacht van hun compositie vorm kunnen geven.

Om deze assembleer/omzet srategie te ontwikkelen, kijken we eerst naar een individuele omzettingsroute. **In Hoofdstuk 2** onderzoeken we de omzetting van $BaCO_3$ naar cadmium carbonaat ($CdCO_3$), die we opvolgen met de omzetting van $CdCO_3$ naar cadmium sulfide (CdS). Deze omzettingsreacties worden aangedreven door een verschil in oplosbaarheid en concentratie ($BaCO_3$ naar $CdCO_3$), of via de decompositie van het carbonaat anion in een sulfide-rijke omgeving ($CdCO_3$ naar CdS). Tijdens deze omzettingen zien we een volledige verandering van de elementencompositie en kristalstructuur van de nanocomposieten, waarmee we bevestigen dat omzettingsreacties mogelijk zijn.

We gaan dan dieper in op het mechanisme achter deze omzettingen en analyseren hoe dit de individuele nanokristallen en de volledige architectuur beïnvloedt. We zien een krimp van de architectuur op de microschaal, die we kunnen verbinden met de verandering in volume van de individuele nanokristallen. Echter, de algemene vorm van de architectuur blijft in tact door alle omzettingsreacties heen, wat aangeeft dat de stabiliteit van de ondersteunende $SiO_2$ matrix voldoende is om de stress veroorzaakt door de krimp te overkomen.

De principes van de omzetting van $BaCO_3$ naar CdS kunnen ook gebruikt worden voor de omzetting naar andere metalen. We sluiten Hoofdstuk 2 af door nanocomposieten in verschillende vormen te assembleren en ze om te zetten naar ijzer-, mangaan-, cobalt- en nikkeloxides/sulfides. Hierdoor laten we zien dat ons assembleer/omzet strategie onafhankelijke controle over de vorm en compositie geeft, wat betekent dat de nanocomposieten in elke combinatie van vorm en compositie te maken zijn.

**In Hoofdstuk 3** kijken we naar potentiële toepassingen voor de omgezette nanocomposieten. We beginnen met het veld van katalyse, omdat de structurele indeling van de nanocomposieten verscheidene eigenschappen heeft die ze interessant maken om te gebruiken als katalysator (bijvoorbeeld een hoge metaal inhoud, een groot oppervlak en kleine individuele kristalgroottes). Om te onderzoeken of de nanocomposieten functioneren in katalytische processen, gebruiken we nikkel- en cobalt-bevattende nanocomposieten als katalysatoren.

De nikkel-bevattende nanocomposieten gebruiken we voor het reformeren van koolstofdioxide ($CO_2$). In dit proces wordt $CO_2$ in combinatie met butaan ($C_4H_{10}$) omgezet in waterstof ($H_2$) en koolstofmonoxide (CO). Om deze nanocomposieten te testen vergelijken we ze met standaard katalysatoren onder indentieke reactie condities. Uit deze tests blijkt dat op lage temperaturen de nanocomposiet katalysatoren beter werken dan de traditionele katalysatoren, wat de nanocomposiet katalysatoren een interessante optie voor dit proces maakt.

Hierna kijken we hoe de cobalt-bevattende nanocomposieten presteren in de Fischer-Tropsch synthese, waar $H_2$ en CO omgezet worden in koolwaterstoffen ($C_xH_{x+2}$) en water ($H_2O$). Voor dit proces variëren we de reactie condities tijdens onze omzettingsreacties, wat een verschil in kristalgrootte in de omgezette nanocomposieten geeft. Hiermee zijn we in staat om de koolstofketen-lengte te beïnvloeden tijdens de katalyse, waarmee we verschillende producten als benzine of smeerolie kunnen maken. Dit, in combinatie met de resultaten van de reformatiekatalyse, laat zien dat de omgezette nanocomposieten gebruikt kunnen worden als katalysatoren die een competatieve activiteit en aanpasbare selectiviteit hebben.

De toepassingsmogelijkheid van de omgezette nanocomposieten kan makkelijk uitgebreid worden naar andere velden buiten het veld van katalyse. **In Hoofdstuk 4** ontwikkelen we een nieuwe omzettingsroute naar lood halide perovskieten, een materiaal dat op het moment veel wetenschappelijke aandacht heeft vanwege zijn fotovoltaïsche eigenschappen. Deze perovskieten heb-ben de potentie om te dienen als halfgeleiders voor de volgende generatie van zonnecellen en lichtgevende apparaten, en er zijn nog vele kansen onbenut voor dit materiaal. Één van deze kansen ligt in het vorm geven van perovskieten in 3D. Wij laten zien dat door nanocomposieten om te zetten in perovskiet, we de 3D vorm van de originele nanocomposiet kunnen doorgeven en hiermee vorm-gecontroleerde 3D perovskieten kunnen maken. De omgezette nanocomposiet heeft daarbij nog steeds dezelfde fotovoltaïsche eigenschappen als hoogwaardige 2D perovskiet. Dus geeft onze assembleer/omzet strategie ons hier 3D materialen die potentieel toegepast kunnen worden in het veld van fotovoltaïsche energie.

Als laatste kijken we naar alternatieve omzettingsreacties voor de nanocomposieten. **In Hoofdstuk 5** zetten we de kristallen in de nanocomposieten om naar tin-bevattende kristallen. Dit is onmogelijk om te doen met een normale kation-uitwisseling ($BaCO_3$ naar $SnCO_3$), omdat tin geen stabiel carbonaat vormt. In dit hoofdstuk ontdekken we echter dat de locale reactie condities een omzetting naar een ander tin zout stabiliseren: hydroromarchiet ($Sn_3(OH)_2O_2$). Dit $Sn_3(OH)_2O_2$ kan verder omgezet worden naar tin dioxide ($SnO_2$) en tin perovskiet ($CH_3NH_3$ $SnX_3$), waarbij het zich vergelijkbaar gedraagt als een carbonaatzout zoals beschreven in de vorige hoofdstukken. Hieruit blijkt dat ons assembleer/omzet strategie erg flexibel is en dat er waarschijnlijk nog veel meer omzettingsroutes te ontdekken zijn.

Alles samen genomen laat deze thesis een nieuwe omzet/assembleer strategie zien, waarbij de controle over de vorm en compositie wordt gescheiden in twee stappen. Hierdoor kunnen we nanocomposieten met een wijde selectie aan vormen en composities creëren, die op maat kunnen worden gemaakt voor een specifieke toepassing. We laten de potentie hiervan zien door de omgezette nanocomposieten toe te passen in zowel katalytische als photovoltaïsche toepassingen. Hiermee laten we de kracht van natuur-geïnspireerde zelf-assemblage zien (waar materie in complexe architecturen kan vormen), wanneer dit gecombineerd wordt met omzettingsreacties (waarmee de compositie op maat gemaakt kan worden voor artificiële toepassingen).

# Acknowledgements

Never start a mail with 'I' I have been told; it makes it sound self-centered. How weird is it then to start a section about others, who were crucial for the success of my PhD, with something about myself? Yet, I feel I cannot express how special these people are without mentioning one particularity about myself. You see, I don't bond particularly strongly. Meeting new people is no problem, but to maintain a relation with them instead of moving on to something/someone new is something I am still trying to improve. However, the people below have been able to defy this habit of mine and have been able to become special to me. That, in my opinion, makes each of them special, on top of what I will say about them below.

Wim, I believe many people have already told you that you are a remarkable person, remarking your enthusiasm, your creative ideas or your ability to convey either to your audience. I will happily be among those who say this, though I want to add some additional points from my experience with you as my supervisor. You see, the things I respect the most about you are the things that are behind this enthusiasm. Your care for your employees, the sincerity in your research and your willingness to improve as a person are the core values that I respect in you. I am happy that you were able to convince me to come do a PhD in your group.

Not that the Self-Organizing Matter group is unremarkable without its group leader. Lukas, I am happy to have shared first PhD-ship in this group. You still puzzle me, I feel at times we are very alike, but each in their unique way. This has given me a valuable insights, not too similar to be obvious, nor too alien to be incomprehensible. Whether it has been in the PV, during one of your parties or in the lab, I have truly appreciated our time together.

Iarik, your arrival into my office meant I finally had a stable officemate that remained longer than a few months. And with it came opportunities to talk about... well, anything really. Existential questions, sources for motivation, plans for life, badly behaving experiments (or people) in the lab... everything was open to discussion. Also the more difficult points I suppose, like me learning to deal with criticism or taking 3 years to find time for things like karaoke. These discussions have been paramount for me handling my PhD, and therefore it was only logical to also have you as my paranymph. I hope you will find what you want to do in life, and I hope we can discuss about it when you do.

Arno, your name can be placed almost anywhere within these acknowledgements. When thanking my paranymphs, or fellow researchers, or friends... you have all these bases covered. This should emphasize the large part you have in my life, and I am happy you are the person to do so. I remember asking you whether you were interested in doing an internship in our group, not realizing that your work would become so fundamental to my PhD. And I guess that summarizes why I am happy that you have the role in my life that you do: you are reliable, committed and also just a lot of fun to be around!

Marloes, the first time we met you were not even part of the group, but already vital to my research with your presentation about IR spectroscopy. I'm glad you kept helping me forward when you did join the group, be it in my research or in understanding the female perspective of dating. Christiaan, ever since you applied to the SOM group, I have been impressed by your attitude towards things. You clearly know a lot about things, and otherwise you quickly can comprehend new concepts by just observing them. Yet, you give things the chance to develop

on their own, using your intellect to work with them, rather than overruling them with your own ideas. This gives you a certain type of grace that I really appreciate. Also, thank you so much for helping me build my own pc! Sjoerd, though we haven't spend too much time together, I have been impressed with your knowledge about your occupations. Whether it is chemistry knowledge for a project you haven't even started, or how to compose a musical piece, it was inspiring to listen to your knowledge while I was trying to put my own research into words.

Furthermore, the students of the SOM group have been an asset to my PhD time. Nesrine, Ariane, Imane, Daniel, Bruno and Pietro, thank you for the many conversations we had and different personalities you brought to our group. Tim, thank you in particular for the pioneering work you did on the perovskite conversion, it became the starting point of my PhD research. Stivell, I am glad to have had you under my supervision. I remember you saying to me that you felt like I didn't like any of the plans you proposed, and it really struck me as I really appreciated them and just wanted to give feedback. In the end you even solved the mystery, which is why I could include my final chapter! I hope the new 3D-printing-with-welding job suits you, but if not, you can always become a great jam session bassist!

Of course, the SOM group would not be the SOM group without it's supporting staff. Teresa, your cheerful attitude and can-do mentality have inspired me many times to do things I was unsure about myself whether they would work. And I have been suprised by all the things possible, except for dancing that is. Marc, thank you for organizing our chemical lab, and your contributions during the sports day which always led us to top 5 placings! Hinco, thank you for your down-to-earth approach on handling things. I remember when first getting to AMOLF I was overwhelmed with all the opportunities that AMOLF presented me. Luckily you were there to make things simple, instead of overanalyzing things like a PhD-brain tends to do. Yet, you also reminded me at times to actually spend more time on the important people who assist my activities. Though I might not have appreciated that at that time, I do fully support the sentiment and will take the lesson into regard when it comes up again. Finally, I would like to thank Hans and the Nanocenter group for supporting the SOM group. Without you all, I wouldn't have learned how to work in a cleanroom and probably would've had to quit due to a defective Verios. Dimitry and Bob, thank you as well for your active participation in the activities organised by the PV!

In my time at AMOLF, I also had the opportunity to be part of the wonderful PV. I fondly remember the many borrels, 'uitjes', and of course the Christmas lunches we organized. Niels, Giorgio, Konrad, Lennard, Tom, Jeffrey, Isabelle, Christian, Lukas, Sukanth, Giulia, Annemarie, Loretta, Lennard and Floortje, thank you for making this happen with me, I believe it has been one of my most valued experiences while being at AMOLF. Floortje, thank you in particular for setting a great example of how this PV should be chaired, following in you footsteps was a great way for me to take on the role myself.

Both my scientific contributions and many PV activities would not have been possible without the assistance of many technical supporting members. For example, the Drawing Department (Ilyah, Ricardo, Henk-Jan, Marnix and Dirk-Jan) were always there to design planets, brains or whatever else was needed for our crazy ideas. Then, Jan and the Mechanical Workshop would be able to assist Niels to actually create these things, as well as UFO's, Tree Supports and many more incredible objects. Andre and the facilities crew would then make sure that everything was set in place, with Wiebe and Richard taking care of the technical part and Paula approving the ideas (and paying for them). Thank you all, the PV was/is great thanks to your support.

Yet, the support of AMOLF doesn't stop there. Juliëtte and Ad were always there for a warm welcome when I arrived and were available for interesting chats about the influence of clothes on the weather forecast or how to roll from a student job into a dream job. Karelia, Sabine, Teresa, Floortje and Henriëtte were always there to help me with bureaucracy. Petra and Erny were there to promote my newest paper. Roos, Reshma, Wouter, Linda and Sharlene would assist when I had any questions about my employment conditions. Grace was there to make sure all the PV activities were well documented on the intranet, and to listen to my random ideas about composing music and creating worlds. Tatiana, André and Angela made sure that all my product orders are handled with care, while Arnelli, Sebastiaan and Jeroen took care of the payment bureaucracy. Oana helped me with getting into reading scientific publications and making sure my work got out there properly. Finally, Tineke and her crew were there to clean up, keeping my working space a nice and serene place.

And of course my colleagues in research also made my time at AMOLF a lot more pleasant. The master students in my office for example were excellent candidates to discuss perspectives on science, being hyped for the new gaming console that would come out, or keeping track of how much nonsense I had said in our time together. Donny, Sanne, Tom, Daniël, Manuel, Lotte and Michiel, thank you so much for our time together! My colleagues at AMOLF have made a large contribution to my positive experience there. For example with the AMOLF Jam Sessions, where Jenny would show off her better-than-she-says sax play, along with Christian, Weiyi, Benjamin, Cesare, Lukas, Verena, Jose, Mark and Julia to make our music truly epic (and Nasim and Magda being there for support!) Without you all, the music we made would not have been so epic! Moreover, my colleagues were also there for all kinds of other different activities. Playing games with Jeffrey, Niels, Kevin,Isabelle and Ruslan, wart treatments with Roberto, Carolyn and Eliane and so much more with so many more people. Augustin, Luuk, Bas, Anne, Corentin, Hadrien, Scott, Dion, Parisa, Rahul, Balazs, Alexander, Simone, Rene, Robin, Jente, Jesse, Zhou, Hugo, Andrea, Matthias, Nick, Federica, Tom, Toon, Sven, Hongyu, Jian-Yao, Lucie, Imme, Marco, Daphne, Yorick, Mareike, Yvonne, Dario and everyone else, thank you so much for all the great times!

The people I met during conferences also made my PhD experience an exceptionally pleasant one. In particular Arjun, Stelian, Esmee and Maria have made a great impact, showing me the power of a good application, the pleasant side of Romania, the art in science and the beauty of collaberation respectively. Maria, with you my journey of going to conferences to get new collaberators started. Of course this resulted in arguably the publication of my PhD I'm most proud of, but I also just appreciated working together and learning (and celebrating success) with you.

Many more collaborators made my PhD a success. Erik, Gede, Sarah, Sophie, Roland, Esther, Marco, Ling, Ting, Fernanda, Alejo, Martin, Shiju, Anja, Eliane and Anne, thank you for your input and great research while assisting me, I hope my contributions helped you as much as yours helped me. Fernanda, asking you to collaborate on my PhD project was one of the most Hail Mary things I have done during my PhD: Going to a conference where I know no one to ask someone over a dinner to look at the 3 slides I have on my laptop... Who knew that it would result in a great collaboration, a pseudo-mentor when Wim was ill, and in the end a committee member for my PhD defence!

Of course, I highly appreciate my other PhD committee members as well. From the University of Amsterdam, I would like to thank Daniel Bonn, Bas de Bruin and Chris Slootweg for their time and insights given to this thesis. Martin van Hecke, thank you for looking at my triangle approach and shaping it to a vital part of the thesis. Helmut Cölfen, your enthousiasm was truly contagious when we met in Granada early into my PhD, and definitely helped with giving this thesis shape. Finally, I would like to thank Huib Bakker for being my promotor, thank you for finding the time to guide my promotion in the right direction. I would also like to express my thanks to my previous supervisors and people that have coached me sporadically along the way. Paul, Pim, Nehar, Jimmie, Joan, Bert and Alan, thank you for inspiring me and motivating me to continue the road to what now has become my PhD.

Furthermore, my friends outside of AMOLF made sure that I wouldn't bubble too much into one direction. Martin and his Jazz group learned me how to improvise, while Peter and the Amsterdam DnD group showed me the ropes of leading a story. Thank you all for this, I really appreciate learning while having fun :). Furthermore, Gerwin, Bernd and Timo, thank you for being around all this time. Whether it is to discuss my existential crises or being guinea pigs for my newest plans, I'm happy that you are there to support me: You truly are the beginning point of a lot of the things I try, and protect me from making a mess out of it.

Verder switch ik voor mijn familie even naar het Nederlands (maar niet helemaal, speciaal voor Petra ;) ). Pap en mam, bedankt voor alle goede zorgen, ook voordat mijn PhD periode überhaupt begonnen was. Jullie hebben mij perfect de basis gegeven om mijn PhD te voltooien; zowel in de juiste houding om de goede aanpak te vinden, als steun tijdens de moelijkere periodes van mijn opleiding. Dineke, Pieter, Nynke, Willeke, Arian, Janika en Stefan, jullie als familie zijn altijd een positief element in mijn leven. Zij het de connectie met mijn oudste zus, mijn verbazing over hoe slim jullie uit de hoek kunnen komen, of de iets-meer-dan-een-triologie Twilight weekenden, ik ben altijd blij om tijd met jullie door te brengen. Petra, ik ben blij om je als zus te hebben. Je sterke (en goed onderbouwde) mening zet me altijd aan tot denken, terwijl je zorgzame innerlijk een warme charme aan je geeft. Corine, Bart, Lisanne, Danny en Ivan, jullie gezin is hartverwarmend om samen te zien. Hoewel jullie huis nog niet helemaal af is, zijn jullie altijd wel een thuis voor mij (en de rest van de familie). Anne, Jessica en sinds kort Nikita, bedankt voor de vele gastvrije uitnodigingen die Maxime en ik gehad hebben om bij jullie te komen gourmetten. Jullie hebben me altijd enorm geholpen met het delen van jullie ervaringen, die ik vaak als inspiratie kon gebruiken om vergelijkbare situaties in mijn eigen leven aan te gaan. Kees, bedankt dat je het lang uitgehouden hebt bij onze ouders totdat ik ook klaar was om het huis uit te gaan. ;) Ik hoop dat je het nog steeds naar je zin hebt in Engeland, al mis ik de mogelijkheid om je makkelijk te spreken wel!

Maxime, als ik gewoon zou zeggen hoeveel je voor me betekent, zou je dat niet volledig accepteren. Tot op een zekere hoogte is prima, maar daarna moet ik niet zo gek doen. Helaas moet ik toch die hoogte even ingaan, anders zou mijn dankwoord aan jou onvolledig zijn. Ik kan me nog herinneren dat ik eindelijk bedacht had wat ik in een relatie zocht: Een meisje dat zowel lief was, als scherp uit de hoek kan komen. Dat eerste ben je van nature, ik denk dat niemand daar tegenin kan gaan. En iedere keer als ik weer teveel bedenk om te gaan doen en het me teveel wordt, is die kant van je er om me bij te staan, zodat het uiteindelijk allemaal wel weer gaat. Aan de andere kant vind je het ook niet erg om even mijn ideeën aan de kaak te stellen, waardoor ik zeker van ze ben zodra ik ze presenteer. Samen met Anja, Alexander en Robin ben je echt familie voor me geworden, en ik hoop dat nog lang met jullie te ervaren.

# Thank You Everyone!